University of Dundee

University of Dundee

DOCTOR OF PHILOSOPHY

Physical characteristics of laser processed hydrogenated amorphous silicon

Halim, Mohd Mahadi

Award date:
2012

Link to publication

General rights
Copyright and moral rights for the publications made accessible in the public portal are retained by the authors and/or other copyright owners and it is a condition of accessing publications that users recognise and abide by the legal requirements associated with these rights.

- Users may download and print one copy of any publication from the public portal for the purpose of private study or research.
- You may not further distribute the material or use it for any profit-making activity or commercial gain
- You may freely distribute the URL identifying the publication in the public portal

Take down policy
If you believe that this document breaches copyright please contact us providing details, and we will remove access to the work immediately and investigate your claim.

Download date: 04. May. 2023

DOCTOR OF PHILOSOPHY

Physical characteristics of laser processed hydrogenated amorphous silicon

Mohd Mahadi Halim

2012

University of Dundee

Conditions for Use and Duplication
Copyright of this work belongs to the author unless otherwise identified in the body of the thesis. It is permitted to use and duplicate this work only for personal and non-commercial research, study or criticism/review. You must obtain prior written consent from the author for any other use. Any quotation from this thesis must be acknowledged using the normal academic conventions. It is not permitted to supply the whole or part of this thesis to any other person or to post the same on any website or other online location without the prior written consent of the author. Contact the Discovery team (discovery@dundee.ac.uk) with any queries about the use or acknowledgement of this work.

Physical Characteristics of Laser Processed Hydrogenated Amorphous Silicon

Mohd Mahadi Halim

A thesis submitted in partial fulfilment of the requirements of the University of Dundee for the degree of Doctor of Philosophy

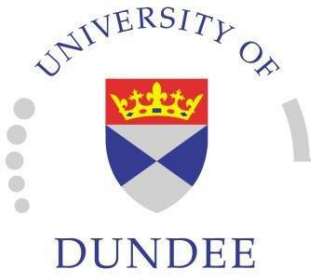

Carnegie Laboratory of Physics

Division of Electronic Engineering and Physics

University of Dundee

Nethergate, Dundee DD1 4HN, UK

April 2012

Declaration

This is a declaration that the candidate is the author of the thesis, that all references cited have been consulted by the candidate, that the work of which the thesis is a record has been done by the candidate and that it has not been previously accepted for a higher degree.

Signed

Mohd Mahadi Halim

Abstract

Hydrogenated amorphous silicon films subjected to KrF excimer laser irradiation with a profiled beam in air leads to the formation of microstructures. The main objective of this research was to perform a comprehensive study in understanding this material in three different aspects: thermal, electrical, and optical properties by experiment, SEM analysis and modelling.

For the thermal interactions, analysis was carried out to investigate factors relating to the formation of the microstructures in a range of applied laser fluences from 93.8 to 443.8 mJ/cm^2. The tallest microstructures were formed with average height from 1 to 3 μm at laser fluence of 312.5 mJ/cm^2. Investigation also include the effect of different applied laser fluence, different scanning schemes, the effect of the presence of 300 nm metal layer, and irradiation environment. Thermal modelling using COMSOL simulation software was used to simulate heat transfer during laser-material interaction and the results suggest a fair agreement with experimental findings. SEM and TEM reveal that the material formed was an oxynitride with embedded particles of crystalline silicon.

In the electrical part, conductivity and field emission were the main tools to help elucidate the internal structure. Arrhenius plots acquired from conductivity measurements demonstrates a decrease in activation energy from 0.8957 eV from original sample to 0.3955 and 0.1727 eV for HE and LE sample respectively. Analysis also showed an agreement with Meyer Neldel rule for both samples. Observation made on the ratio of dark current to photogenerated current revealed the

decrease from 59600 in original sample to 1.77 and 1.40 for HE and LE samples respectively. For the field emission properties, IE plots from samples were analysed using 170 μm fixed gap structure, and lowest emission thresholds were achieved at 3 and 2.4 V/μm for HE and LE samples respectively. The results were fitted to a model of conducting particles in an insulating matrix offering a transport route to the surface.

In the optical part, FTIR measurements were carried and analysis in IR absorbance profile within range of 550 to 2200 cm^{-1} demonstrates SiH_x absorbance peaks at 640 cm^{-1}, between 1980 to 2100 cm^{-1}, and at 2095 cm^{-1}. Hydrogen content was found to be decreased with the increase in applied laser fluence from 12 % in original sample to 4.2 and 1.5 % for HE and LE sample respectively. Measurements using UV-Vis between wavelengths of 200 to 1100 nm shows high absorbance up to 98% for laser process sample from 218.8 to 312.5 mJ/cm^2. TR analysis demonstrated increasing absorbance properties at increasing incident angle. Raman spectroscopy showed an increase in the crystal fraction with laser fluence. The final analysis work in this thesis examines the material as a potential disordered photonic crystal and studies the propagation and localisation of light in ordered and disordered photonic crystal, modelled using COMSOL simulation software. This shows the transition from diffusive to localised propagation. A number of applications are suggested for this structured material. This is the first report of a new large area 'black silicon' material that has a number of interesting applications.

Acknowledgements

This thesis would be impossible to complete without help from all nice person I have ever known in my life, listed as follows. I would like to thank my supervisor, Professor Mervyn Rose for his kind guidance through my entire research study. Many thank to Dr Yongchang Fan for helping me especially for laser irradiation and SEM analysis. And also many thanks to Dr Saydulla Persheyev for introducing and explaining about measurement gears and post measurement discussion. Thanks also to Dr Amin Abdolvand for helping with thermal analysis, and Prof Charlie Main for helping with modelling. Not to mention, thanks to Mr Stuart Anthony for depositing amorphous silicon and preparing all related PECVD process samples. I would like to thank Mr Jin Yao and Mr Qamar Goher from my group and their families, for friendship and cares.

Special thanks go to my family, especially my wife Ms Elly, and our little daughter Bushra for always by my side with unconditionally love and support. Thanks also to my entire friend in Dundee for their assist and memorable experience. And not to forget, many thanks to Government of Malaysia and Universiti Sains Malaysia for sponsoring expenses throughout my higher degree study.

Contents

List of Figures

List of Tables

List of Acronyms

AMRG	Amorphous Material Research Group
a-Si	Amorphous silicon
a-Si:H	Hydrogenated amorphous silicon
BSD	Ballistic electron surface-emitting display
CdSe	Cadmium Selenide
CRN	Continuous random network
DBP	Dual beam photoconductivity
DC	Direct current
EDX	Energy-dispersive X-ray spectroscopy
e.m.	Electromagnetic
ENH	Electrically nanostructured heterogeneous
FED	Field emission display
F-N	Fowler-Nordheim
FTIR	Fourier transform infrared spectroscopy
FWHM	Full width at half maximum
HE	High energy leading edge scanning scheme
HSM	High stretching mode
IR	Infrared spectroscopy
LCD	Liquid crystal display
LE	Low energy leading edge scanning scheme
LSM	Low stretching mode
MVEDs	Microwave vacuum electron devices
NEA	Negative electron affinity

OSA	Optical Spectrum Analyser
PDS	Photothermal Deflection Spectroscopy
PECVD	Plasma-enhanced chemical vapour deposition
PV	Photovoltaics
RF	Radio frequency
SCIBB	Space charge induce band bending
SE	Spectroscopic ellipsometry
SEM	Scanning Electron Microscope
SLG	Super Lateral Growth
SWE	Staebler-Wronski effect
TR	Transmittance-reflectance
TFT	Thin film transistor
THz	Terahertz
UV-Vis	UV and visible spectroscopy
VHF-PECVD	Very high frequency - PECVD

Chapter 1 Introduction

1.1 Background Motivation

Silicon is the second commonest element in the earth's crust after oxygen [1]. Apart from its well known role in today's electronics industry, silicon and its compounds were found to have very useful applications in our daily life. This ranges from glass windows, cement concrete to silicone – synthetic compounds.

In the electronics industries, silicon plays a vital role in the branches of microelectronics, optoelectronics and photovoltaics (PV). Research on the properties of silicon has been carried out extensively throughout history from the day of its discovery until the present day. Crystalline silicon shares the biggest part of the market. This is due to its suitability, its nascent oxide and the maturity of the silicon technology itself.

The three most common silicon allotropes form are single crystal, polycrystalline and amorphous silicon. Each of these allotropes has their own advantages and disadvantages. Single crystal silicon is known for its properties such as fast carrier mobility, strong structure which make it stable mechanically and very good for heat dissipation whilst polycrystalline silicon has the advantages of easy production and low cost. This is amongst the reasons it became the key component in solar cell and can be used as a contact layer or resistor in microelectronics.

Amorphous silicon is the easiest to produce among these three allotropes. It can be produced using plasma-enhanced chemical vapour deposition (PECVD) at substrate temperatures less than 300^{o}C. This feature makes amorphous silicon suitable for deposition on plastic substrates with typical melting point of 150^{o}C, a key to flexible electronics applications such as flexible displays or flexible solar panels, allowing reel to reel processing.

One of the most important factors affecting semiconductor performance is the doping process. The first doping process was reported by J. R. Woodyard in 1950 [2]. Doping in simple terms is the addition of trivalent or pentavalent impurities to the intrinsic Group IV (in the case of Si) semiconductor at a measured level. This process can either transform the semiconductor to become a p-type or n-type semiconductor. P-type refers to the semiconductor with trivalent element substitution where the majority carriers are holes while n-type refers to the semiconductor with pentavalent impurities with electrons as the majority carriers.

The perceived inability to dope amorphous silicon made this material less interesting to the electronics industry. It was not until 1976 when Spear and LeComber working at the University of Dundee reported the first successful attempt to dope hydrogenated amorphous silicon from the gas phase [3]. Amorphous silicon can be doped with diborane or phosphine to make it either p-type or n-type respectively. After this discovery, the thin film transistor (TFT) using amorphous silicon technology was developed and used in liquid crystal display (LCD) technology [4]. Additionally, thin film solar photovoltaic technology made from amorphous silicon also emerged. This technology covers the market where cheap

and easily fabricated PV modules are required. Thin film silicon has been studied because of its low mobility, with laser processing techniques to produce polysilicon with higher carrier mobility.

In 1998, a Harvard group led by Eric Mazur discovered a very simple way to produce 'black silicon' (textured light absorbing Si surfaces), by irradiating Si by femtosecond laser pulses in a chamber containing sulfur hexafluoride gas [5]. Before this discovery by Mazur, black silicon was produced by a reactive ion etching process. This process produced black silicon with needle like structures on the surface. But the black silicon produced by Mazur group's was in the shape of cone-like features on a microscopic scale. Due to this unique shape and distribution, the black silicon absorbed a wider spectrum of incident light than the original silicon [6]. This feature suggests several promising applications in image sensor, thermal imaging, solar cells and terahertz technology. Currently, an American company named SiOnyx is the first in commercialising the black silicon [7].

In 2006 Fan et al. from the Amorphous Material Research Group (AMRG) University of Dundee produce similar results, but over a large area, by irradiating amorphous silicon thin films in air by excimer laser [8]. The results were followed on in the quest of an amorphous silicon based field emission display (FED) backplane by laser annealing for low power and low cost devices where nanoscale features were produced. A feature of this 'new material' is randomly organised 'conical' microstructures and it is interesting to know about the formation and physical properties of this material so that potential applications can be predicted.

1.2 Aim of Thesis

The main aim of this thesis is to characterise the properties of laser processed amorphous silicon, also known as “large area black silicon”, produced by excimer laser processing. KrF excimer laser annealing at 248 nm of a-Si:H films results in various type of micro and nano structures with different surface morphology and internal structure. This thesis aims to give a comprehensive study of the properties of these new nanocomposite materials in terms of their thermal, electrical and optical properties.

1.3 Thesis Outline

Chapter 1

In this first chapter of the thesis, the background to silicon technology is given. The motivation of the whole project then follows. Then a summary of the thesis outline is given.

Chapter 2

In this chapter, a brief introduction to the main concepts in amorphous silicon and the laser crystallisation processing is given. This also includes the properties of amorphous silicon, different techniques for sample preparation and properties of the excimer laser system.

Chapter 3

This chapter will discuss details of the thermal properties of amorphous silicon. This includes the experimental procedures, surface morphology and thermal modelling during laser pulse heating.

Chapter 4

The electrical properties of laser processed amorphous silicon are discussed in this chapter. The results from experiments on conductivity measurement and electron field emission are outlined and discussed.

Chapter 5

In this chapter, the discussion covers the optical properties of the laser processed thin films. Experimental techniques such as UV-Vis, FTIR and TR analysis are included with additional simulation on localisation of light.

Chapter 6

An overall discussion of the optical, thermal and electronic properties is done in this chapter based on the finding from the experiments that have been carried out. Conclusions from this research project will be given and a list for future work is suggested.

Chapter 2 Review of Amorphous Silicon and Laser Processing

2.1 Introduction

In this chapter a review of hydrogenated amorphous silicon and its properties, deposition techniques, and laser crystallisation properties will be discussed. A brief history of amorphous silicon is given before details of the properties of the material in term of its structure, density of states, electronic and optical characteristics. There then follows a discussion of two different methods of sample deposition, namely PECVD and DC sputtering of the metallic backplane. In the final part of this chapter a review of the laser crystallisation techniques will be presented. This part will cover a brief discussion of the historic background, followed by the properties of the laser system itself and the techniques used for producing samples for analysis.

2.2 Background Review

In 1824, the first recorded pure silicon was prepared by Berzelius in the form of the amorphous state [9]. It took 30 years before crystalline silicon was successfully prepared by Deville in 1854 [10]. For about 100 years the research was mainly dedicated to the study of the properties of crystalline silicon. During the period of the 1950's and 1960's, the study of amorphous semiconductors became

very popular. But the attention was given to chalcogenides, materials containing sulfur, selenium and tellurium. The first report on amorphous silicon deposition using silane gas was successfully made by Sterling et al [11]. In 1969, Chittick and the STL group successfully deposited hydrogenated amorphous silicon (a-Si:H) using the 'glow discharge' technique and carried out electrical conductivity measurement of this material [12]. This marked the first step of amorphous silicon as an electronics material. A similar technique of depositing a-Si:H is used to this day, but some of the design characteristics have changed to meet better efficiency and quality of deposited films.

However the promise of this new material was not convincing to the investors at the time and this led to the lab stopping further research. Then W.E Spear from the University of Dundee showed a deep interest in this field and quickly established deposition equipment at Dundee. With his colleague P.G. LeComber, they manage to publish a series of milestone papers showing better performance of this material in terms of its electrical and electro-optic properties [13-14].

Another report from Harvard showed that hydrogen incorporated during deposition plays a crucial role in giving the a-Si:H a better electronic performance [15]. A-Si:H has a disordered structure with a high density of imperfections due to the existence of defects and dangling bonds. The hydrogen is incorporated into the amorphous silicon and passivates these bonds and significantly reduces the defect density. This also means that the density of defects which also represent recombination centre and traps for the carriers is greatly reduced.

The next major successful breakthroughs were the reports on the incorporation of diborane and phosphine into the deposition chamber to make the film p-type or n-type respectively [3]. This was a great achievement where the doping process allowed control of the position of the Fermi level. Prior to this report, it was thought that doping of amorphous silicon was not possible. Doped amorphous silicon was mainly used in solar cell applications in the years between 1975 to 1985 [16].

The first working thin film transistor (TFT) was reported in 1961, and used Cadmium Selenide (CdSe) deposited on glass [18]. But after almost two decades, an amorphous silicon TFT was successfully fabricated and reported in 1979. The report suggested that it had potential to be applied in a liquid crystal display (LCD) driving an active matrix of pixels [4]. The transistor used silicon nitride (SiN) as the gate insulator layer, which was deposited in the plasma chamber by mixing the SiH_4 and ammonia (NH_3). With these unique features, it was realised and agreed by others that amorphous silicon was the most suitable candidate for TFT technology [17].

2.3 Amorphous Silicon Properties

2.3.1 Structure

Silicon has three different allotropes, known as crystalline silicon (c-Si), polycrystalline silicon (poly-Si) and amorphous silicon (a-Si). The main difference between these allotropes was in terms of atomic structure. In crystalline silicon, the atoms are arranged tetrahedrally in a periodic structure with long range order. However, amorphous silicon lacks this attribute and long range order is not present due to displacement of silicon atoms from their ideal single crystal position. The nearest neighbours in the short range are slightly changed, leading to variation in bonding lengths and angles among the silicon atoms. The atoms in amorphous silicon are disordered and form a continuous random network (CRN). This term was first used to describe the atomic structure of glass [18]. The interaction between neighbouring atoms in a short range is stressed rather than the long range order.

Other than imperfection of crystalline structure, another defect distribution in amorphous silicon is through the existence of dangling bonds. This is a defect of isolated coordination and it occurs when the network structure is incapable of satisfying all these bonds. The defect is formed during the deposition process and exists as broken or weak bonds among silicon. This, together with hydrogen interaction results in metastability on light exposure (described in detail later). Figure 2.1(a) illustrates a two dimensional crystalline silicon and amorphous silicon network structure with the presence of dangling bond defects.

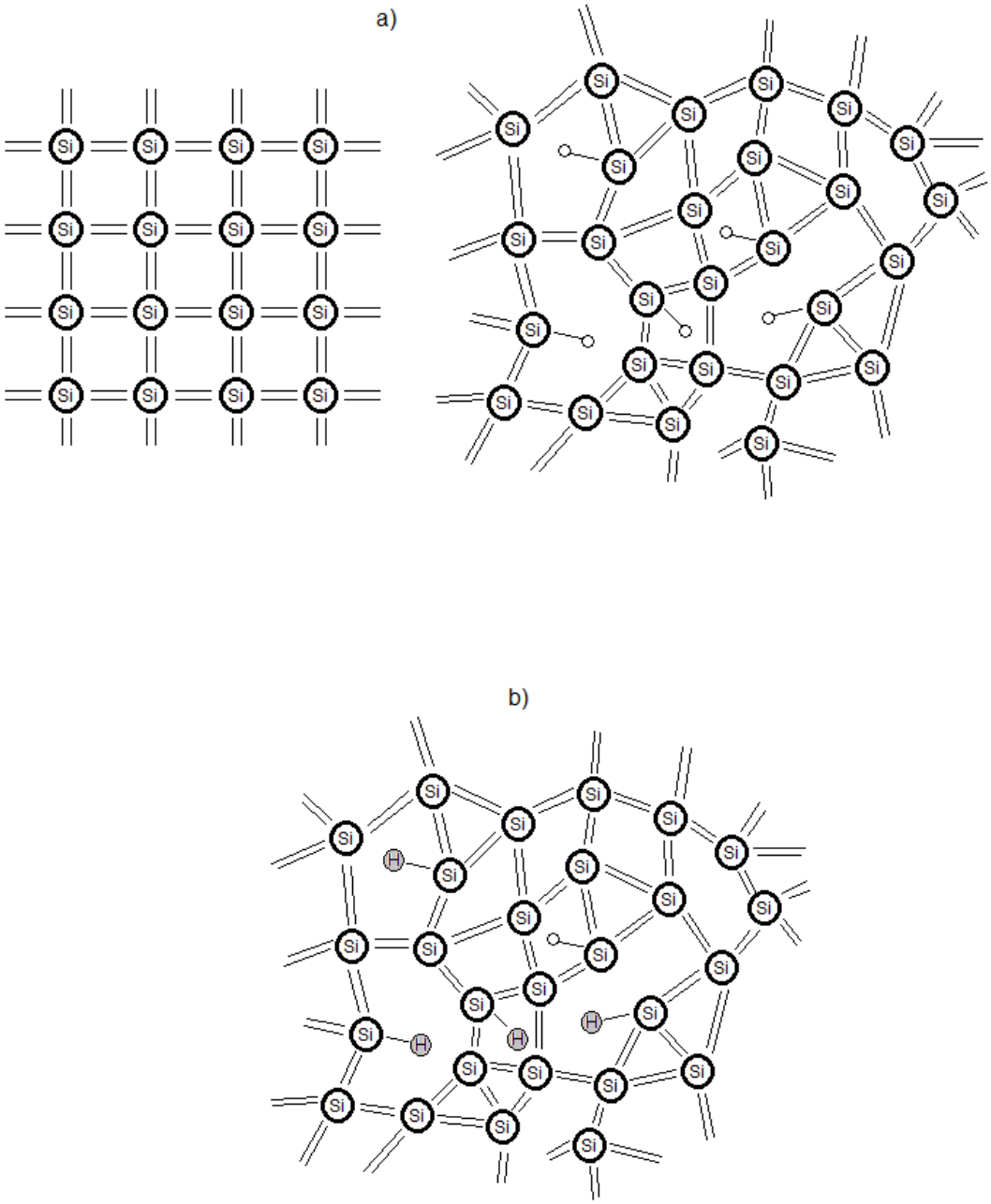

Figure 2.1: (a) Atomic network structure in single crystalline silicon (top left) and amorphous silicon (top right). (b) Hydrogenated amorphous silicon networks structure (bottom).

The hydrogen is used to passivate these dangling bonds, in order to minimise this defect state as shown in figure 2.1(b). The hydrogen is incorporated into the network mostly in the form of Si-H bonds and results in much improved electronic properties. The hydrogen content is typically about 10 to 20 %. Although the number is quite large, the dangling bonds are still present to a concentration of around 10^{15} cm^{-3} [16] which is normally found in a good a-Si:H film.

2.3.2 Density of States

The energy distribution of electronic states is important in order to describe the electronic properties of amorphous silicon. Crystalline silicon has a definite energy gap separating a conduction band from the valence band. However, in amorphous silicon the disorder in the network causes the energy distribution of electronic states to be broadened into the energy gap between the conduction band and valence band.

The standard density of states as shown in Figure 2.2 is used to describe the electronic state structure of amorphous silicon [19]. There are three important parts in the density of states model. First is the 'conduction band and valence band' extended states as in crystalline silicon. Then the band tail region which is close to the conduction band and valence band. The third is the defect state in the middle of the forbidden gap.

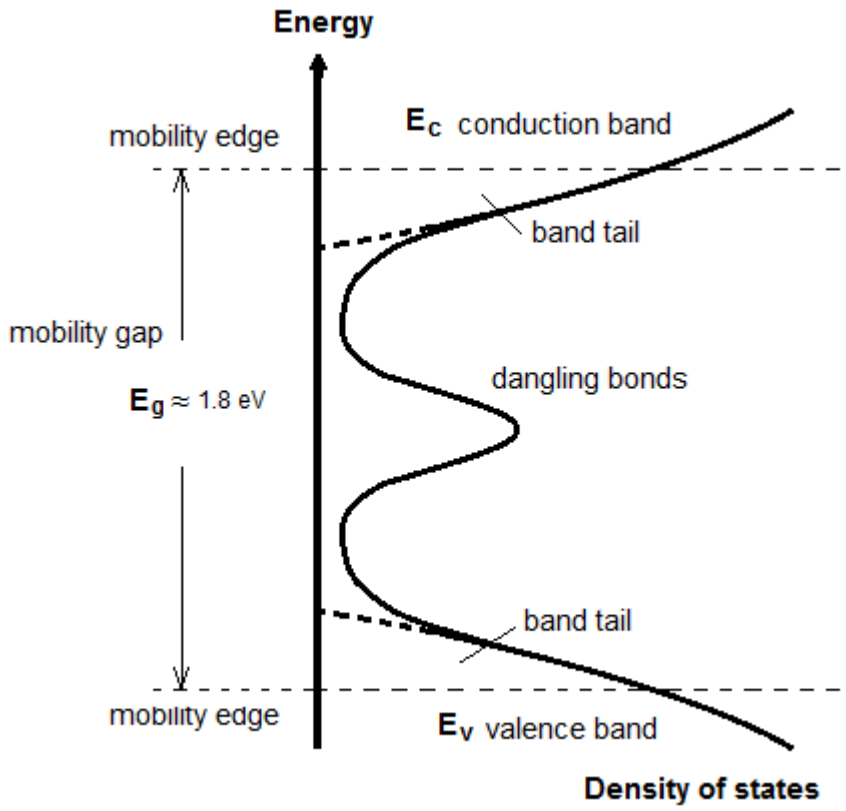

Figure 2.2: The standard distribution of density of states in amorphous silicon [16].

Instead of an abrupt band edge as in crystalline silicon, a broadened tail of states is featured and extends into the forbidden gap. These states exist because of the variation of bond length and angle in the amorphous silicon network. Among the two bands, the valence band tail is actually more influenced by the deformation of the amorphous silicon network compared to the conduction band tail. The consequence of this leads to the difference in Urbach energy, E_U of the conduction band and valence band. The Urbach energy is determined from the exponential energy dependence of the optical absorption [20]. For a good intrinsic material, the

typical values of Urbach energy for conduction band tail is about 25 – 35 meV and for the valence band tail is around 45 – 55 meV.

The electronic conduction occurs at the band edge and this part is important in the study of the electronic properties of amorphous silicon. The existence of electronics states within the forbidden gap is due to the deviation from the ideal network, and these are the coordination defects and dangling bond defects. The mobility edge is the energy dividing the localised states and the extended states and the gap between the conduction band and the valence band is called the 'mobility gap'. The bandgap of crystalline silicon is 1.1 eV and the conduction band separated from the valence band by a definite forbidden gap. In amorphous silicon, the mobility gap was used to explain the range between conduction band and valence band. For amorphous silicon the typical value is around 1.8 eV, depending on the configuration of hydrogen [21] and this energy range is similar to the optical gap [22].

2.3.3 Electrical Properties

The structural disorder affects the electronic properties of amorphous silicon. From the free electron theory, the presence of a band gap is as a result of the periodicity of the crystalline lattice. Similar to the case in crystalline silicon, in amorphous silicon the bands are most strongly affected by the influence of local interaction due to the short range order. The Bloch solutions for the Schrödinger equation of the electronic states are used to describe the energy-momentum (E-$\boldsymbol{k}$)

dispersion relations of the conduction band and valence band. In crystalline silicon, the lattice potential $V(\boldsymbol{r})$, is said to be extended or delocalised because the wavefunctions have a definite momentum, $\boldsymbol{k}$. The situation for amorphous silicon in continuous random networks is different. There is no periodicity in the potential $V(\boldsymbol{r})$ and this is caused by strong scattering over a range of one or two atomic spacings and this leads to a large uncertainty in the momentum of electron, $\boldsymbol{k}$. From the Heisenberg uncertainty principle,

$$\Delta \boldsymbol{k} \Delta x \approx \hbar \tag{2.1}$$

$$\Delta \boldsymbol{k} \approx \frac{\hbar}{\Delta x} \approx \frac{\hbar}{a_0} \approx \boldsymbol{k} \tag{2.2}$$

where, Δx = scattering length

a_0 = interatomic spacing

with the uncertainty in $\boldsymbol{k}$ approximately the same as magnitude $\boldsymbol{k}$. Therefore, momentum is not a reliable quantum number and is not conserved in the electronic transition [22].

The direct consequences from this are the energy bands are not described by an energy-momentum dispersion but rather explained by the distribution of the density of states $N(E)$. Another consequence of the disorder potential is the localised wavefunction being confined to a small volume of material and not extended. The Anderson model is illustrated in figure 2.3 [23]. The crystalline phase is described by a regular array of similar atomic potential wells. Energy width B is the broadened

state energy, formed by the local interaction among atoms. In the disorder structure as shown in figure 2.3(b), the average random potential is added as V_0. Anderson proved that when V_0 / B surpasses a critical value, all states are localised and no electrical conduction takes place at absolute zero. If the Anderson criterion is not met, the localised states still exist at the extreme edges of the band [24].

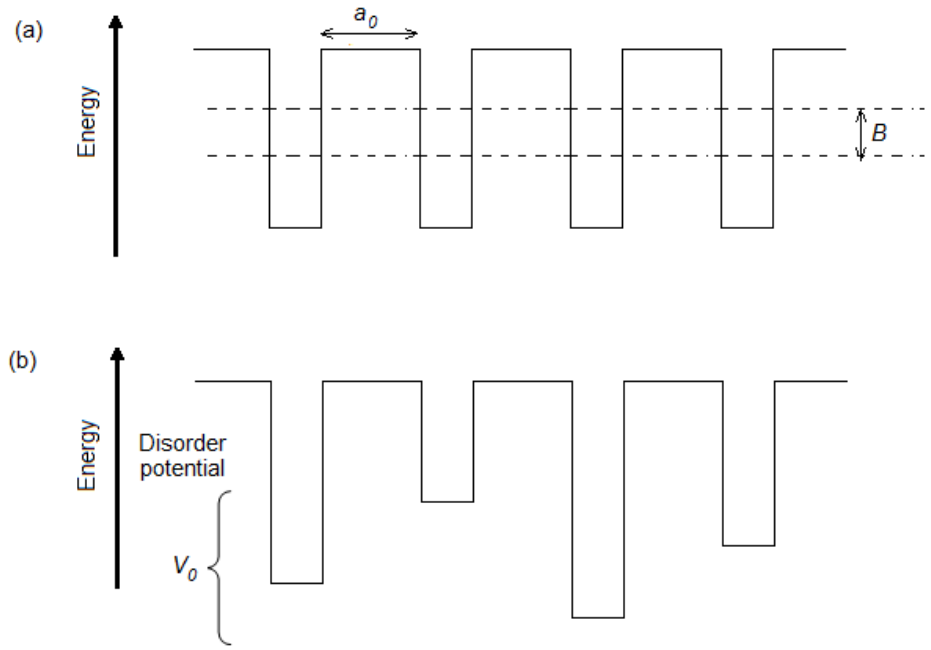

Figure 2.3: Anderson model of the potential wells for (a) crystalline and (b) amorphous network with V_0, the disorder potential [22].

In the real case, the energy bands of amorphous silicon are too broad compared to the disorder potential for complete localisation, but there are broadened band edges & localised states. This case is referred to as tail states or band tails. As in crystalline silicon, only electrons with energy higher than the conduction band are free to move and contribute to the conduction [23-24]. The free electron and hole

have a scattering length of about an interatomic spacing a_0. Consequently, the mobility of free carriers in amorphous silicon is only about 10 to 20 cm^2/Vs. Due to the thermal factors and the fact that carriers are also affected by trapping and release, the actual carrier mobility is less than the given range. This value is much lower compared to the mobility of carriers in crystalline silicon, which are around 1000 cm^2/Vs.

The transport in amorphous silicon is more complicated than in the crystalline silicon. At high such as room temperature (300 K), the electronic transport above the band edge is dominant, whereas at lower temperature (80 K), the electronic transport is more influenced by the multiple trapping mechanisms [25]. This multiple trapping mechanism is described as the electronic transition between delocalised states above conduction band and to the localised states below it. Other than that, a hopping mechanism is significant at low temperature. Hopping is a term used to describe electronic transitions between localised states within the mobility gap [26]. The defect states that lie within the mobility gap act as trapping and recombination centres, affecting photoconductivity. Therefore it is important to reduce the defect states in order to enhance the electronic and optical properties of amorphous silicon.

2.3.4 Optical Properties

Silicon is known to have an indirect bandgap in its crystalline state, but not in the amorphous state. The distinction between direct and indirect type of semiconductor is not clear because the optical transition which is not allowed due to the conservation of momentum could occur in amorphous silicon. Photoconductivity is said to occur when carriers absorb the energy of the incident photon and undergo a transition from the valence band to conduction band. When amorphous silicon is exposed to light, electrons and holes are excited to the band edge, then drift towards the positive and negative terminal respectively. In crystalline semiconductors, transitions of electrons from the valence band to the conduction band dominate the photoconductivity. Crystalline silicon is not allowed to make a direct transition, otherwise it violates the conservation of momentum $\boldsymbol{k}$. This is because the corresponding state for electrons to make transitions from valence band to conduction band lies at different values of $\boldsymbol{k}$. A photon, which is the quantum of light, has only small momentum. Therefore phonon involvement is critical to give an additional momentum change. Phonon is the photon counterpart and described as the quantised modes of vibration. This is the reason that such a transition is called phonon assisted absorption and therefore, crystalline silicon is classified as an indirect semiconductor.

2.4 Deposition Techniques

The deposition process is an important part in producing good quality silicon because the structural and hence other properties of amorphous silicon are defined during this process. A good amorphous silicon structure, with low defect density and better stability against degradation, results from good deposition processes, not to mention better electrical and optical performance in terms of reasonably high carrier mobility and optical absorption. Therefore, it is important to know all the important aspects of the growth mechanism in order to obtain the best possible electrical and optical properties. By optimising the related parameters, lower cost production can be achieved.

Plasma decomposition of silane gas is the typical method used to deposit amorphous silicon on substrates. Without the presence of plasma, silane decomposes at temperatures above 450^{o}C. Generally this high temperature method has been used to create an epitaxial layer of silicon or polycrystalline silicon.

A similar method has been used to grow amorphous silicon. But the quality of such films was not good since most of the hydrogen escaped due to the very high temperature environment [22]. This results in a very high defect density and therefore produces amorphous silicon with poor electronic and optical properties. A better quality film could be produced by decomposition of silane in plasma at lower temperatures. With this condition, hydrogen in the surrounding plasma passivates and satisfies the dangling bonds, consequently reducing the concentration [27].

The type of plasma system used by Chittick et al. to deposit the amorphous silicon was a radio frequency inductive system. The plasma inside the reactor chamber was created by an external induction coil [28]. This was known as a pioneering method of producing hydrogenated amorphous silicon. Although different methods had been introduced and evolved, the basic operations were fairly similar.

In the following sections, the details of PECVD process will be discussed. Additionally, a method for depositing metal backplanes, namely DC magnetron sputtering will also be discussed. Metal backplanes were used as a part of experimental technique associate within this project, and served to catalyse reactions with silicon under laser irradiation.

2.4.1 Plasma Enhanced Chemical Vapour Deposition

PECVD is recognised as a standard method to produce industry quality amorphous silicon. It is also known as the glow discharge method because of the presence of plasma inside the chamber during the deposition process. The principle behind PECVD is based on a radio frequency (RF) capacitive coupled system (compared to the inductive system used by Chittick).

A capacitively coupled parallel plate reactor is placed inside the deposition chamber where silane is decomposed into plasma species and confined between the two parallel electrodes [29]. Figure 2.4 shows a standard PECVD system. The reactor chamber receives several source gases through a set of gas inlets. These gases

(e.g. silane, hydrogen, nitrogen, etc) are regulated by flow controllers. Inside the reactor chamber, the substrate is placed on a substrate holder which sits on a heating system. The RF generator supplies power to a cathode for electrical discharge.

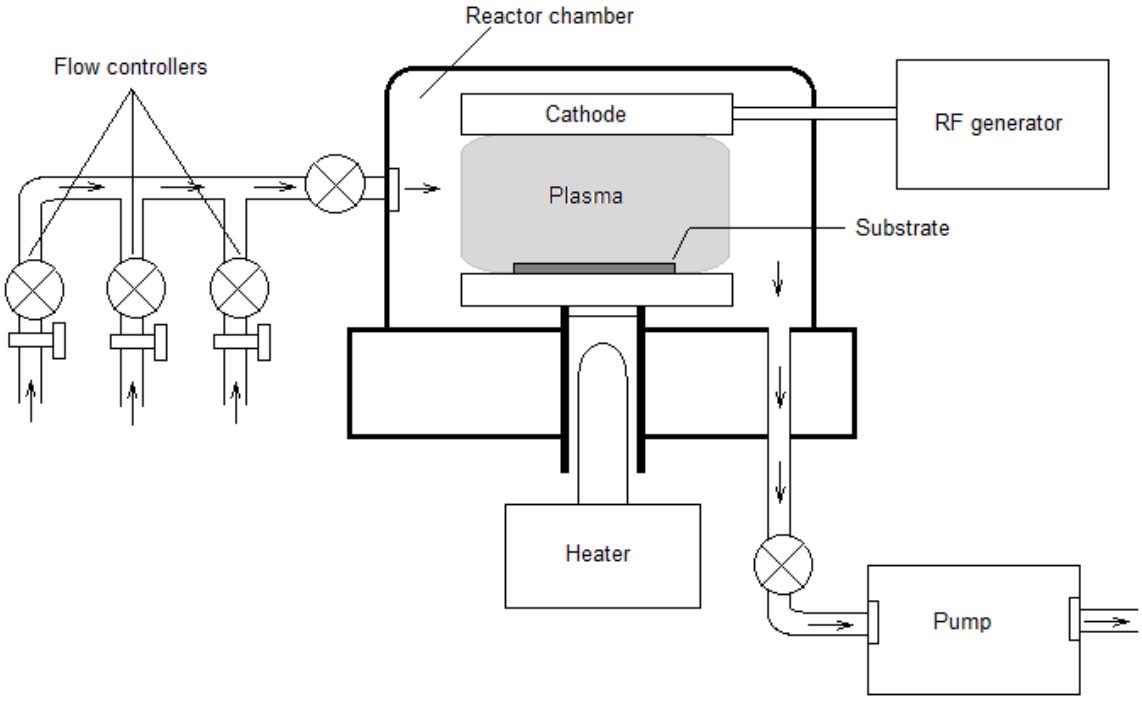

Figure 2.4: Cross sectional view of a typical PECVD system.

Although the system looks quite simple, several parameters need to be regulated to facilitate the production of good quality amorphous silicon. The average distance (mean free path) of the gas molecules for collisions is determined by the gas pressure, and a pumping system is used to pump out the residual gases. This will affect whether the reaction takes place on the substrate or in the gas. The average amount of time (residence time) of the gas inside the chamber is determined by the

gas flow rate. The RF power source controls the gas dissociation rate, hence determines the rate of film growth. The substrate temperature, T_s controls the chemical reaction on the substrate.

Normally deposition processes takes place at gas pressure between 0.1 to 1 Torr. This is the optimum pressure to sustain the plasma. The industry standard RF 13.56 MHz is used for the plasma excitation frequency. While other parameters are also recognised to influence the amorphous silicon properties, the most important parameter is substrate temperature T_s. Usually the best quality amorphous silicon is produced at T_s between 200^{o}C and 300^{o}C. The optimum gas flow rate also influences growth but it is less defined as a result of reactor design variations.

The growth mechanism inside the chamber can be explained as follows. The applied electric field accelerates the electrons and sustains the electrical discharge. These electrons collide with the source gas molecules, causing the ionisation process hence, creating more free electrons. However, the acceleration of ions in the plasma is insignificant due to their large mass compared to the electrons. The silane gas is broken into several neutrals radicals or ions. For example, the dissociation processes are:

$$SiH_4 \rightarrow SiH_2 + H_2 \quad \text{at 2.2 eV}$$
$$2SiH_4 \rightarrow 2SiH_3 + H_2 \quad \text{at 4.0 eV}$$
$$SiH_4 \rightarrow Si + 2H_2 \quad \text{at 4.2 eV}$$

These radicals, ions, free electrons and photons form a weak plasma between the electrodes. The SiH_3 radicals are less reactive and their creation is crucial since

they persist to exist longest despite collision with other molecules. As a result, they have the highest probability to survive and finally deposit on the hot substrate.

The subsequent process is the molecular fragment adsorption onto the substrate. This is followed by hydrogen liberation from the surface. The process is essential since the SiH_3 radicals could not make any bonding if Si-H bonds are terminated. Consequently, a good quality amorphous silicon film contains hydrogen to about 10%. The presence of hydrogen is very important since it is capable of removing subsurface defects, or dangling bonds. At the final stage of the deposition process, the hydrogen passivates and satisfies these dangling bonds [30].

Doping of amorphous silicon can be done by adding into the chamber additional gases such as diborane (B_2H_6) and phosphine (PH_3) to produce p-type or n-type amorphous silicon respectively. This feature enables much wider application of amorphous silicon especially in electronics.

Some modification has been made to existing systems by increasing the frequency of plasma excitation up to 300MHz. This is known as very high frequency-PECVD (VHF-PECVD). The result is an improved deposition rate by approximately one order of magnitude compared to standard PECVD.

2.4.2 DC Sputtering of Metal Backplanes

Magnetron sputtering is widely known as a standard preference method for coatings in industry and the laboratory [31]. Although there are a number of different types of sputtering system, specifically DC magnetron sputtering is used for this project. The glass substrate is coated with a thin film of metal as a back contact. This configuration is used especially for field emission measurements, but the metal also serves as a catalytic system for the transformation of the material under laser annealing.

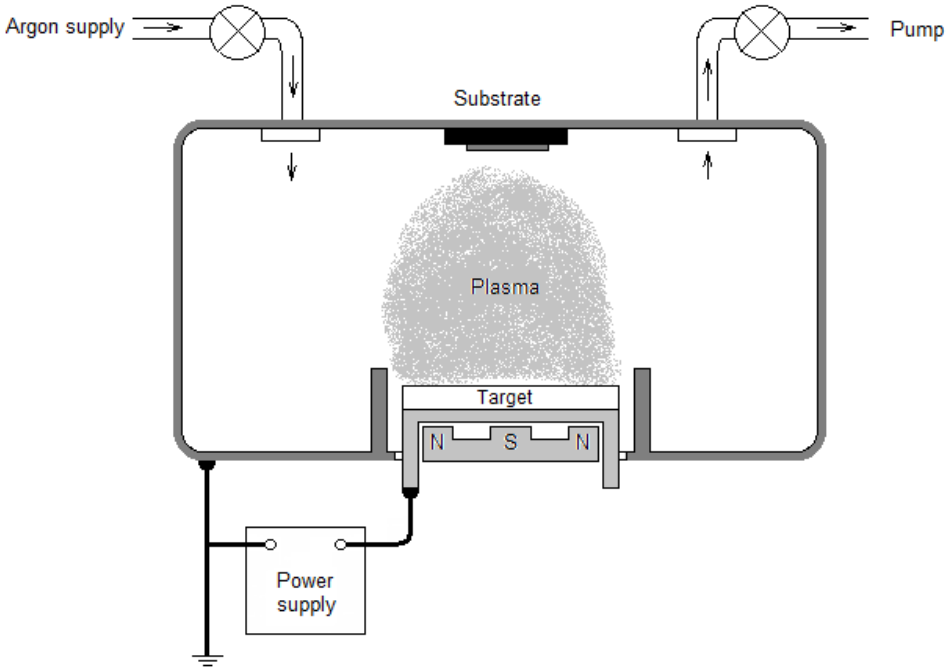

Figure 2.5: Cross sectional view of a typical DC magnetron sputtering system.

Figure 2.5 shows a typical DC sputtering system. A gas supply inlet is connected to the sputtering chamber and a pump is used to control the pressure inside the chamber. The target is the source of the coating material and it is located at the bottom of the chamber. A high voltage power supply is connected to the target with a permanent magnet located below. The role of the permanent magnet is to confine the plasma to a particular area on the target.

The operation of the DC sputtering system is as follows. Argon is supplied into the sputtering chamber at a pressure of approximately 1 Pa. Then a high voltage DC power supply excites a plasma between the two electrodes. The cathode, which also holds the sputter target, is set to a voltage drop at 1kV and then accelerates the positively charged argon ions. This high kinetic energy argon ion then bombards the target and knocks out individual atoms at the target surface. The ejected atom moves towards substrate as well as in the other direction. The sputtered materials finally reside on the substrate randomly. The subsequently sputtered materials combine with the existing material and form small islands which then become the growth nucleation site. All these islands finally coalesce and form a uniformly coated surface.

Properties of the coated film are controlled by rate of deposition process as determined by the applied voltage, and the mean free path of the sputtered material is controlled by the pressure inside the chamber. This also affects the atomic structure and texture of the final coating. Other than that, the substrate temperature can also affect the atomic structure.

2.5 Laser Crystallisation Techniques

2.5.1 Review

The theoretical basis for laser operation, which is radiation from stimulated emission, was introduced by Einstein in 1917 [32]. The stimulated emission was achieved first in the microwave region by C. H. Townes [33], in a device known as a maser, (acronym from microwave amplification by stimulated emission of radiation). Although the effort had been made to produce stimulated emission in the optical region, it was not until 1960 that the first working laser was successfully built and demonstrated by Theodore Maiman from Hughes Research Laboratory [34]. It was a short pulse ruby laser, excited by a flash lamp. In December the same year the first continuous laser was constructed in the Bell Telephone Laboratory using a helium and neon gas mixture and pumped by electrical discharge [35]. Since then, the developments in laser science and technology have been advanced much further and the laser is no longer dubbed as "a solution looking for a problem".

Predictions of temperature profiles in materials upon laser irradiation was made by Anisimov [36] and then developed much further in the following years [37-38]. Detail analysis of thermal conditions resulting from laser heating and melting has been made by Anthony and Cline [39]. They reported on the effect of the melting flow towards the temperature gradient of material. Early research on laser irradiation upon silicon was pioneered by Usui's group from the Sony Research Centre in the mid of 1980's. They reported on the heat transfer between thin film and substrate, the effect on surface morphology, the ability of poly silicon to amorphise and recrystallise, and most importantly, they managed to show that it is possible to

fabricate low resistivity poly silicon at low processing temperature [40-44]. Most of the laser processing work was carried out using excimer laser due to the advantages of this type of laser, particularly for silicon.

2.5.2 Excimer Laser

A phenomenon where a mixture of noble gases emit a luminescent spectra while making a transition from excited state to ground state and their possibility to become as another type of laser was discovered and reported by N. G. Basov et al. in 1970 [45]. However, the first lasing effect using mixtures of noble gas halides was reported 5 years later in 1975 by several research groups from USA, at about the same time [46]. And in 1977, the first commercial excimer laser was available in the market, manufactured by Lambda Physik. Now, the excimer laser is widely known as a powerful tool with applications in areas such as microelectronics, micromachining and eye surgery [46].

The term excimer comes from the words 'excited dimer'. The excimer laser consist of a noble gas mixture or noble gas halide mixture. When this mixture is pumped or excited by electrical discharge, a pseudo-molecule is formed temporarily among the noble gas themselves (dimers) or the noble gas with halides (complexes). Population inversion is achieved when numbers of molecules in their excited states are bigger than in the ground states. Stimulated emissions take place where the excited molecules dissociate back to their ground state. This transition releases the excess energy in the form of pulse electromagnetic waves in the UV region.

The excimer laser has several advantages which make them very suitable for silicon processes. Although a big and quite complicated system requirement for an excimer laser operation need to be installed, the UV laser produces a uniform and large beam size typically around 8 × 20 mm [47], compared to other type of laser such as the smaller size yet small output power of a semiconductor laser. This particular feature is required especially for large area processing technology where a large and uniform beam is essential. Moreover, the wavelength of the UV light KrF laser as an example is 248 nm and this wavelength has absorption depth of 1×10^{-8} m^{-1} in amorphous silicon. Hence, the photon energy is effectively transferred to the silicon film. The small absorption depth hence affected the surface of the film and if the film thickness is ~1 μm, the underlying substrate is virtually left intact. This allows the irradiation process to be carried out on low temperature substrates such as glass and also on flexible substrates such as plastic. Sometimes, the surface of the substrate can be coated with a thin layer of silicon dioxide which acts as a heat buffer. Silicon dioxide has a good insulating character and the resulting heat from laser-silicon interaction is dissipated hence protecting the substrate more effectively.

2.5.3 Properties of Laser

The specific UV wavelength emitted from the excimer laser is determined by the active gain medium which is the gas mixture used. Table 2.1 shows examples of different type of excimer lasers and their output wavelengths. The excimer laser used throughout the whole projects was a KrF excimer laser and produced a wavelength at 248 nm. As the name suggests, the main content of the active medium is krypton gas and fluorine gas. Additionally, helium gas is also installed as a buffer gas while nitrogen gas is used and its role is to purge the emitted laser irradiation [48].

Excimer	Wavelength
F_2 (fluorine)	157 nm
ArF (argon fluoride)	193 nm
KrF (krypton fluoride)	248 nm
XeBr (xenon bromide)	282 nm
XeCl (xenon chloride)	308 nm
XeF (xenon fluoride)	351 nm

Table 2.1: An examples of gain medium used in a different type of excimer lasers and their emitted UV wavelengths, ranging from 157nm to 351nm [49].

The specific model of the excimer laser used is LPX Pro 210 (F), manufactured by Coherent, Inc. The maximum energy produced by this model is 400 mJ and its maximum repetition rate is up to 100 Hz, while the output pulse duration is 20 ns on the full width at half maximum (FWHM). Efficiency conversion from electrical power input to laser power output is typically 2% [50]. As a result a huge amount of heat is generated during the operation, and a water cooling system is used to dissipate the heat away from the main system.

Chapter 3 Thermal Properties

3.1 Introduction

This chapter will cover the discussion on the thermal properties of laser processed amorphous silicon. A review of the crystallisation process and surface modification will be given first. Then details of the experimental techniques and thermal modelling will follow. The subsequent section will cover results and discussions on the formation of microstructures and their variation on changing parameter such as applied laser fluence, scanning method, substrate, metal catalyst layer, ambient conditions, and from single pulse to multiple pulses. The effect on the surface morphology of the amorphous silicon film is the main subject of comparison with consideration given to the internal structure. Thermal modelling will provide the theoretical explanation behind the laser material interaction.

3.1.1 Crystallisation Process

The crystallisation process from pulse laser processes of amorphous silicon is characterised in two major regimes. These regimes are based on the size of grain and duration of melting as a function of the applied laser fluence [16,51]. Between these two regimes, there exists a narrow transition region that can yield very large grain polycrystalline films. This process is called the Super Lateral Growth (SLG) phenomenon [16,51,52]. Figure 3.1 illustrate the location of the regimes and SLG in

the plot of grain size against laser density while, figures 3.2 (a) to (c) depicts the effect on amorphous silicon film at different applied laser fluences.

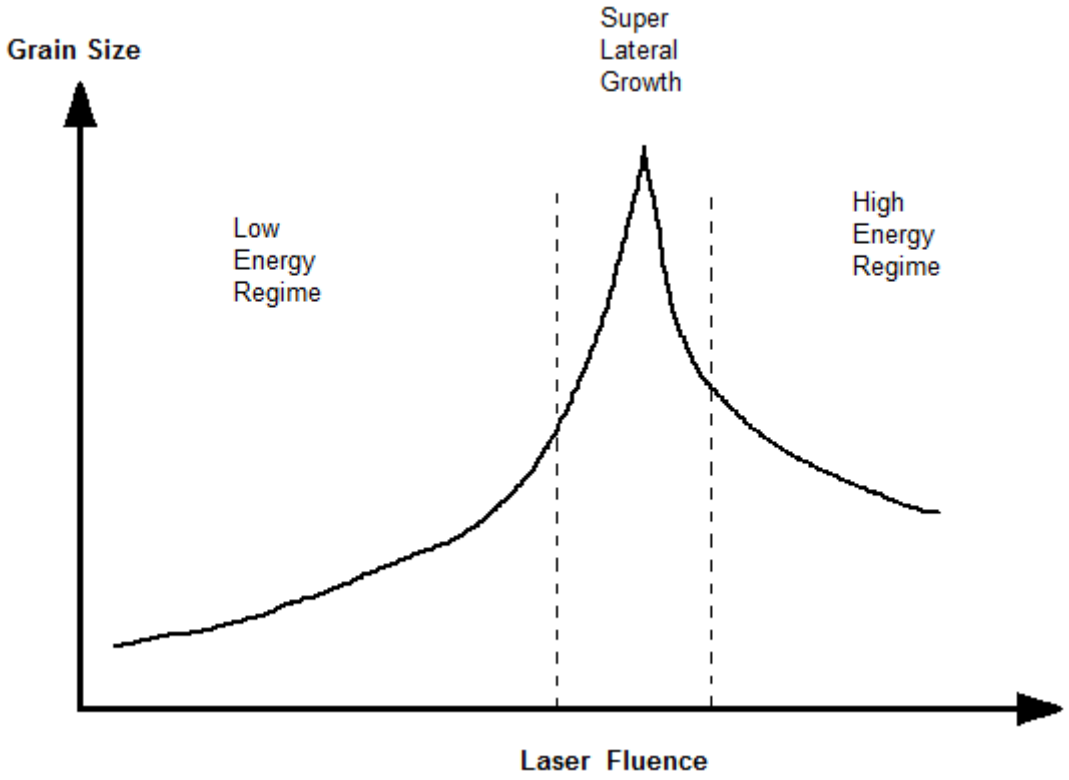

Figure 3.1: Variation of grain size to the applied laser fluence for polycrystalline silicon from laser processed amorphous silicon.

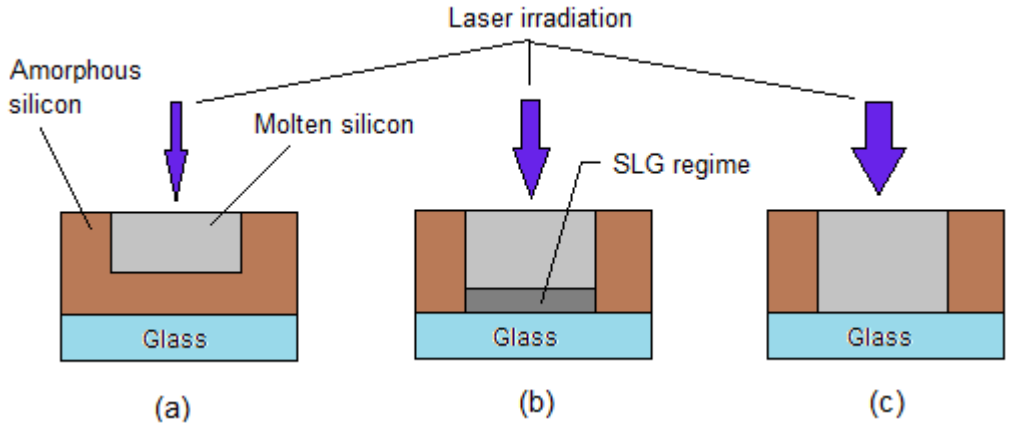

Figure 3.2: Effect on amorphous silicon film during laser crystallisation for, (a) low, (b) medium - SLG and (c) high applied laser fluence.

The low energy regime is classified as when the applied laser fluence is sufficient to induce melting on the surface of amorphous silicon film, but not high enough to melt the entire film thickness. A gradual increase in grain size is achieved with an increase in applied laser fluence. This relation continues until the mean of the grain size is approximately equal to the thickness of the film [53-54]. For a sample at 100 nm on a thick glass or quartz substrate, an applied laser fluence of 100 mJ/cm^2 is categorised in the low density regime [16].

The increase in grain size is understood to occur due to the seeded growth process from the melted liquid phase silicon. The surface of the film has larger grains, while near to the film/glass interface it has smaller grains. This fine grain is the result of rapid melting-cooling propagation of molten silicon across the film where it is also known as explosive crystallisation [55-57]. As the applied laser fluence is increased, much more of the film melts and contributes to the crystallisation process and the number of grain nucleation sites is reduced [16].

SLG occurs in a narrow range of applied laser fluence, at the transition between two major regimes, and coincides with the near complete melting of the film. Within this range, a sharp peak in average grain size can be observed. Individual polycrystallite grains originate from the seeds during explosive crystallisation and are formed during super cooling of the molten film. The length of the grain is determined from the quenching rate, which is related to the thermal conductivity of the substrate.

When further increase in applied laser fluence does not give a clear effect on the structure, a high energy density regime is said to occur [51]. The effect in this

case is usually not very desirable since the process of complete melting can also cause the process of impurities diffusion such from substrate into the film.

3.1.2 Surface Roughness

The mechanism of crystallisation from the laser process is well understood. However, the increase in surface roughness is still not well explained. The irradiated film shows rough and hillock features on the surface. Some of the reasons suggested are:

i) Ambient condition during laser processed

ii) Variation of latent heat and thermal conductivity for polysilicon and amorphous silicon

iii) Resolidification of capillary wave in the molten film

iv) Pulse frequency

v) Amount of hydrogen in the film

From the previous report, it shows that the ambient surrounding can affect the resulting surface roughness, where the irradiation in air yields to higher surface roughness than in the inert condition [58-59]. The active role has been attributed to oxygen. As shown before, the increase in oxygen percentage in the ambient leads to a steady increase in the surface roughness [58]. However the exact role of oxygen during the process is still not well understood.

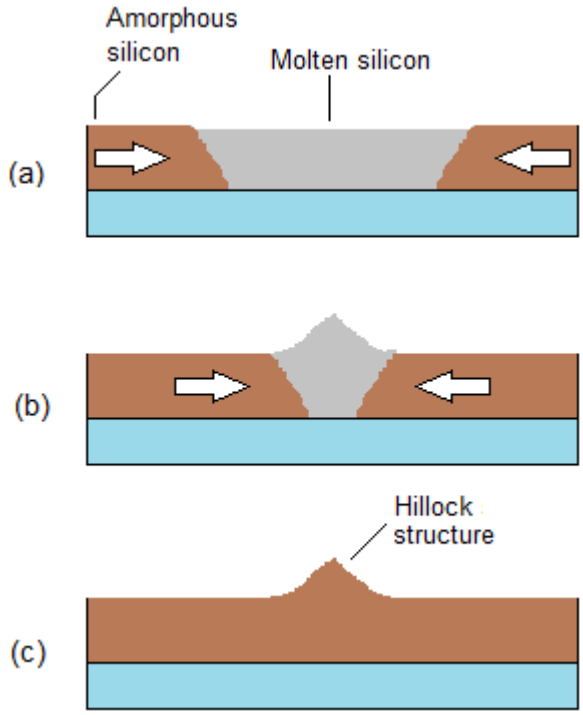

Figure 3.3: Schematic representation propagation of freezing capillary waves at grain boundary shows process of (a) volume expansion, (b) forcing into hillock structure, and (c) solidification as grain boundary structure.

Surface roughening was also shown to result from the freezing of capillary waves which are excited in the molten film during the laser process [59-60]. The volume increase from the solidified silicon drives the remaining molten film towards the grain boundaries. The molten film is forced into a hillock like structure at the emerging grain boundary. Then the complete solidification occurs resulting in the grain boundary structure. This effect is illustrated in figure 3.3. The effect occurs especially when the grain solidification fronts spread at significant lateral distances during the SLG phenomenon.

The effect of the number of pulses on the surface roughness during laser process has been reported earlier for pulsed Gaussian beams [58]. For the same applied laser fluence, it was shown that when low scan speed is used to irradiate the hydrogenated and dehydrogenated film sample, considerable surface roughening is observed. However, with much higher scanning speed, only hydrogenated sample shows significant increase in surface roughness.

3.2 Experiment Techniques

3.2.1 Sample Preparation

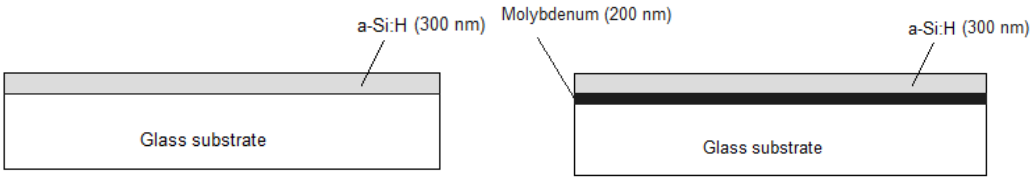

Figure 3.4: Samples of amorphous silicon film on glass substrate (left) and on metal coated glass substrate (right).

For this work, two different sets of samples with the configuration shown in figure 3.4 were prepared to study the thermal effect and surface morphology upon laser irradiation. The deposition process for the amorphous silicon was carried out by PECVD. The first sample was prepared with amorphous silicon on a glass substrate and the second was amorphous silicon on a molybdenum coated glass substrate. The thickness of the amorphous silicon films was 300 nm for each sample. For the

second set, 200 nm of molybdenum was deposited first, by DC magnetron sputtering, before the deposition of the amorphous silicon film. During the process of amorphous silicon deposition, the substrates were heated up to 220°C, the discharge RF power was 10 W and the flow rate of the precursor gas SiH_4 introduced into the chamber was 75 sccm. The time taken for the growth process was 20 minutes. The pressure inside the chamber was maintained at 100 mTorr.

3.2.2 Laser System Arrangement

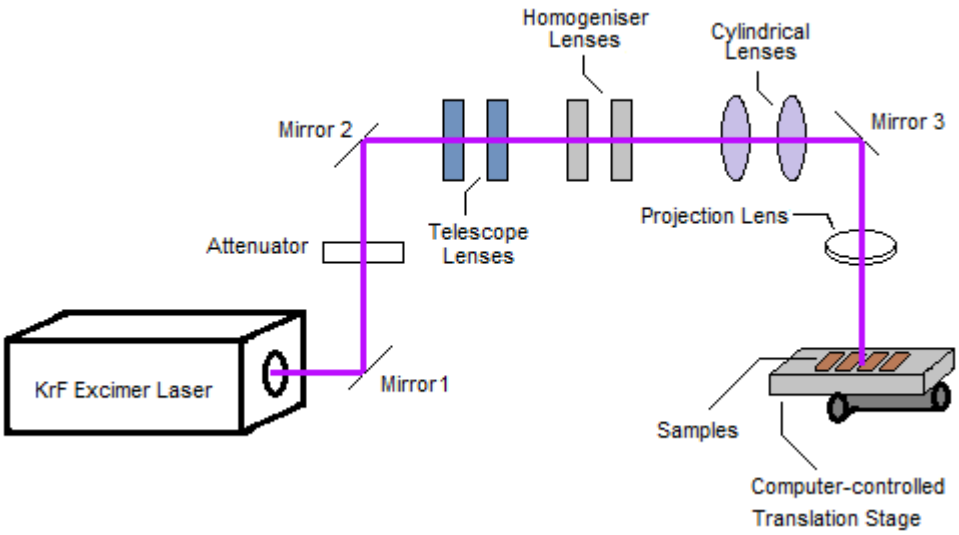

Figure 3.5: Schematic diagram of KrF excimer laser optical system setup.

An asymmetrical slope beam profile was used to irradiate the amorphous silicon film samples. This unique beam profile is one of the most important factors to produce and control the microstructure during laser irradiation process [61]. However, a very high energy laser beam is produced from the KrF excimer laser and it has a flat top profile [62]. Therefore a special optical system was required along

the beam path in order to obtain the desired energy range and beam profile. Figure 3.5 shows the optical path of laser beam from the main excimer laser system to the irradiation on the sample.

The beam produced out from the main laser is controlled by an electronic shutter connected to the main computer. The beam then reflected by the first mirror and passed through attenuator which reduces its initial power. The second mirror reflected the beam to the main optical setup consist series of lens for beam directing and shaping processes. The role of the telescope lenses was to expand the beam to fill the homogeniser lenses. The homogeniser lenses act by breaking up the input beam into many smaller beams towards the cylindrical lenses. These cylindrical lenses modified the incoming beam into desired shape (asymmetrical) then the beam is reflected by the third mirror, passed through the projection lens and reaches the sample stage. The projection lens focuses the beam at a specific distance so that a range of beam sizes could be chosen for the sample irradiation.

The samples were placed on a computer-controlled translation stage which moves in both the x-axis and y-axis. Therefore, during irradiation, the sample can be scanned in two dimensions. Due to the shape of beam profile, there are two different types of sample scanning that can be utilised, namely the high energy leading scanning scheme (HE) and low energy leading scanning scheme (LE). In the HE scheme, during the laser irradiation the sample will experience an abrupt increase in laser fluence, gradually decreases and reduce to zero. In contrast to the HE scheme, in the LE scheme the sample experiences a lower laser fluence first, then slowly increase until it reach maximum peak and finally decreases abruptly to zero.

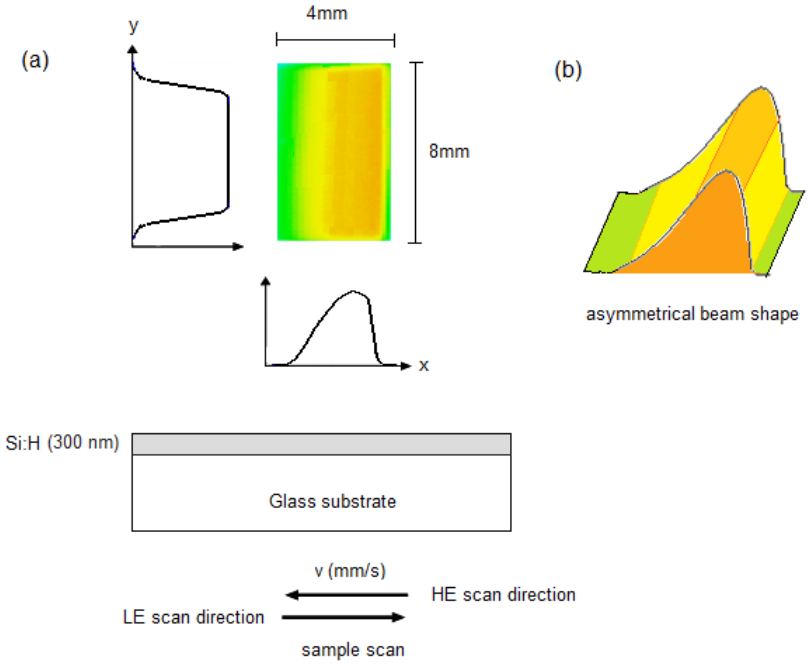

Figure 3.6: Schematic diagram of the output from the KrF excimer laser beam profile, (a) top view and the scanning method, (b) the 3-D illustration of the beam shape.

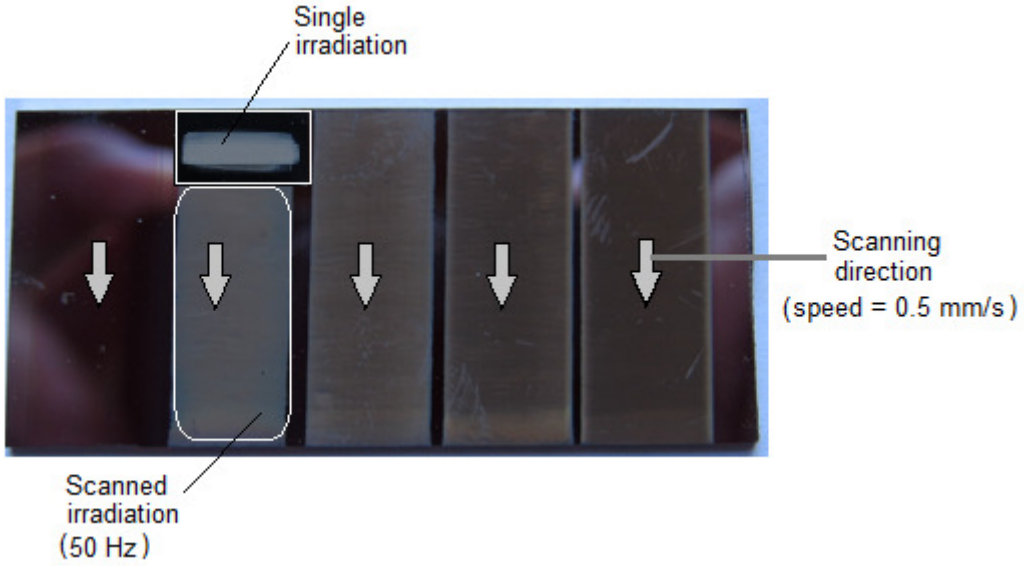

Figure 3.7: Physical appearance of a laser processed sample reveals an area affected by a single irradiation, strips of scanned irradiation, and scanning direction. The applied laser fluences ranging from the lowest value of 131.3 mJ/cm^2 (left) to the highest value of 312.5 mJ/cm^2 (right).

The size of the rectangular beam pattern irradiated on the surface of the films was approximately 4 mm by 8 mm. The a-Si:H films were subjected to multiple pulses (50 Hz) of the laser beam during the irradiation and the sample was scanned along the x-axis at a speed of 0.5 mm/s. The laser irradiation was carried out in air at room temperature and the laser pulse energy was varied between 30 mJ and 130 mJ, delivering a fluence in the range of 98.3 mJ/cm^2 to 443.8 mJ/cm^2. Figure 3.6 (a) illustrate the beam size and sample scanning, and (b) the beam shape in three dimensions. Figure 3.7 shows a real sample image after laser irradiation process.

The given values for the applied laser fluence were only approximations with uncertainty of ±10 mJ/cm^2. This is due to limitation of the excimer laser where some part of the energy was attenuate when the laser pulse travels along the series of lenses.

3.2.3 Scanning Electron Microscope

The scanning electron microscope (SEM) is a powerful imaging system used to study the sample surface topography. The basic principle operation of SEM is analogous to the optical microscope in general, but instead of using visible light, the SEM use a stream of electrons in vacuum to prevent the absorption of electrons by gas molecules. Figure 3.8 illustrates the construction of an SEM. The mechanism behind the SEM starts with the electron gun, which is the source of electrons. These electrons are accelerated from the anode along the main chamber, consisting of a series of electrostatic and electromagnetic lenses. These condense and focus the beam to a very fine point. The beam then passes through a pair of scanning coils,

deflecting the beam in the x and y direction over a rectangular area of the sample. Once the electron beam interacts with the sample, the incident electron is reflected and scattered within an interaction volume resulting in the production of backscattered electrons, secondary electrons and X-ray radiation from the sample.

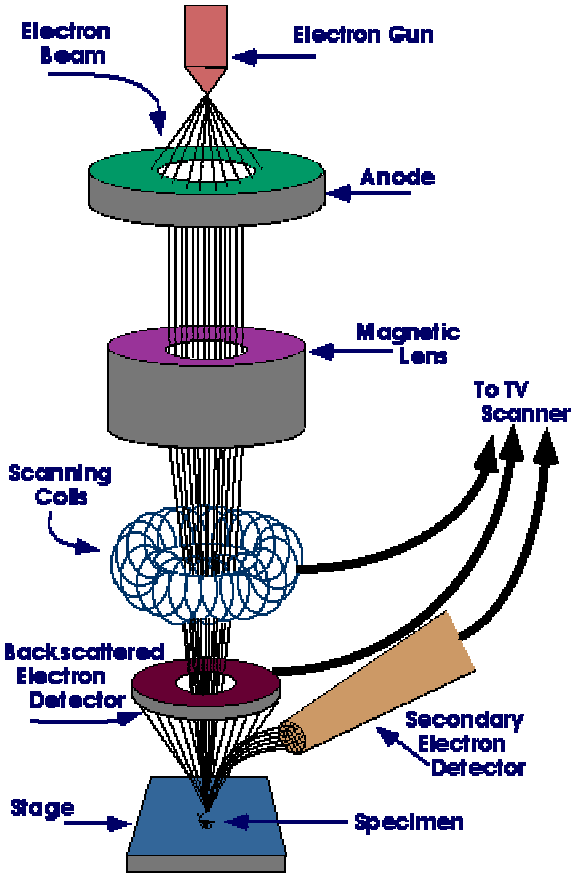

Figure 3.8: Schematic diagram of an SEM, showed here the path of electron beam from the electron gun until it hit the sample [63].

The detectors collect these and convert them to an electronic signal that is finally displayed or stored on a hard disk. The sample is required to be conductive

before placed on the stage inside the SEM. Therefore, 10 nm thin layer of a gold/palladium alloy is sputtered on the surface of the sample to enhance the sample's conductivity by using a sputter coater.

3.2.4 Thermal Modelling

Simulations on the heat transfer during laser irradiation have been carried out to examine the effect of varying the laser fluence and film geometry on the heating, melting and resolidification of amorphous silicon films. Additionally, the results can also be used to predict the effect of laser irradiation on samples with different parameters such as thickness or fluence. All simulations work has been done using COMSOL FEMLAB3.

For the simulation, the laser pulse from KrF excimer laser is considered as a volume heat source. It is in the form of Gaussian function of time and as it reaches the surface of the film, it is absorbed and decays with the sample depth. This type of heat source is represent by,

$$Q(t,x) = Q_0 \exp\left(-\frac{(t-t_0)^2}{\tau^2}\right)\exp(-\alpha x) \qquad (3.1)$$

Where t_0 is the laser pulse peak, τ is the pulse width (FWHM), and α is the absorption coefficient. With $P_{\max}$ as the maximum power, the input optical pulse irradiance is given by,

$$P(t) = P_{\max} \exp\left(-\frac{(t-t_0)^2}{\tau^2}\right) \qquad (\mathrm{W/m^2}), \qquad (3.2)$$

The decay of irradiance into film, with absorption constant α and reflectance loss R at the surface becomes,

$$P(t,x) = (1-R)P_{\max}\ \exp\left(-\frac{(t-t_0)^2}{\tau^2}\right)\exp(-\alpha x), \tag{3.3}$$

Volume heating at depth x (Wm^{-2}) is equal to the rate of loss of beam irradiance with x,

$$Q(t,x) = -\frac{\partial P(t,x)}{\partial x} = \alpha(1-R)P_{\max}\ \exp\left(-\frac{(t-t_0)^2}{\tau^2}\right)\exp(-\alpha x) \tag{3.4}$$

Using the definition of Gaussian integral, $\int_{-\infty}^{\infty}\exp\left(-\left(\frac{z}{a}\right)^2\right)dz = a\sqrt{\pi}$, (3.5)

For incident fluence, Q_a (Jm^{-2}),

$$Q_a = P_{\max}\int_{-\infty}^{\infty}\exp\left(-\frac{(t-t_0)^2}{\tau^2}\right)dt = P_{\max}\tau\sqrt{\pi}, \tag{3.6}$$

Then, $P_{\max} = \frac{Q_a}{\tau\sqrt{\pi}}$ (3.7)

$$Q(t,x) = -\frac{\partial P(t,x)}{\partial x} = (1-R)\alpha\, P_{\max}\ \exp\left(-\frac{(t-t_0)^2}{\tau^2}\right)\exp(-\alpha x) \quad = \alpha P(t,x) \tag{3.8}$$

Finally,

$$Q(t,x) = (1-R)\alpha\frac{Q_a}{\tau\sqrt{\pi}}\exp\left(-\frac{(t-t_0)^2}{\tau^2}\right)\exp(-\alpha x) \quad (W/m^3) \tag{3.9}$$

Equation 3.9 is used to simulate the heat transfer and the results give the heat profile with respect to interaction time t, and depth of the sample x. However it has to take into account that this simulation results will only be valid for the first laser pulse. This is due to the fact that the simulation is merely based on the thermal effects of the laser-material interaction in the initial case. Changes in material properties after the first interaction made the same modelling invalid for the subsequent pulses. In this thesis, discussion will be made on the basis of two different sample structures which are the amorphous silicon film on glass and on metal coated glass substrate. List of parameters used for the simulation are listed in table 3.1.

a-Si:H	
Density	$\rho = 2320$ kgm^{-3}
Specific heat capacity	$Cp = 800$ Jkg^{-1}K^{-1}
Latent heat of fusion	$Hm = 1.5 \times 10^{6}$ Jkg^{-1}
Latent heat of vaporization	$Hv = 13 \times 10^{6}$ Jkg^{-1}
Thermal conductivity	$k = 1.8$ Wm^{-1}K^{-1}
Melting point	$T_m = 1420$ K
Reflectance	$R = 0.65$
Absorption depth	$\alpha = 1 \times 10^{-8}$ m
Molybdenum	
Density	$\rho = 10280$ kgm^{-3}
Specific heat capacity	$C_p = 250$ Jkg^{-1}K^{-1}
Latent heat of fusion	$Hm = 2.89 \times 10^{5}$ Jkg^{-1}
Thermal conductivity	$k = 139$ Wm^{-1}K^{-1}
Melting point	$T_m = 2896$ K

Table 3.1: Detail of parameters used in the heat transfer simulation [64].

3.3 Results and Discussions

3.3.1 Microstructures from Excimer Laser Irradiation

The main parameters for laser irradiation process that will be discussed in this thesis are the laser fluence, scanning scheme, number of pulses and the scanning environment. As discussed in the introduction, surface roughening of amorphous silicon with hillock feature is a common result of the laser irradiation process. However in this thesis, the discussion will cover another significant result from the process, which is the formation of a homogeneous and high density distribution of conical microstructures when the sample is irradiated in air. The figure 3.9 shows the results before and after the laser irradiation on a sample of 300 nm amorphous silicon on 7059 Corning glass. The applied laser fluence was 312.5 mJ/cm^2, at laser frequency of 50 Hz, and the sample was scanned at a speed of 0.5 mm/s. Under these conditions, the surface of the sample has been irradiated with a total of 400 laser pulses. The type of scanning method applied was the HE scheme.

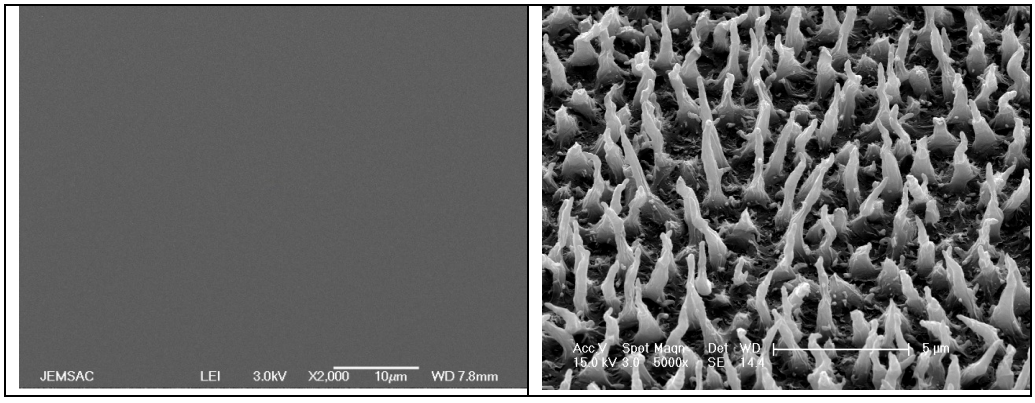

Figure 3.9: SEM images of the 300 nm amorphous silicon film before irradiation (left) and after irradiation (right). The SEM sample stage was tilted at 45^o.

The difference on the surface morphology is very clear for before and after the laser irradiation process. On a macroscopic scale, the non treated amorphous silicon film is brownish in colour, while the irradiated film has a dark grey colour. At the microscopic level, the non treated film has a smooth surface while the laser treated sample shows the formation of tall and sharp conical microstructures with a random distribution. Amorphous silicon has a high absorption coefficient, especially in the UV region. At 248 nm wavelength, the absorption occurs within the film and does not reach the substrate. And at 20 ns laser pulse, the film melts rapidly, and resolidifies as it cools by releasing heat to the substrate and the environment. The conical microstructures are the result of the repetition process of rapid melting and resolidification within a short period of time.

Simulation for the heat profile was carried out to study the heat transfer after the film interaction with single pulse laser. The simulation was made for 300 nm amorphous silicon on Corning 7059 glass substrate. A Laser pulse with fluence of 312.5 mJ/cm^2 was used at 248 nm and of Gaussian shape with FWHM at 20 ns.

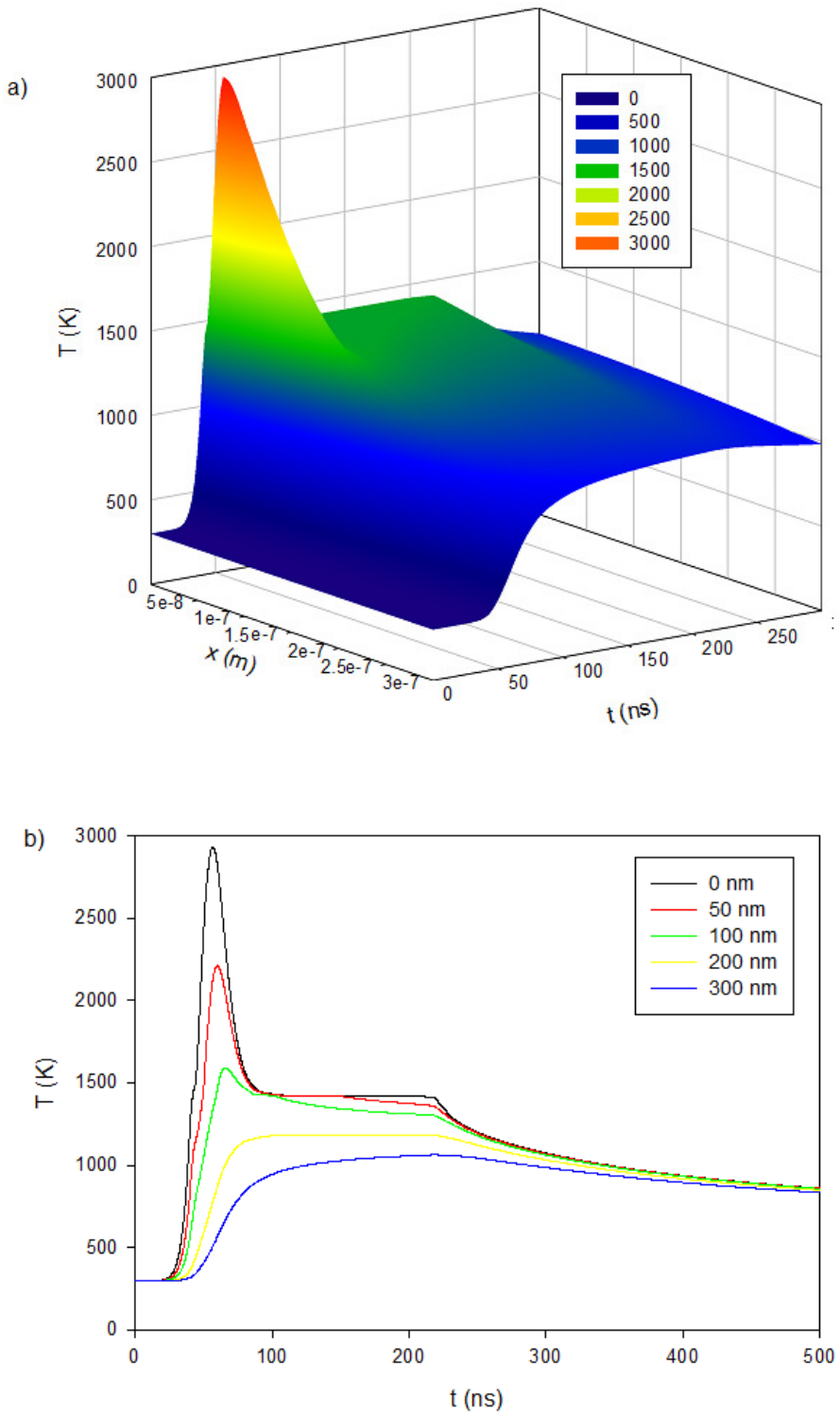

Figure 3.10: Heat profile for fluence at 312.5 mJ/cm^2, (a) in 3-dimensional and (b) 2-dimensional representative at different thickness.

Figure 3.10 (a) shows the thermal time and depth profile results from the simulation. The spike feature which is the temperature region in green to red indicates that melting was achieved at this particular fluence. Figure 3.10 (b) is used to understand further the process after the irradiation. When the laser pulse reached the film, the surface of the film absorbed within 50 ns the incident laser energy. During the absorption process, the surface temperature increased suddenly from room temperature to a maximum temperature of 2900 K within 30 ns. The maximum temperature was reached, followed by a rapid decrease in temperature to 1420 K. The plateau region is associated with the latent heat evolution during the cooling process. Then the temperature is decreased further from the process of heat transfer from the film to substrate and surroundings.

The temperature profile inside the film is different from the surface. Again, from figure 3.10 (b), it is shown that the temperature profile at the depth near the surface at 50 nm follows a similar profile to the surface but with a much lower maximum temperature peak and shorter time for latent heat evolution. With increasing depth of film (at 100 nm), less heat is transferred. At this depth, the maximum temperature only goes up approximately at 1600 K which is a little higher than the melting point of the film and only for a short while. At the depth of 200 nm, it shows that the melting does not occur but the temperature stayed at 1200 K, during the latent heat evolution process at the surface. At a depth of 300 nm, which is at the interface between the film and substrate, the maximum temperature was no more than 1000 K. Therefore, the used substrate was susceptible to a temperature of not more than 1000 K at this particular laser fluence.

3.3.2 Effect from Varying Laser Fluence

(a) F = 93.8 mJ/cm^2	(b) F = 131.3 mJ/cm^2
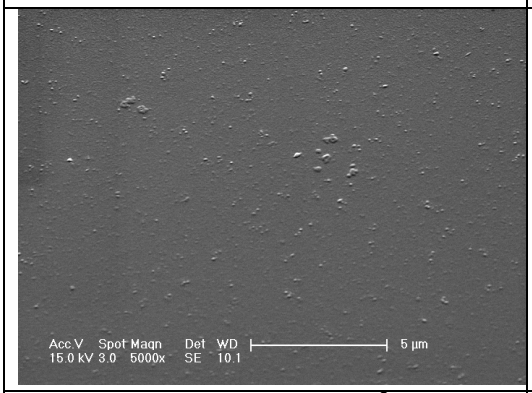	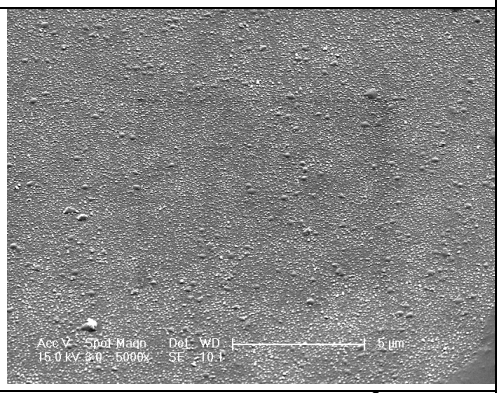
(c) F = 175 mJ/cm^2	(d) F = 218.8 mJ/cm^2
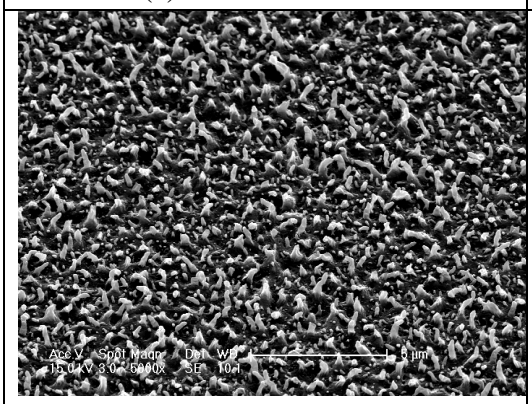	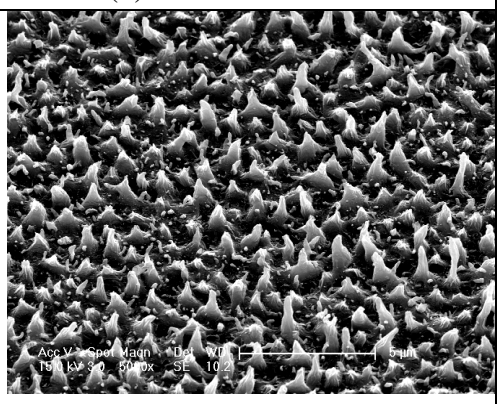
(e) F = 256.6 mJ/cm^2	(f) F = 312.5 mJ/cm^2
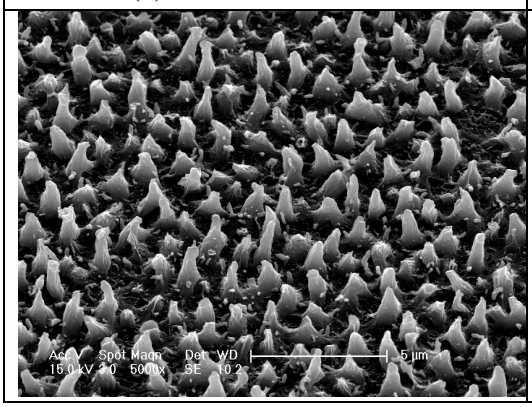	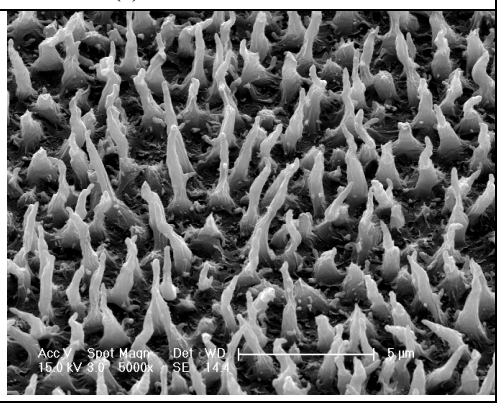

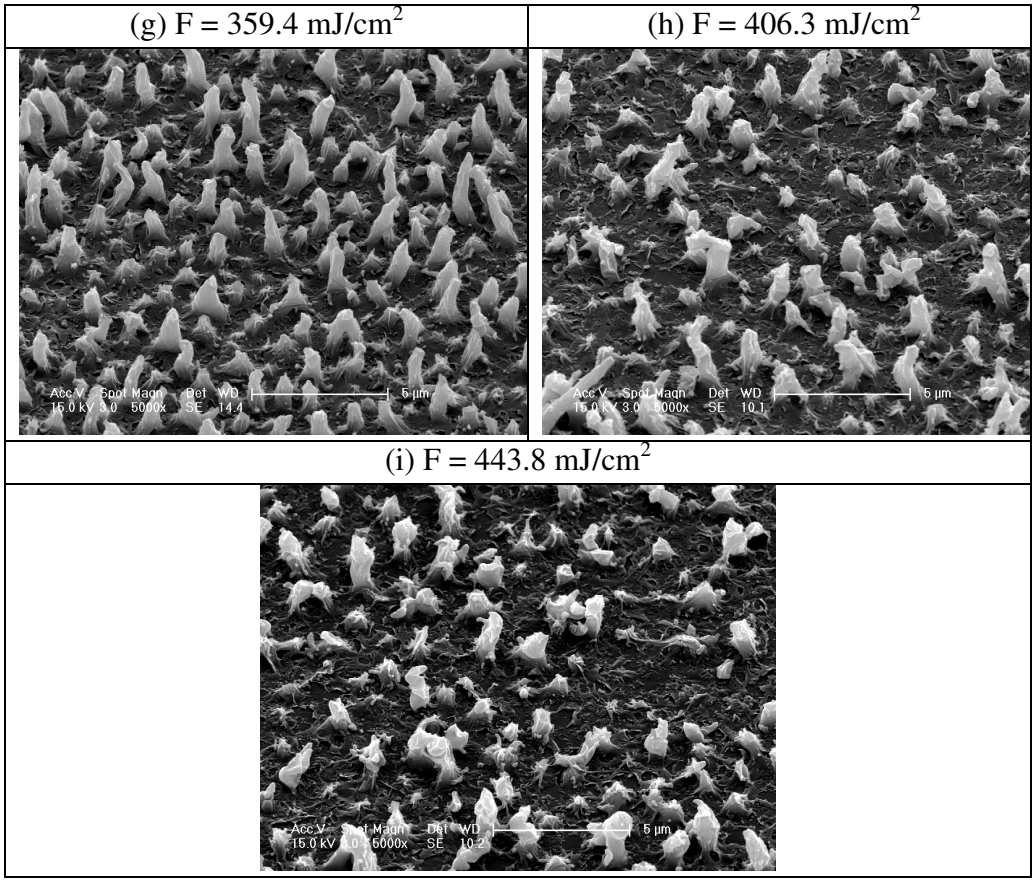

Figure 3.11: SEM images of 300 nm amorphous silicon samples irradiated in air with HE scheme scanning at laser fluence of (a) 93.8 mJ/cm^2 to (i) 443.8 mJ/cm^2.

The effects on the formation of conical microstructure upon different laser fluence are observed by varying the applied laser energy while keeping other parameters fixed. To achieve this, the laser irradiation process is carried out within the laser fluence ranging from 93.8 mJ/cm^2 to 443.8 mJ/cm^2. The SEM images are shown in figure 3.11.

At the first two laser fluences, the surfaces of the films were deformed, and with higher laser fluence effects became more pronounced. The energy provided by

the applied laser fluence was not enough for microstructures to form, although, the films experienced a surface deformation with visible lumps, and the density of these features increased with laser fluences. With all parameters fixed, the microstructures are clearly observed when the laser fluence is at 175 mJ/cm^2. At this point, small features of microstructure were randomly formed with average height of 0.5 μm. With the increase of applied laser fluence, there was a volume expansion with the microstructures becoming taller. However, the density per unit area of the microstructures decreased as more material combined to form larger structures. These trends were repeated with the increase of laser fluences until the largest microstructure was achieved when the laser fluence was at 312.5 mJ/cm^2. At this point, the measured average height of the microstructures is approximately 3 μm. Beyond this point, the size of the microstructures decreases and the density also decreases. This can be explained where, the higher applied laser fluence ablated the film more than the previous fluence. The spaces between each microstructure also increased as the material of the film is ablated. Much higher laser fluence ablated most of the film and exposed the glass substrates underneath.

Thermal modelling was carried out by keeping all parameters fixed and by varying the values of laser fluence. The simulated heat profile of the film surface at different fluence is showed in the figure 3.12. At a laser fluence of 131.3 mJ/cm^2 and lower, the absorbed energy is not sufficient to heat up the surface to a temperature higher than the melting point of the film. This assumption is in agreement with the SEM observation of figure 3.11. The lowest fluence which results in the process of melting is 175 mJ/cm^2. The scanning process leads to the formation of

microstructures as showed in the SEM. The increase of fluence results in a higher peak of maximum temperature achieved at the surface and a longer time taken for the latent heat evolution. For the highest fluence of 443.8 mJ/cm^2, theoretically the surface experienced a maximum temperature of 4500 K leading to the ablation process and degradation of the film further from the substrate as revealed in SEM.

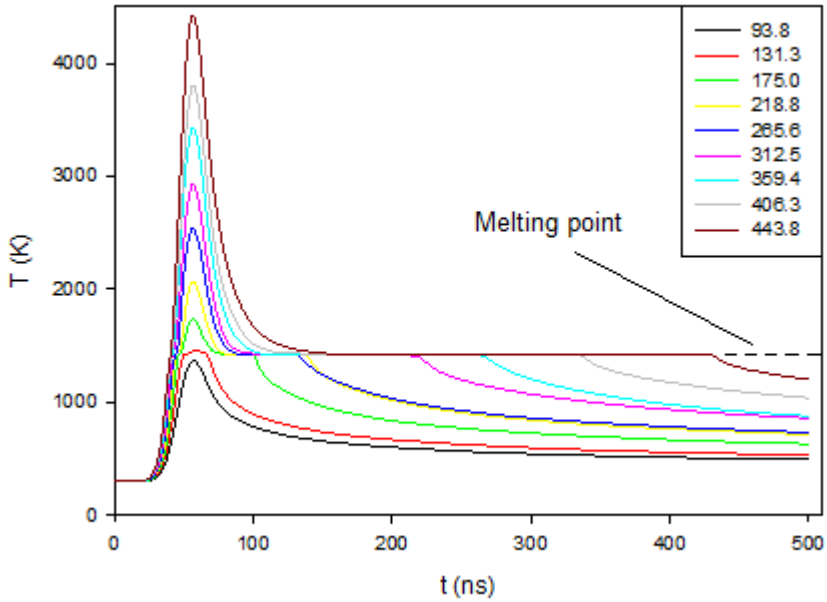

Figure 3.12: Correspondence heat profile of the sample surface as from the figure 3.11.

3.3.3 Effect of Beam Shape Scanning Method

By using another scanning method, the LE scheme, and retaining all other parameters, the results of irradiation with the same laser fluence parameters as before are shown in figure 3.13. The variation in formation of the microstructures on laser fluence are similar to the previous results with the HE scheme. However, the major difference between these two schemes is the shape of the microstructure resulting from the laser irradiation process. In order to observe the effect, a higher resolution SEM was used, with the results shown in figure 3.14. The typical results of the microstructure formed by using the HE schemes are sharp with conical like features. Whereas for the LE scheme, the features of the microstructures are apparently blunt in shape.

The difference in resulting features of the microstructures is the direct consequence of the different heat transfer process between these two schemes. Samples of the HE scheme experienced a sudden increase of heat energy rapid melting and resolidification occurring with a supply of high laser fluence before it was steadily decreased along with the scanning process. On the other hand, with the LE scheme the samples experienced a lower laser fluence before it increased steadily to the elevated temperature. This process allowed the film to be heated up steadily, rather than the abrupt change in the HE scheme case. This should have some bearing on the hydrogen evolution process and on the internal structure of the features. The results from these cases are important as it will give an opportunity to choose two different structures which will become the next subject of the research in this thesis.

(a) F = 131.3 mJ/cm^2	(b) F = 175 mJ/cm^2
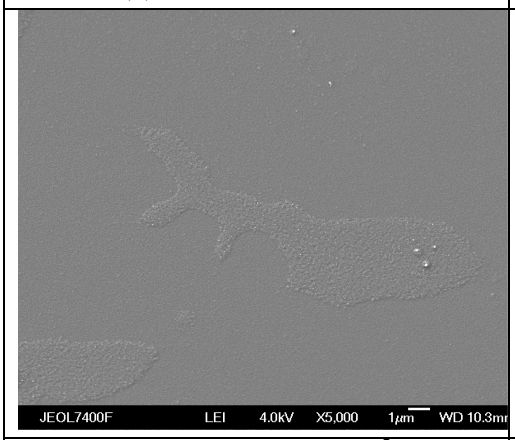	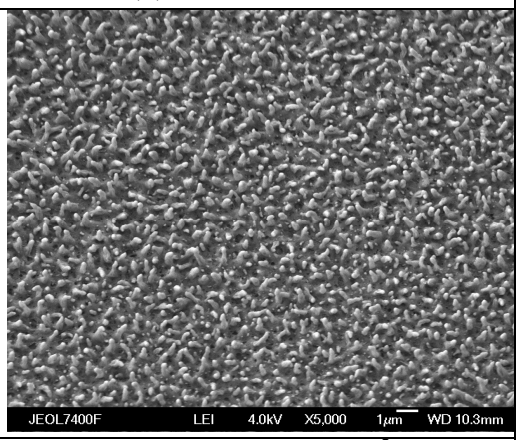
(c) F = 218.8 mJ/cm^2	(d) F = 256.6 mJ/cm^2
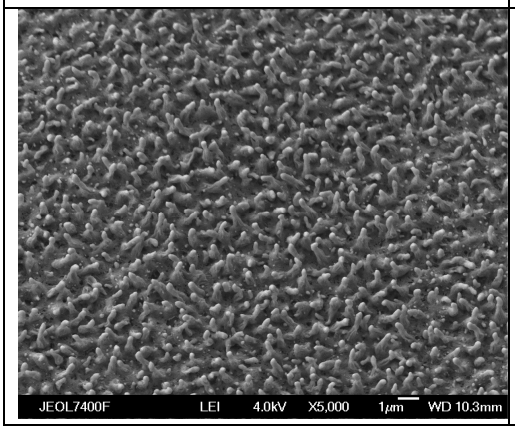	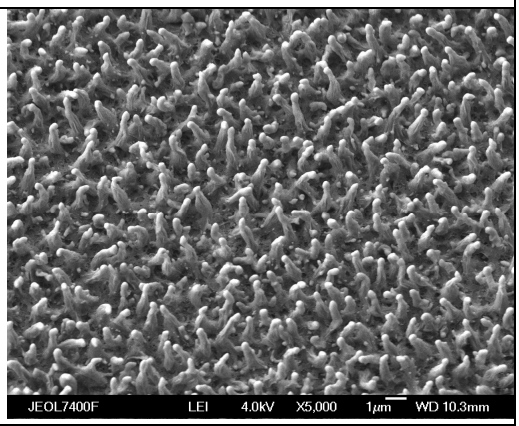
(e) F = 312.5 mJ/cm^2	(f) F = 359.4 mJ/cm^2
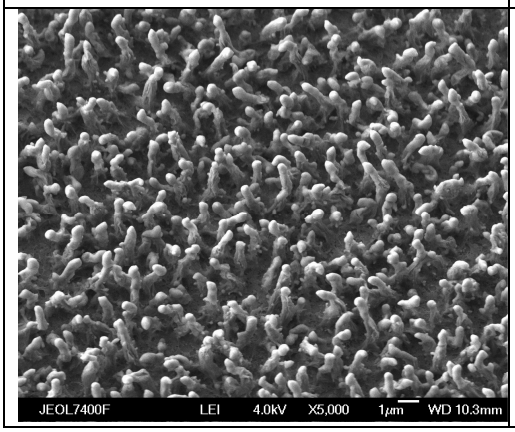	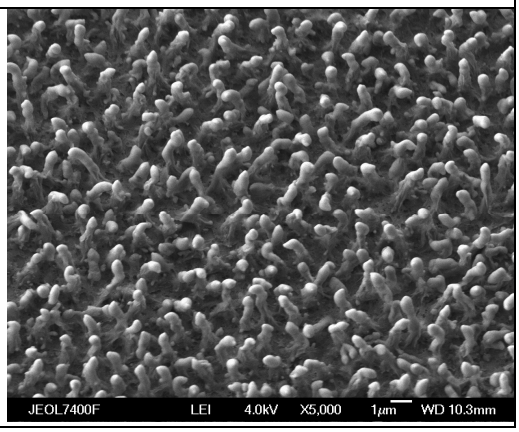

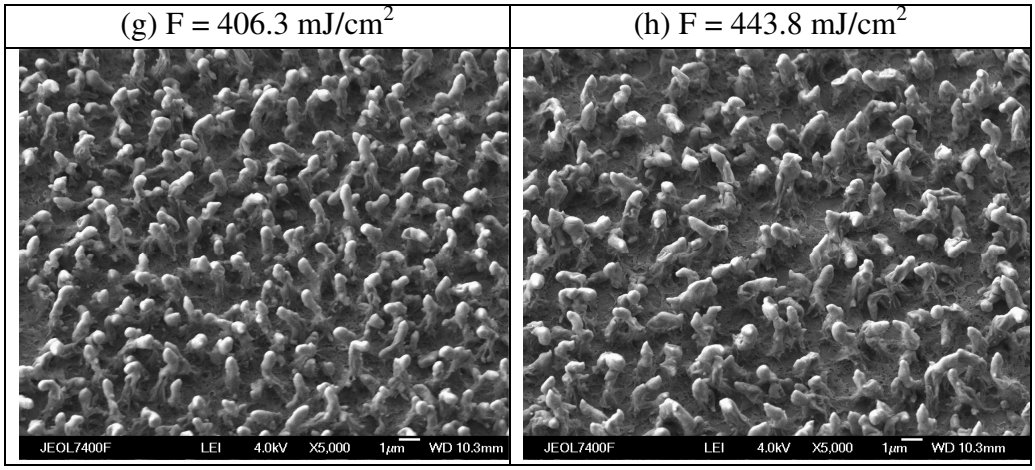

Figure 3.13: SEM images of 300 nm amorphous silicon samples irradiated in air with LE scheme scanning at laser fluence of (a) 131.3 mJ/cm^2 to (h) 443.8 mJ/cm^2.

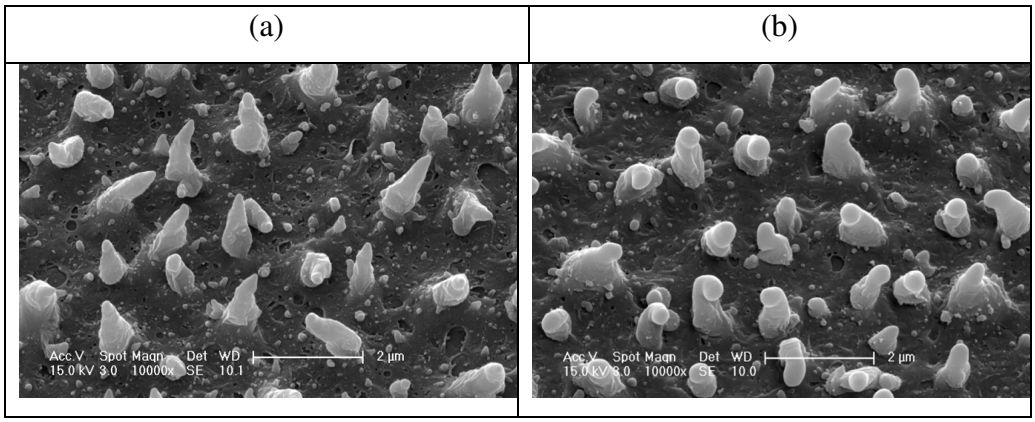

Figure 3.14: Comparison on surface morphology of (a) HE scheme, and (b) LE scheme.

3.3.4 Irradiation on Metal Coated Glass

The purpose of this experiment is to study the effect of the formation of the microstructures with the existence of a thin layer of metal between the film and glass substrate. This type of sample was also designed for field emission measurement to give insight into the internal structure of the features. The metal layer acts as a back contact which realises a cathode structure applicable in display devices. The sample was prepared by sputtering a 200 nm layer of molybdenum on the Corning glass before a 300 nm layer of amorphous silicon was deposited by PECVD.

For the irradiation process, the HE scheme was chosen with other parameters such as scanning speed, laser frequency and irradiation environment are kept exactly the same as in the previous experiment. The range of the applied laser fluence was varied from 93.8 mJ/cm^2 to 443.8 mJ/cm^2. The SEM results from this experiment are shows in figure 3.14. It shows that, except for the first irradiated sample at 93.8 mJ/cm^2 laser fluence, all other irradiated samples result in the formation of microstructures.

(a) F = 93.8 mJ/cm^2	(b) F = 131.3 mJ/cm^2
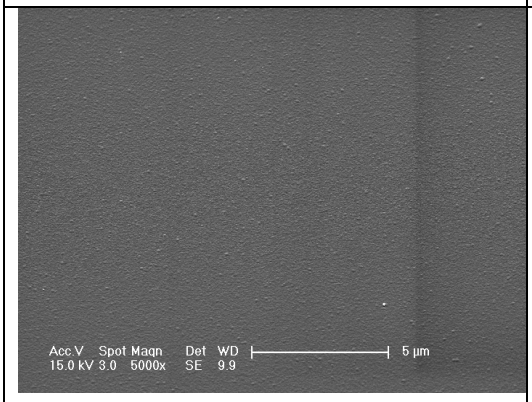	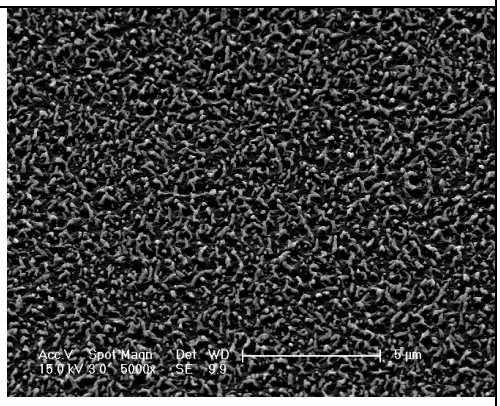
(c) F = 175 mJ/cm^2	(d) F = 218.8 mJ/cm^2
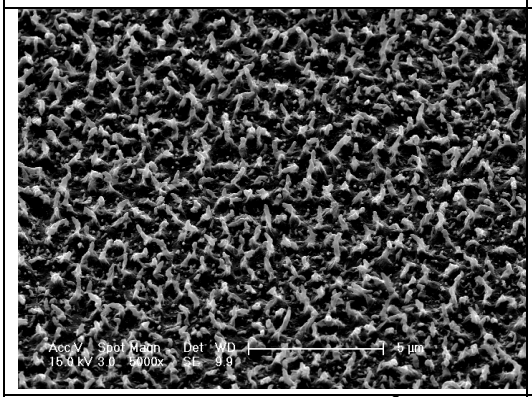	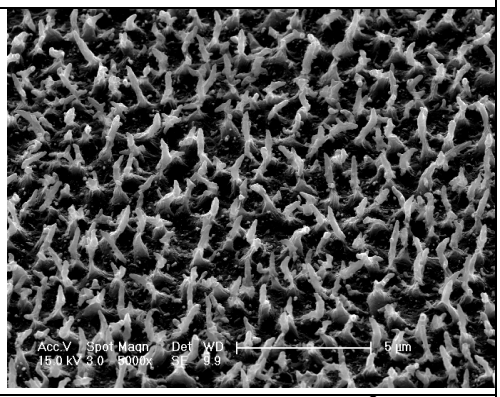
(e) F = 256.6 mJ/cm^2	(f) F = 312.5 mJ/cm^2
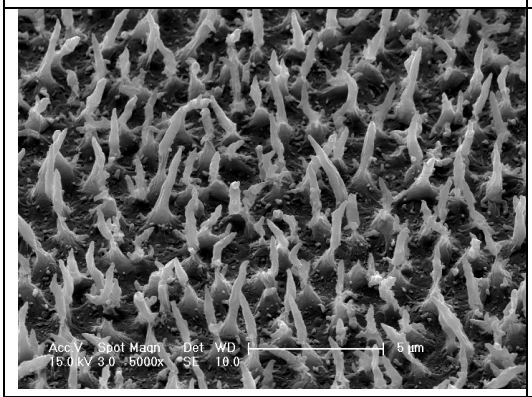	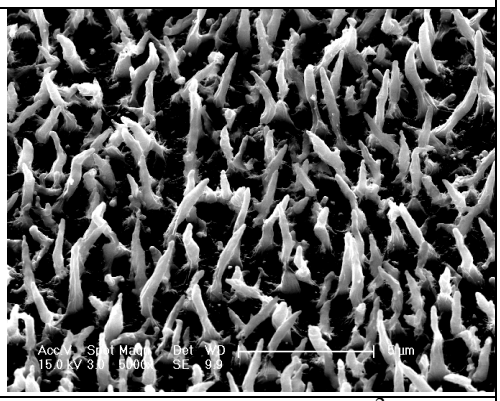
(g) F = 359.4 mJ/cm^2	(h) F = 406.3 mJ/cm^2

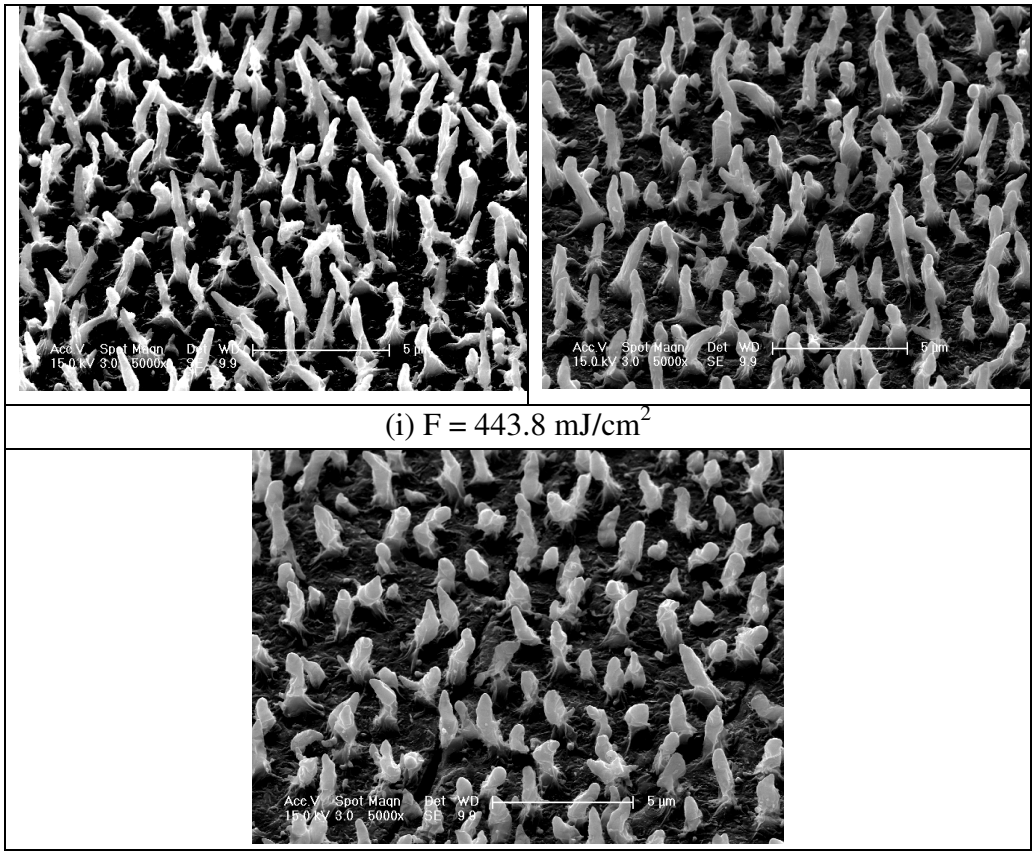

Figure 3.15: SEM images of 300 nm amorphous silicon samples on metal coated glass irradiated in air with HE scheme scanning at laser fluence of (a) 93.8 mJ/cm^2 to (i) 443.8 mJ/cm^2.

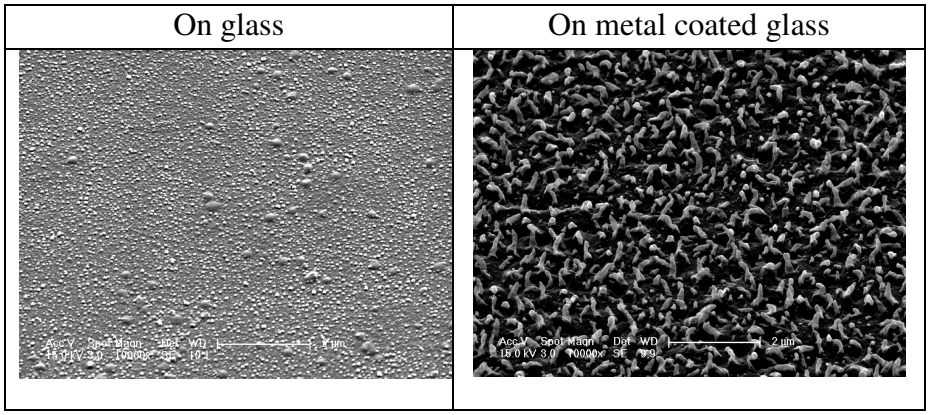

Figure 3.16: SEM images of the 300 nm amorphous silicon film on glass substrate (left) and metal coated glass substrate (right) after irradiation at 131.3 mJ/cm^2 laser fluence. The magnification is at 10000x and sample stage was tilted at 45^o.

The cut off point for the laser fluence to form the microstructure is at a laser fluence of 131.3 mJ/cm^2. Compared to the sample on the glass substrate, at the same laser fluence, the microstructures are not present, except for small protrusions (figure 3.16). Other than that, the shapes of the microstructures are sharp spike-like features, compared to the conical features of the previous samples. Throughout the irradiation process, the sharp spikes are still present although the laser fluence was increased to very high fluence as 443.8 mJ/cm^2. As measured by ImageJ software, the approximate average heights of the spikes are in the range of 3 ± 0.5 μm, similar to the previous case. At very high fluence the ablation process became prominent, affecting the shape of the microstructures to become more blunt and less dense. Apart from that, the irradiation from the high laser fluence also affected the substrate where in the last two samples in figure 3.15, the coated metal underneath the amorphous silicon film was found to be cracked due to the thermal shock.

The variation in the formation of microstructures in this type of sample from the other sample is due to the existence of the metal layer between the film and the glass. Molybdenum is a good conductor, and during laser irradiation this metal layer acted as a heat ballast, where the excess heat was absorbed keeping the temperature of the film maintained at a certain level, before finally released to the glass substrate. Within this condition, the amorphous silicon film is less ablated and significant numbers of microstructures are still present despite the irradiation of high energy fluence.

The thermal modelling for this sample was carried out in similar way to the samples on glass. In the COMSOL software, a 200 nm layer of molybdenum is

placed between the film and glass substrate to replicate the real sample. The simulation was carried out at different laser fluences, from 93.8 mJ/cm^2 to 443.8 mJ/cm^2. The heat transfer profile is shown as in the figure 3.17.

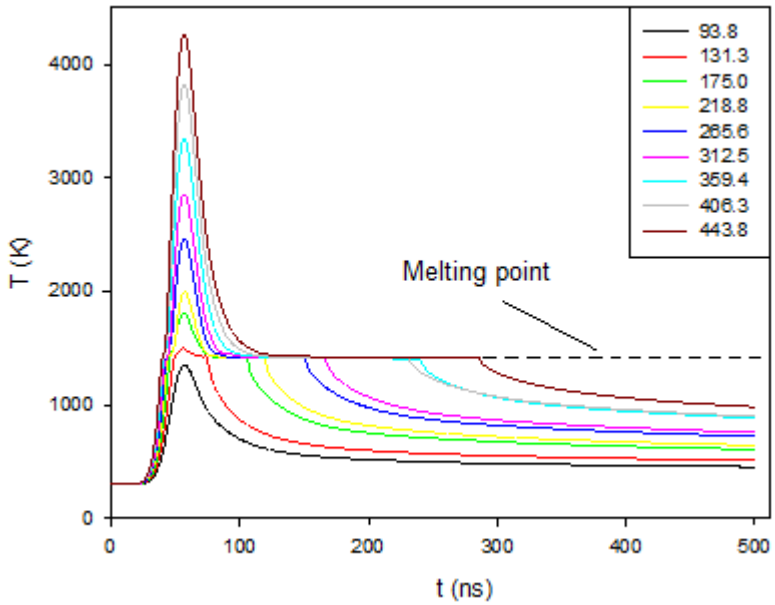

Figure 3.17: Corresponding heat profile of the sample surface as from figure 3.15.

From figure 3.16, it is obvious that the profile for the sample with the metal layer is slightly different from the sample without metal. The thermal modelling indicates that the melting process does not occur for the lowest fluence at 93.8 mJ/cm^2, and for the second lowest fluence at 131.3 mJ/cm^2, the melting process occurred but very briefly. As shown in the SEM micrographs, the microstructure started to form at this fluence. With higher laser fluence, the surface temperature rises quickly, reaches a maximum point and then rapidly cools down to the melting point, similar to the previous case. The clear difference is the time taken for latent

heat evolution which is shorter due to the presence of metal layer as explained earlier.

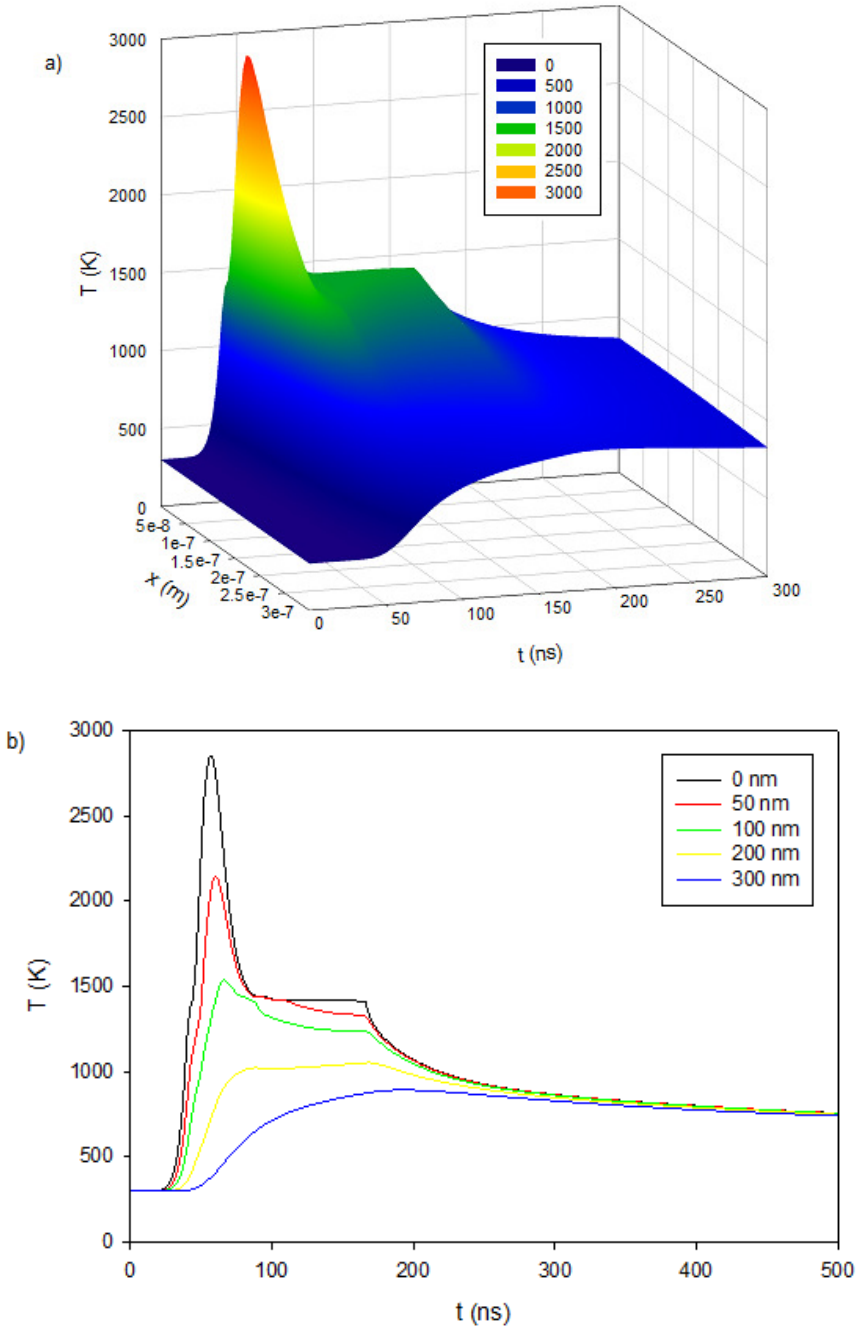

Figure 3.18: Heat profile for sample at laser fluence of 312.5 mJ/cm^2, (a) in 3-dimensional and (b) 2-dimensional representative at different thickness.

The simulation on thermal time and depth profiles at laser fluence of 312.5 mJ/cm^2 is shown in figure 3.18. The features are very much like those of the other sample, although at the same fluence, the melting area is shown to be less. Figure 3.18 (b) reveals further the heat transfer at different film thicknesses. The existence of a metal layer helps to distribute heat further and much more quickly, hence, a lower maximum temperature and shorter time for latent heat is achieved. This observation is also proved and can be seen in the SEM images where the film is less ablated for this sample.

Figure 3.19 shows the heat profile according to different depth of the sample at 150 ns after the irradiation at 312.5 mJ/cm^2 laser fluence. A similar simulation for the sample on glass was plotted coincidently for comparison. The figure reveals that at this particular moment, the film on the surface was melting for both samples. But deeper within the film, the temperature decreased steadily and reduced to 850 K at the interface between metal and the film. The metal layer distributes the heat evenly throughout the entire layer at this temperature. As it reached the glass substrate, the heat transferred evenly further deep inside the glass and the temperature reduced to room condition within less than 1 μm deep.

The heat profile for the sample on glass shows continuity of heat transfer from the surface into the film and finally to the glass substrate. This result was a direct interpretation from the fact that the thermal conduction of the film and the substrate was approximately the same. It also showed that for both samples, the structure experiences a rise in temperature within the depth of 1.4 μm from the surface.

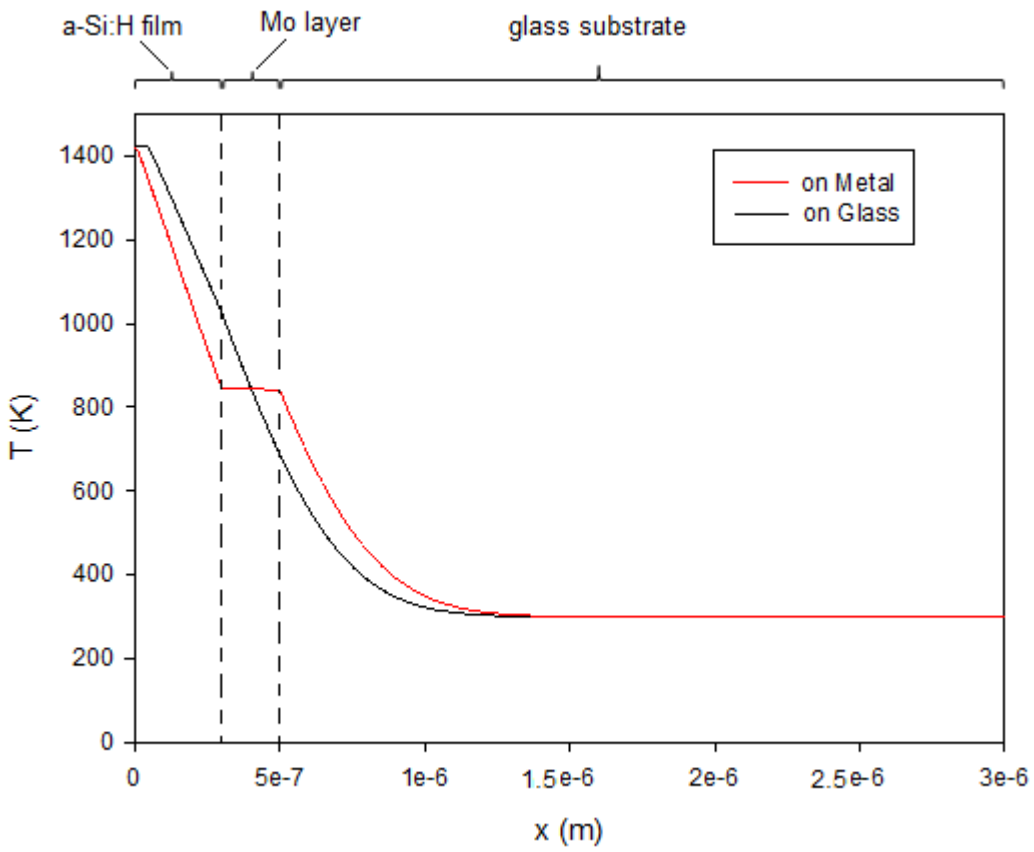

Figure 3.19: Heat transfer at 150 ns after irradiation for fluence at 312.5 mJ/cm^2.

Further discussion will cover a comparison of the surface heat profile and the respective surface morphology for these samples. At low laser fluence, as in the samples of figure 3.20, it is evident that although some heat was absorbed by the films, the sample on glass experienced less of an increase in temperature compared to the sample with metal coated glass. This result was in agreement with the surface morphology after the laser scanning with the HE scheme. At the intermediate laser fluence, as in figure 3.21, the heat profiles for both samples are almost identical, especially for the first 150 ns after laser irradiation. The notable difference was the time taken for latent heat of evolution which was longer for the sample on glass. However, the surface morphology at this fluence is also similar for both samples.

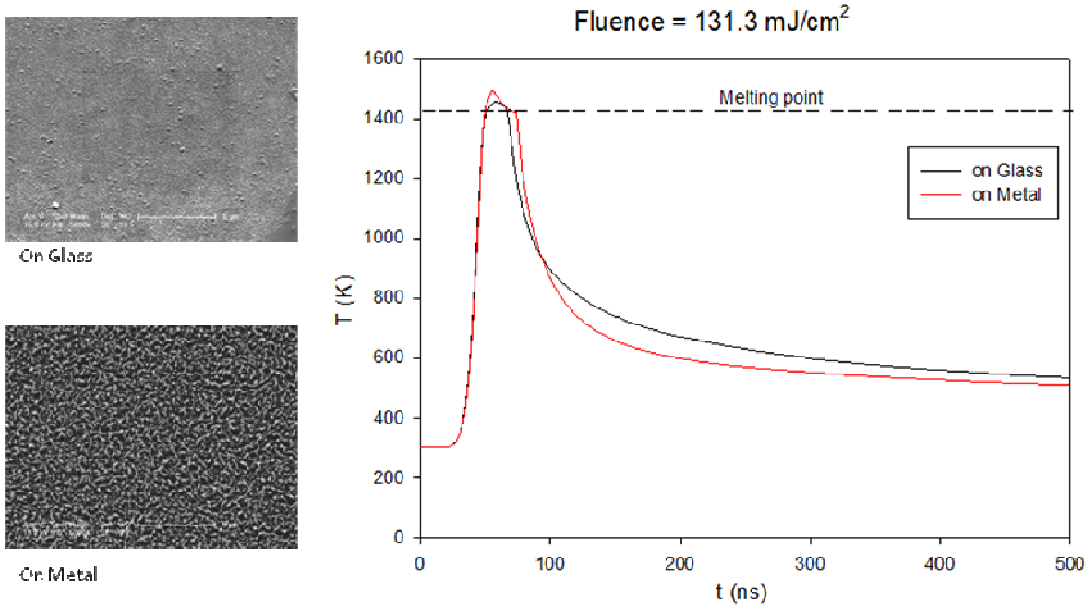

Figure 3.20: Comparison on heat profile between sample on glass and on metal coated glass at low laser fluence of 131.3 mJ/cm^2.

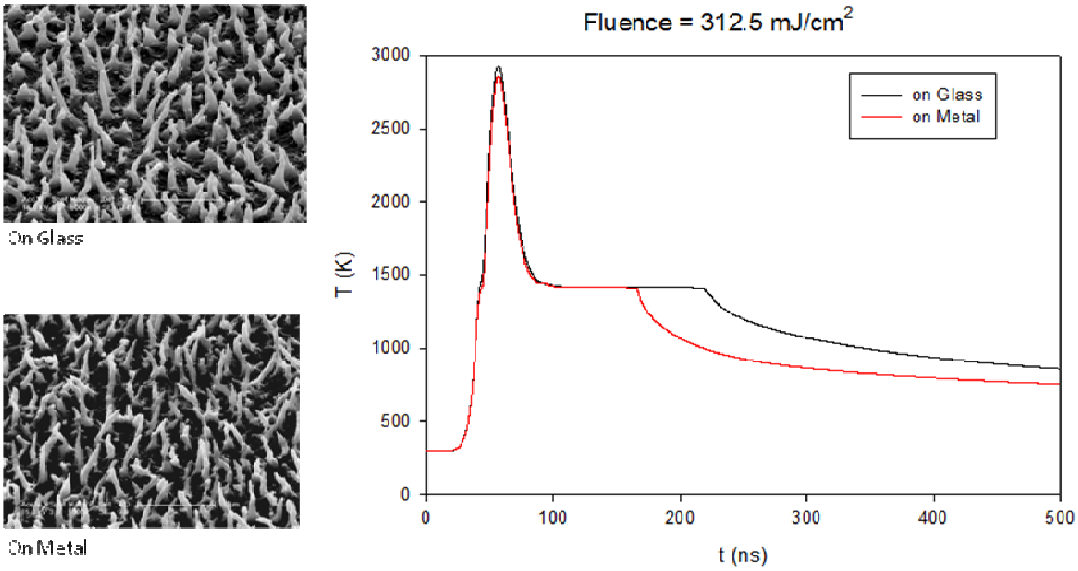

Figure 3.21: Comparison on heat profile between sample on glass and on metal coated glass at intermediate laser fluence of 312.5 mJ/cm^2.

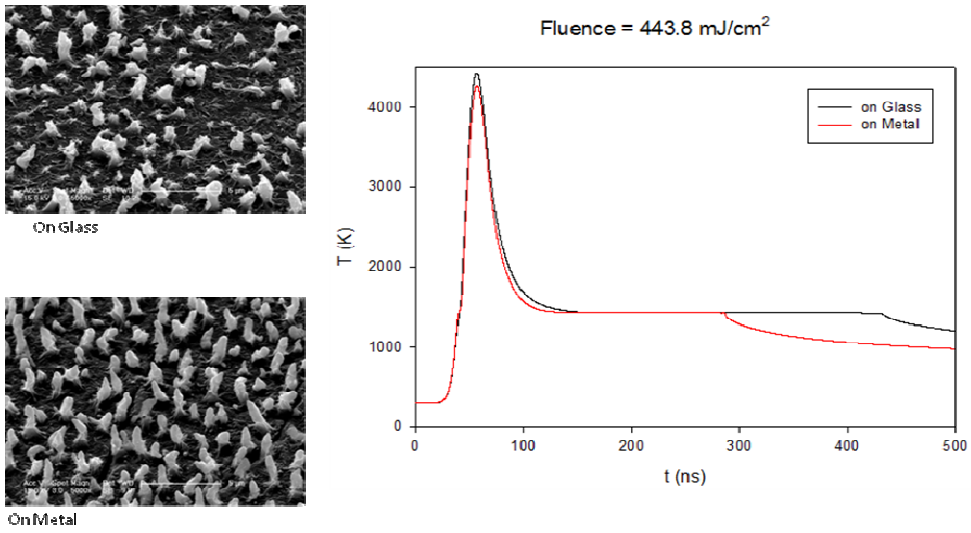

Figure 3.22: Comparison on heat profile between sample on glass and on metal coated glass at laser high fluence of 443.8 mJ/cm^2.

At the highest laser fluence, as in figure 3.22, the heat profiles for both samples are also nearly identical for the first 250 ns after laser irradiation. However, the time taken for latent heat of evolution for the sample on glass was obviously much longer than that of the sample on metal coated glass. The existence of the metal layer clearly affects the final results of the scanning process. This can be seen from the surface morphology studies.

3.3.5 Laser Irradiation in Vacuum

In this section, a study of the effect of the environment towards the formation on the microstructures is carried out. For the previous samples, all of the irradiation processes were carried out in normal atmospheric conditions. Therefore for comparison, the samples were irradiated in the vacuum environment at 10^{-2} millibars. At this pressure, most of the air is pumped out from the irradiation chamber.

A similar sample was prepared with 300 nm amorphous deposited on glass. Two different samples were prepared. The first sample was irradiated with the HE scheme with laser fluence of 131.3 mJ/cm^2 to 256.6 mJ/cm^2, whilst, the second sample was irradiated using the LE scheme at laser fluence of 175 mJ/cm^2 to 312.5 mJ/cm^2. The results are compared directly with those devices irradiated in air at the same fluence.

The SEM images for the irradiation process using the HE scheme are shown in figure 3.23. From the figure, at laser fluence of 131.3 mJ/cm^2, we can see that there is no obvious surface deformation, but at a laser fluence of 175 mJ/cm^2, the surface is modified but not by much. The surface modification becomes more obvious when the applied laser fluence was at 218.8 mJ/cm^2 and beyond.

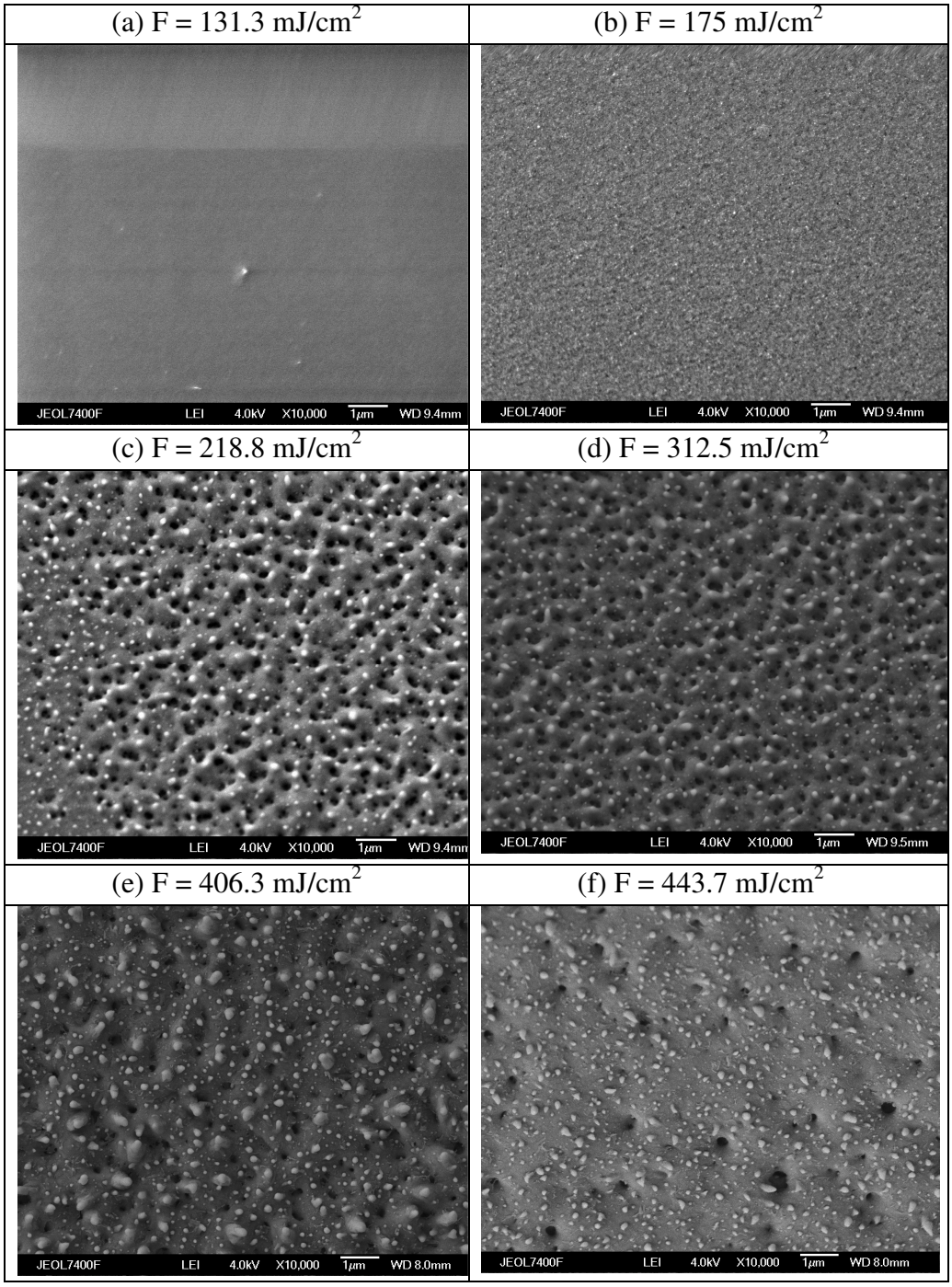

Figure 3.23: SEM images of 300 nm amorphous silicon samples on glass irradiated in vacuum with HE scheme scanning at laser fluence of (a) 131.3 mJ/cm^2 to (f) 443.8 mJ/cm^2.

The surface morphology studies from this experiment reveal a distinct difference between these two processes. A direct comparison of the surface morphology is shown in figure 3.24. The irradiation process in air results in the formation of conical like microstructures at a certain laser fluence threshold. But in vacuum, without the presence of any gas, the microstructures are not formed. Instead, the initial smooth surface of amorphous silicon is deformed into surface with small lumps and pores at the size of 0.1 to 0.2 micron. There is no evidence of the formation of microstructures for the entire fluence range. From this observation, it is believed that the air which mainly consists of nitrogen, oxygen, and water vapour plays a crucial role in the formation of the microstructures. This will be further evidenced by analysis in field emission data that suggests a dramatic internal structural change as discussed in chapter 4.

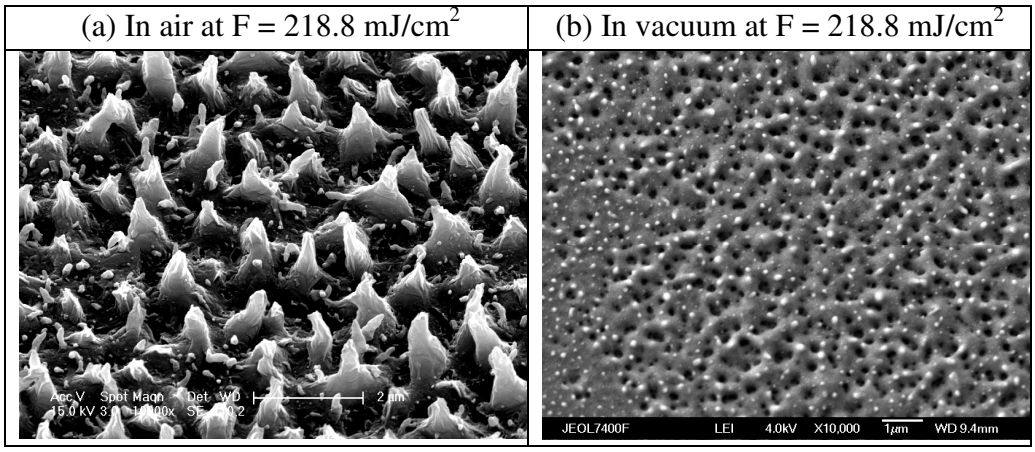

Figure 3.24: Comparison on surface morphology for sample laser process (a) in air, and (b) in vacuum condition at applied laser fluence of 218.8 mJ/cm^2.

For the LE scheme, the SEM results are not significantly different from the HE scheme. As shown in figure 3.25, the surface deformations are quite similar, except that the surface with lumps and pores are formed at higher laser fluence, at 256.6 mJ/cm^2 (compared to 218.8 mJ/cm^2 for the HE scheme). Below this fluence, the surface deformation is not obvious. Therefore it is suggested here that the HE scheme affects the surface of amorphous silicon more than the LE scheme at a given specific laser fluence. This is due to the abrupt heat absorption in HE scheme as opposed to LE scheme.

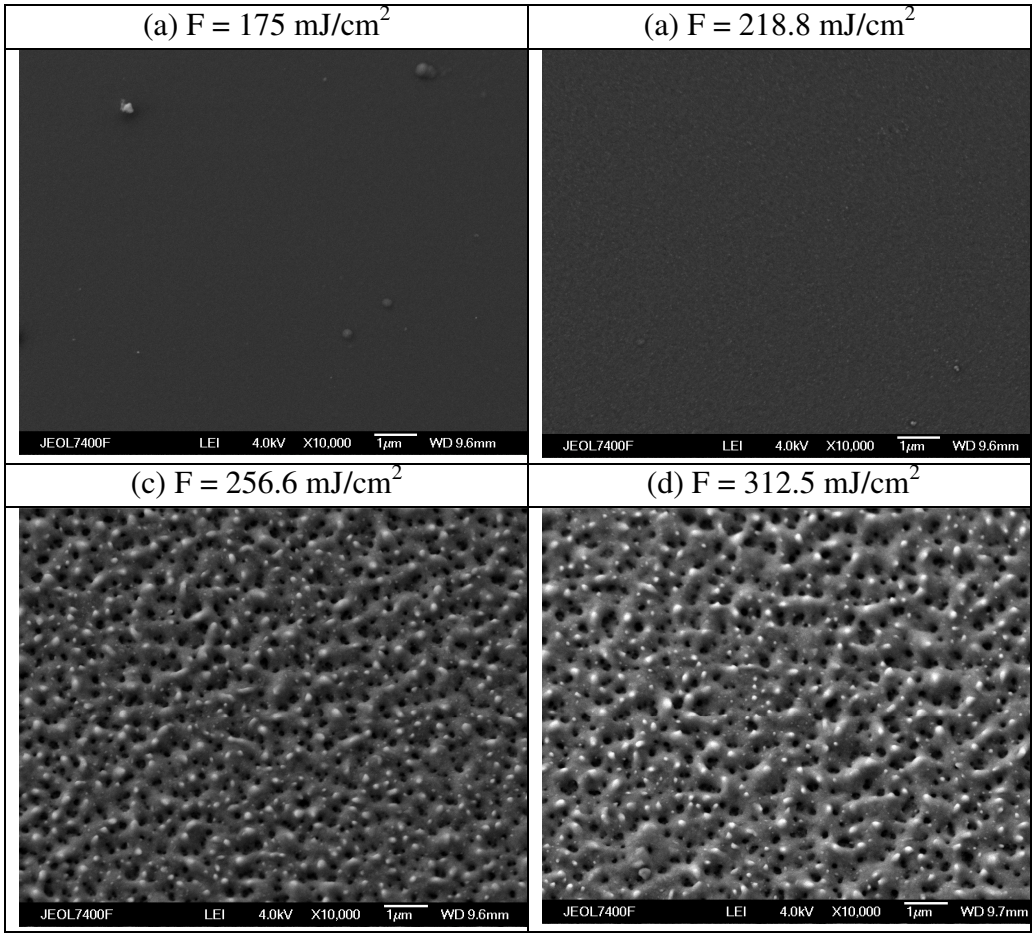

Figure 3.25: SEM images of 300 nm amorphous silicon samples on glass irradiated in vacuum with LE scheme scanning at laser fluence of (a) 175 mJ/cm^2 to (d) 312.5 mJ/cm^2.

3.3.6 Effect upon Single Pulse of Laser

In this section, the intention is to study the effect on the amorphous silicon after irradiation with a single laser pulse. Rather than the scanning method at high frequency as in the previous experiment, only a single laser pulse was set to interact with the amorphous silicon film at a specific location. This experiment will provide the idea of how much the surface is deformed by a given laser fluence. The film was irradiated with varying laser fluence, from lower to higher and therefore the impact of each interaction can be observed.

As shown in figure 3.26, a laser fluence at 131.3 mJ/cm^2 is too low to melt the amorphous silicon film. The film becomes modified at 175 mJ/cm^2, especially near the surface. For a laser fluence at 256.6 mJ/cm^2, the process of rapid melting and resolidification is much clearer to observe and the process goes much deeper. The molten silicon is solidified randomly on top of the film. With a more intense laser fluence, most of the film layer melts to form a much bigger volume of molten silicon, and then resolidifies rapidly.

The results show directly the effect on the absorption process of a single laser pulse when irradiating an amorphous silicon film. The low laser fluence is absorbed by the film but not enough to cause a melting process. As the fluence increases, the surface of the film starts to absorb higher amount of incident laser fluence, enough for melting process to occur. As the pulse duration of the laser is very short (20 ns), the resolidification process follows instantaneously, freezing the shape of the original form of molten silicon. The higher the laser fluence applied to the film, the more energy is absorbed by the film causing the process of rapid melting and

resolidification. The surface modification process is shown to occur on amorphous silicon films after irradiation with a single pulse laser.

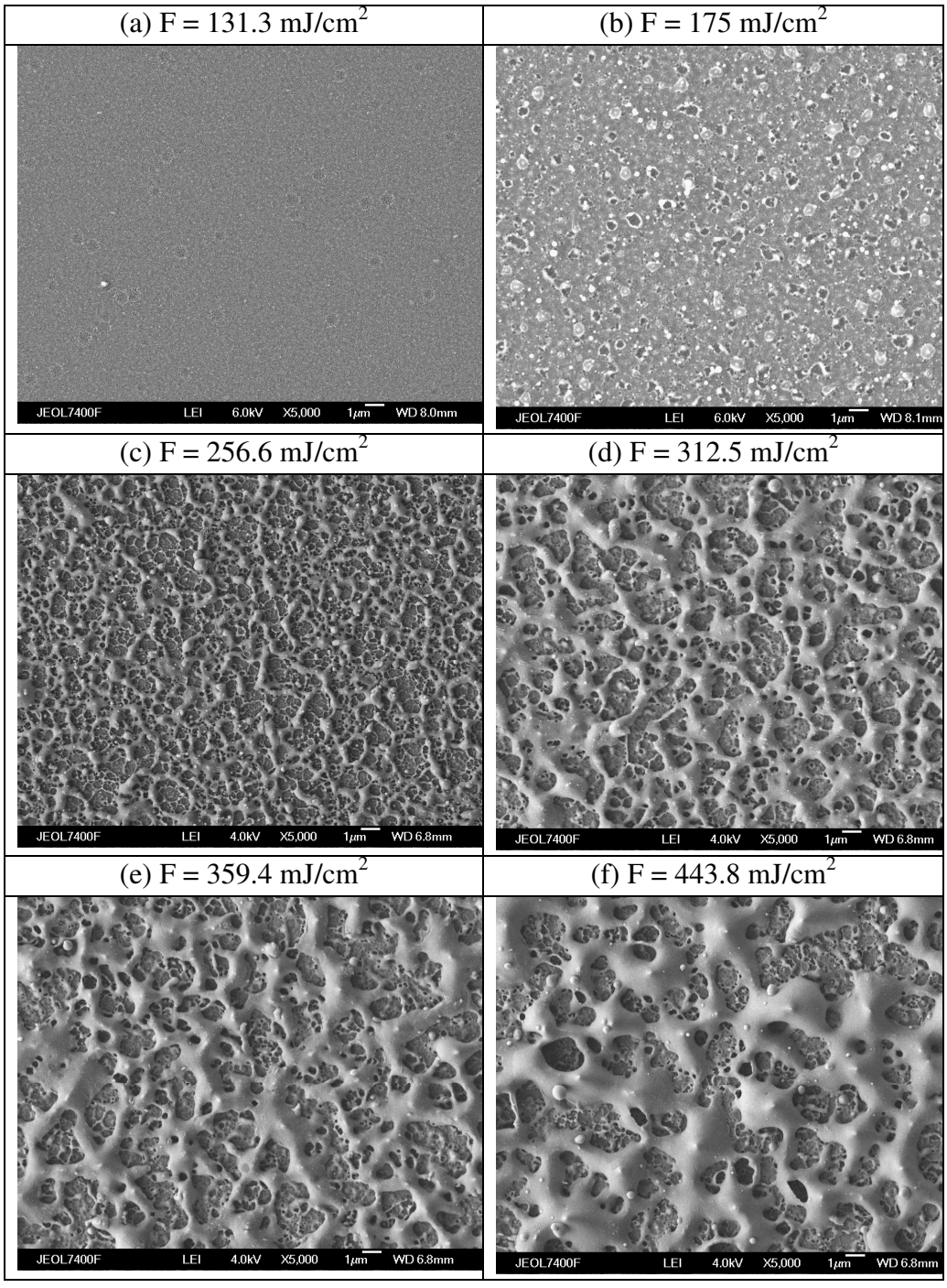

Figure 3.26: SEM images of 300 nm amorphous silicon samples on glass irradiated in air with single pulse laser fluence varies from (a) 131.3 mJ/cm^2 to (f) 443.8 mJ/cm^2.

3.3.7 Effect upon Multiple Pulses of Laser

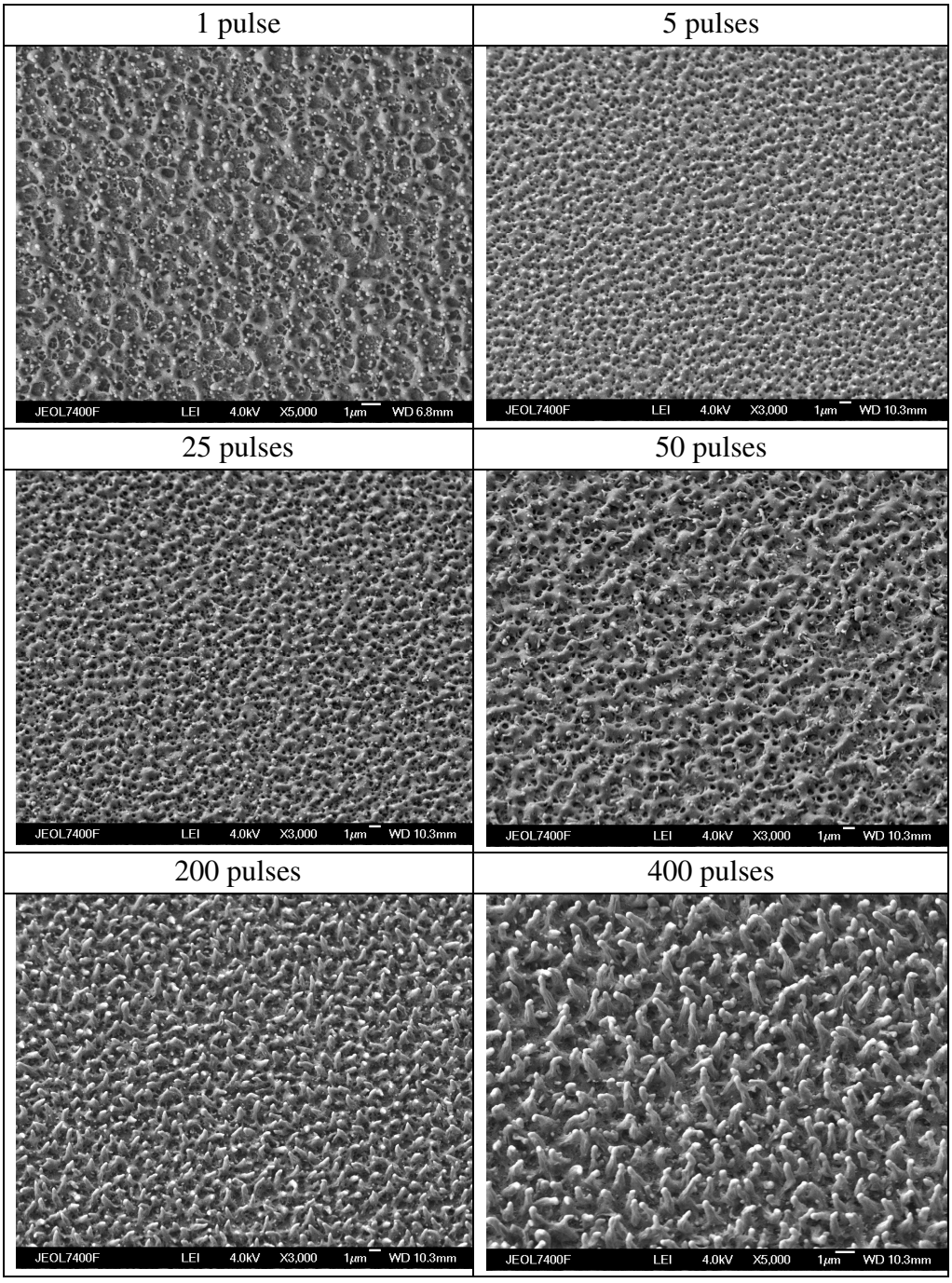

Figure 3.27: SEM images of amorphous silicon samples irradiated in air with variation of applied laser pulse from single pulse to 400 pulses at laser fluence of 256.6 mJ/cm^2.

In the following discussion, the evolution of the surface from the effects upon laser irradiation is showed, starting with a single laser pulse to multiple pulses. The result from this discussion will explain further how the repeated process of rapid melting and resolidification leads to the formation of the microstructures. In this experiment, the laser fluence was fixed at 256.6 mJ/cm^2, the scanning was the LE scheme, and the film was subjected to an increasing number of laser pulses. Different number of pulses was achieved by varying scanning speed of the sample stage or changing the irradiation frequency.

In figure 3.27, the SEM images reveal the surface morphology for 1, 5, 25, 50, 200 and finally 400 pulses of laser irradiation. From this figure, the processes leading to the formation of the microstructures become more obvious. At this laser fluence, the first pulse melts and resolidifies the upper part of amorphous silicon film. During the melting process at very high temperature, some of the hydrogen in the amorphous silicon networks is liberated and some part of the film crystallised. The location of the crystallised silicon then becomes a growth seed for the next crystallisation process. It should be noted here that the absorption coefficient of the film was changed and leads to different absorption profile during the subsequent pulses [65].

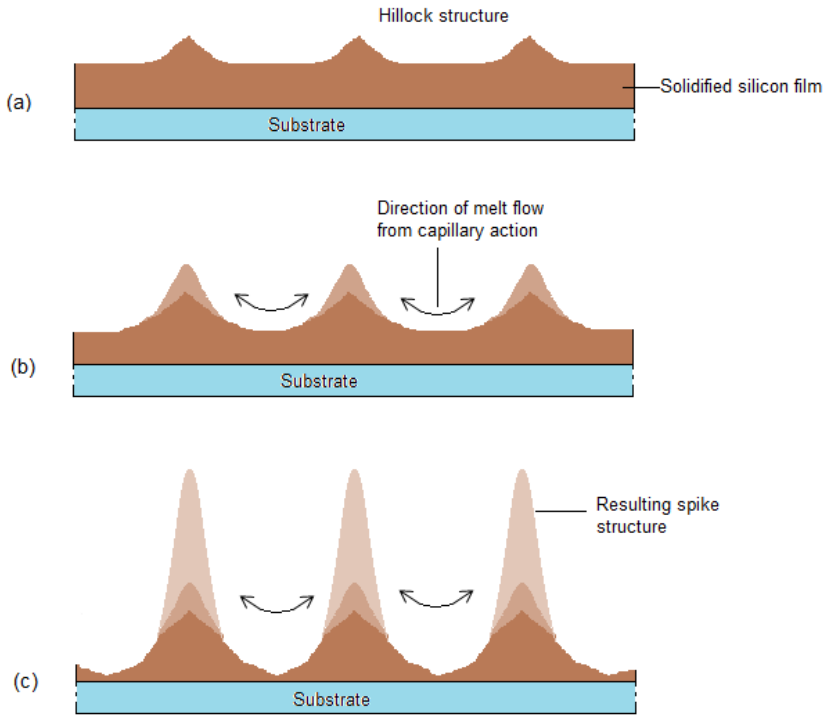

Figure 3.28: The mechanism for the spikes formation. (a) Hillock feature as in the review section. (b) Flow of molten liquid toward the peak contributes to the increase in high. (c) Sharp spike feature at the final stage.

As the number of laser pulses increase, the melting process goes deeper and more bulk film is involved in the melting and resolidification process. It is suggested that during the resolidification process, due to capillary action, the direction of molten silicon is toward the nucleation site which was at a lower temperature. The molten silicon then solidifies as it combines with the pre-existing nucleation growth and contributes to the height increment of the specific nucleation site. This leads to the nucleation site evolving from a hillock and bumpy structure into sharper features. The repetition of this process finally leads to the formation of sharp microstructures

as illustrated in figure 3.28. If the process continues, the entire layer of the film will be used up to reveal the underlying substrate.

3.4 Chapter Summary

In this chapter, it has been shown that laser irradiation of amorphous silicon in air leads to formation of microstructures. Depends on the applied fluence, the microstructures were formed on the scale of 0.1 μm at the threshold fluence to 3 μm at the intermediate fluence. On glass substrates, laser fluence threshold to achieved microstructures was 175 mJ/cm^2 while, on metal coated glass substrates, the threshold was at 131.3 mJ/cm^2. Different type of sample scanning, HE and LE leads to sharp spike or blunt structure respectively. It has been also revealed that the microstructures only formed when the process is carried out in air, but not in vacuum. Thermal modelling was used to simulate laser-material interaction and the results revealed an agreement with the physical experiment.

Chapter 4 Electrical Properties

4.1 Introduction

The application of amorphous silicon is well known in the field of electronics. In the previous chapter, it was demonstrated that various modifications in surface morphology of amorphous silicon film is possible and that these changes can be exploited. This chapter will provide details of the characterisation of electrical properties of these materials in two distinct themes:

a) DC conductivity; and

b) Electron field emission

A brief fundamental review of electrical conductivity and field emission theory will be given first, followed by the experimental techniques used for the characterisation process. Finally an analysis of the results and a discussion will follow.

4.1.1 Electrical Conductivity

One of the basic concepts in the properties of amorphous silicon is the distinction between localised and extended electronic states. At absolute zero, electronic conductivity has contributions only from the carriers in extended states, but not from localised states [22]. The existence of a gap between the valence band and conduction band was proposed as it exhibits a transparent characteristic in the

infrared range spectra [66]. Another feature is the characteristic temperature dependence on electrical conductivity. In crystalline semiconductor, the electrical conductivity as written in the Drude model for a single type carrier system (electron or hole) is,

$$\sigma = e\mu N \tag{4.1}$$

Where, N – carrier density, μ – mobility, written as $\mu = e\tau / m^*$

τ - collision time, and m^* – effective mass

However, for amorphous silicon the explanation of conductivity curves is complex as a result of the existence of continuous distribution $N(E)$ of states and metastability. At any given temperature, carriers generated contribute to the conduction with a mobility $\mu(E,T)$ [67]. The temperature dependence on conductivity is given by the Kubo-Greenwood formula as,

$$\sigma = \int N(E)\mu(E,T)f(E,T)dE \tag{4.2}$$

where, $f(E,T)$ is the Fermi distribution function

For an electron, $N = \int D_c(E)f(E)dE$

where $D_c(E)$ is the density of states in the conduction band.

Under conditions where $E_c - E_f >> kT$, the conductivity can be approximated as,

$$\sigma \approx e\mu N_c \exp[-(E_c - E_f)/kT] \tag{4.3}$$

where, N_c is carrier density in the conduction band

then, $\sigma = \sigma_o \exp(-\Delta E / kT)$ (4.4)

where, $\sigma_o = e\mu N_c$ pre-exponential factor

$\Delta E = E_c - E_f$ – activation energy (E_a)

Therefore, the equation is usually written as

$$\sigma = \sigma_o \exp(-E_a / kT) \quad (4.5)$$

An activation energy can be calculated from an Arrhenius plot of conductivity as shown in figure 4.1. It is also known as thermally activated electrical conductivity for amorphous silicon [66,68]. The characterisation is made by evaluating dark conductivity dependent toward change of temperature in a dc system. The optical gap is often compared with ΔE. The difference between E_o and $E_g = 2\Delta E$ is often interpreted as an activation energy of mobility [66].

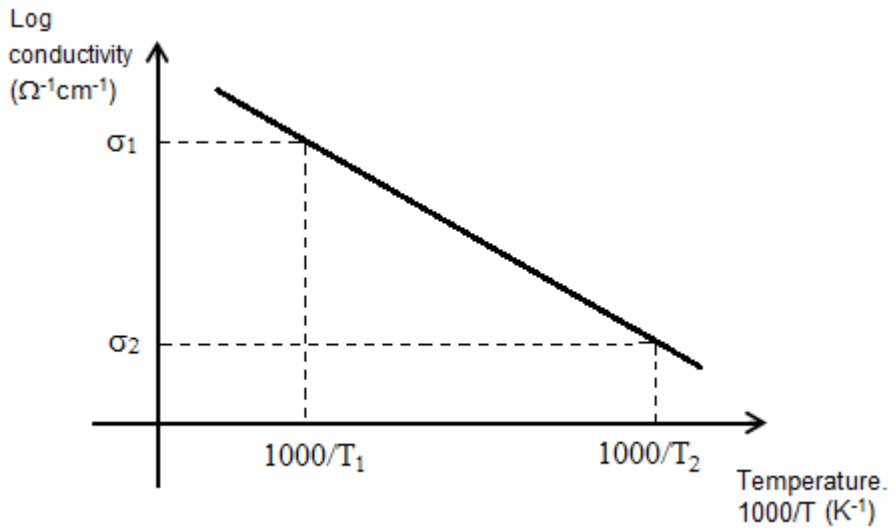

Figure 4.1: Typical Arrhenius plot for dc dark conductivity measurements.

As a semiconductor with a disordered structure, the activation energy of amorphous silicon has a correlation with the pre-exponential factor. From equation 4.5,

$$\ln\sigma = -E_a / kT + \ln\sigma_o \qquad (4.6)$$

The relation of the pre-exponential factor is given by,

$$\ln\sigma_o = E_a / E_{MN} + \ln\sigma_{oo} \qquad (4.7)$$

Where, E_{MN} is a characteristic energy, and σ_{oo} is a constant,

Therefore, the relation is usually written as,

$$\sigma_o = \sigma_{oo} \exp(E_a / E_{MN}) \qquad (4.8)$$

This is known as the equation for the Meyer-Neldel rule. [69-70]. The plot for ln σ_o against E_a is linear relation and it holds universally for many materials including amorphous silicon [71-72].

4.1.2 Electron Field Emission

Electron emission from a cold cathode is known as an alternative technology for flat panel display [73], and microwave vacuum electron devices (MVEDs) [74]. In these devices, a high electric field is applied between cathode-vacuum junction and permits bound electrons to escape from the cathode surface into the vacuum. There are a number of technologies used for the cathode and the typical material used is metal or semiconductor.

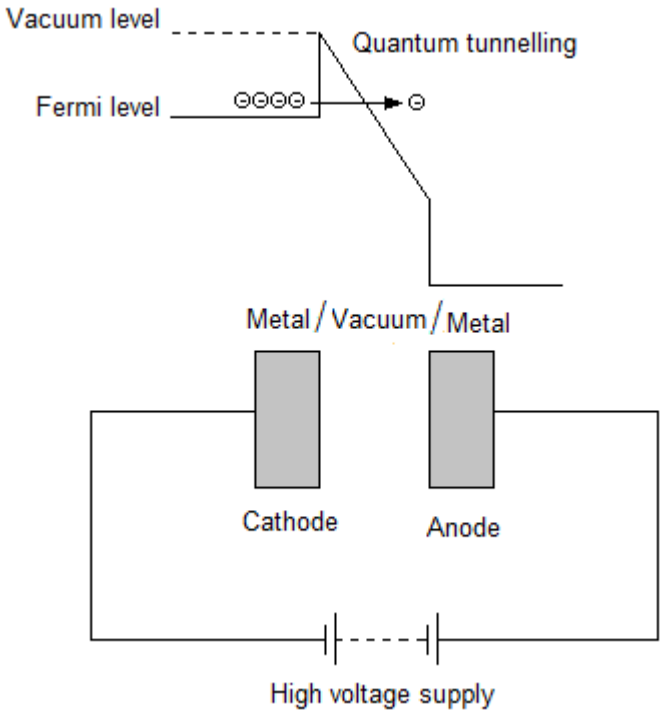

Figure 4.2: Schematic diagram of potential-energy for metal-vacuum-metal structure under the applied of high electric field.

The Fowler-Nordheim approach was used as a common model to explain the process of electron emission by quantum tunnelling [75]. The energy band diagram of a solid state material with the application of electric field between both terminals is showed in figure 4.2. The applied field causes the potential barrier to have a triangular shape and if the field is high enough, the barrier became thinner and electrons can tunnel through this barrier into the vacuum region. The general form of Fowler-Nordheim Model is given by,

$$J = B(\beta E)^2 \exp(-C\phi^{3/2} / \beta E) \tag{4.9}$$

Where, J – emission current density (A/m^2)

B – field-independent constant of dimensions (1.4×10^{-2} A/V^2)

β – field enhancement factor

C – constant (6.8×109 $(eV)^{3/2}V/m^2$)

ϕ – work function (eV)

The enhancement factor β is the ratio between local electric field against the macroscopic electric field and given by,

$$\beta = E_{local} / E_{macro} \tag{4.10}$$

A simplified version of the Fowler Nordheim model was introduced [76] known as Wentzel-Kramer-Brillouin approximation and given as,

$$I = \frac{AB(\beta V)^2}{\phi} \exp(-C\phi^{3/2} / \beta V) \tag{4.11}$$

From equation 4.11, the F-N is expressed in terms of current *I*, applied voltage *V* and emission area *A*. This equation is used to create a Fowler-Nordheim plot which is the plot of log (I/E^2) against 1/E. Ideally this linear plot has the features of a negative slope as the dark conductivity plot. From the Fowler-Nordheim plot, the value of field enhancement factor β can be determined from the linear plot constant where,

$$\text{slope} = -C\phi^{3/2} / \beta \qquad (4.12)$$

The Fowler-Nordheim plot is generally used to explain the electron field emission process. However not all the processes produce the linear plot as proposed by the model. The discrepancy was elucidated further, and it was concluded that this was due to the transition at thermionic emission at low fields and field emission at high field yields to the non-linearity [77]. There are other models as well, used to explain this discrepancy such as space charge induce band bending (SCIBB) [78-80], negative electron affinity (NEA) [81-82], and electrically nanostructured heterogeneous (ENH) [83].

4.2 Experiment Techniques

4.2.1 Conductivity Gear System

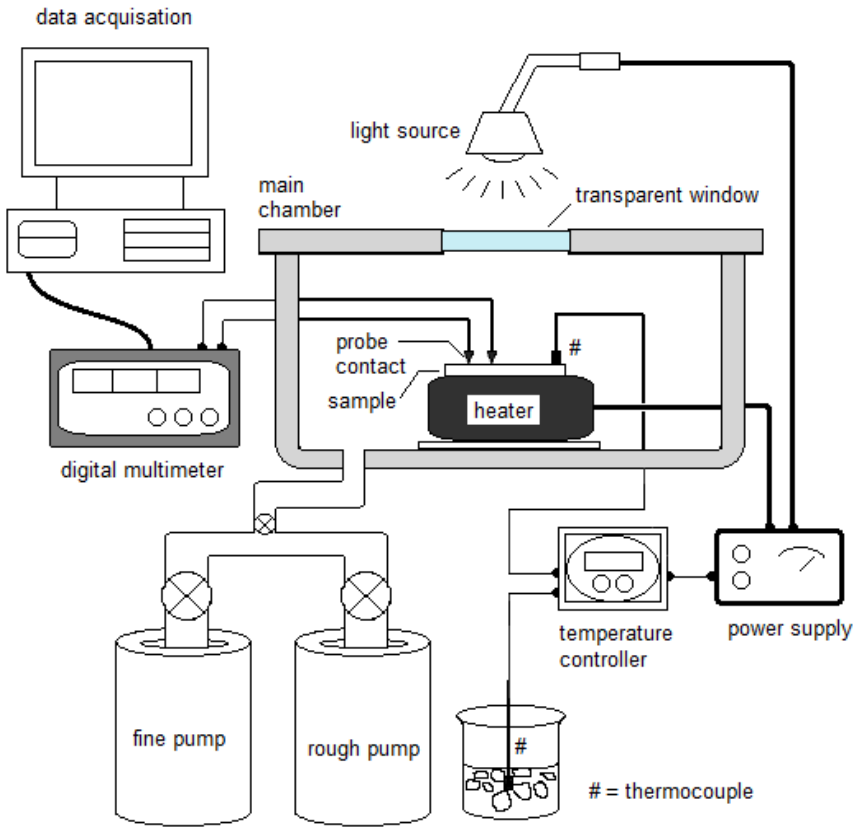

Figure 4.3: Setup for conductivity measurements system.

The instrument for measuring conductivity is shown in figure 4.3. It consists of a main chamber where the sample is placed on a heater block. A metal probe is used to make electrical contact to the sample. A thermocouple is dipped into melting ice as 0 °C as a reference, while the second thermocouple is contacted to the surface of the sample to measure the sample's temperature. Prior to measurement, liquid nitrogen is poured into the cold trap. The vacuum condition is achieved first by

opening the rough pump valve. This pump will bring the pressure down to 10^{-2} millibars. After 5 minutes, the rough pump valve is closed and the fine pump valve is opened. Within 10 minute, a pressure of 10^{-3} millibars can be achieved and the experiment is ready to be carried out. A cold trap system is suitable enough to be used instead of other mechanical vacuum pump since the conductivity measurement only requires low vacuum carbon free conditions.

In this measurement, the data recorded when the temperature is going down. This is because during process of heating up the sample, measurement data shows a non linear character due to the process of sample's annealing. The chosen temperature range is from 20 to 200 °C (293 to 473 K). Within this range, the conductivity profile for amorphous silicon is in the linear region. After the maximum temperature is reached, there is a soaking time where the temperature is kept constant at a maximum of 200 °C for 20 minutes. Then the temperature is gradually decreased back to room temperature. Data for conductivity measurement is collected and saved on a PC connected to the digital multimeter. This whole measurement is done in dark conditions where the light is switched off and the transparent window is covered to prevent light entering the main chamber. After the temperature reaches room condition, the value for the current is taken and noted as dark current I_d. Then the sample is exposed to light by switching a 75 W power bulb. By exposing to light, photogenerated carriers are created and the reading recorded as I_p. The ratio of photocurrent and dark current will be shows in the results and discuss later. At the end of the measurement, the available programme in the PC will shows the plot of conductivity versus temperature. By using a simple command, the slope of the

conductivity plot can be acquired. From this slope, the value of activation energy E_a can be evaluated.

4.2.2 Fixed Gap Field Emission System

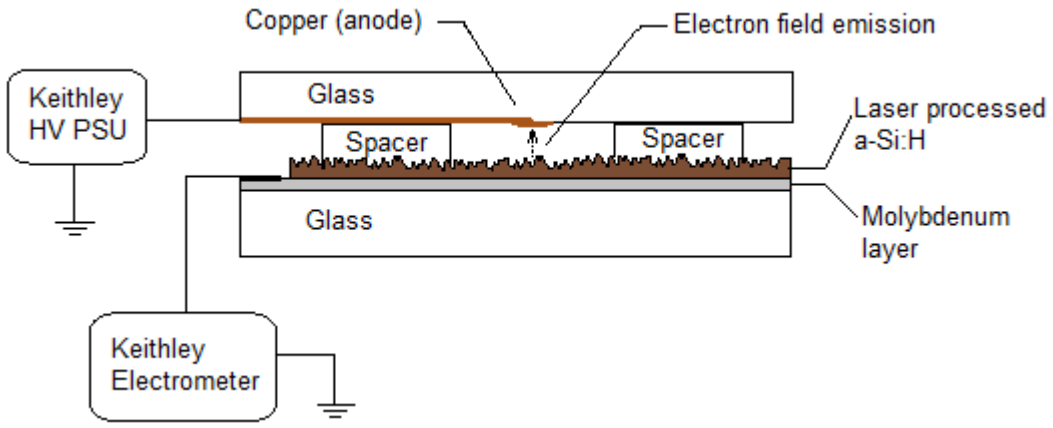

Figure 4.4: Gap structure setup for field emission measurements.

The design of the setup for field emission test is shown in figure 4.4. The anode is a patterned thin layer of copper, made by sputtering a copper target on masked Corning 7059 glass substrate. The anode is placed on top of the sample at a fixed distance by placing the spacer in the middle of the gap. This setup is placed inside a vacuum chamber. A turbo molecular pump is used to pump out the air inside the chamber from atmospheric pressure down to a pressure of 10^{-5} millibars or lower. The anode is connected to a Keithley high voltage power supply which is set to supply the voltage from 0 to 5000 V.

The thickness of the spacer, hence the size of the gap, is 170 μm. Therefore, by definition the electric field between anode and cathode is given by,

$$E = \frac{V}{d} \tag{4.6}$$

$$E = \frac{V}{170} \quad \text{(V/μm)}, \tag{4.7}$$

The initial applied voltage is 50 V and the increment step is also 50 V. The electron emission occurs after the threshold voltage is reached. Its value depends on the properties of the sample itself. Then the voltage is increased until a fairly high maximum current is achieved or the applied voltage is reached at 3000 V. Therefore, the maximum electric field is restricted within a range below 18 V/μm. After the maximum voltage is reached, the emission current is recorded in a similar way by reducing the applied voltage until the lowest possible current is acquired. The step in increasing the applied voltage to a maximum and the reducing it to minimum is carried out for another cycle and the value of the emission current at each increment it recorded. The plot of the emission current *I* versus electric field *E* is plotted and it will shows the field emission characteristic of particular sample.

4.2.3 Samples Preparation

The sample for conductivity measurement required no conductor layer between amorphous silicon film and glass substrate. Therefore, only samples without a metal layer were prepared for this experiment. Similar to those in the previous

experiment, a 300 nm was deposited on Corning 7059 glass substrate by PECVD. Laser processing was carried out and the sample subjected to irradiation at a laser fluence of 131.3, 175, 218.8, 256.6, and 312.5 mJ/cm^2 in the HE scanning scheme. Another sample was produced in a similar way and subjected to the same laser fluence. For comparison, the second sample used the LE scanning scheme during the laser irradiation. As shown in figure 4.5, a top gap metal contact for each irradiated area was made by sputtering 100 nm Al with the help of a shadow mask to form a custom shape contact. The metal contact had a length of 6 mm and separated by a 1 mm gap distance. Prior to measurement, the sample was placed on the heater block in the main chamber and the probe contact brought down to touch the metal contact. Silver paste was applied to the contact point to enhance the electrical conduction between the contacts. A thermocouple probe was also placed on the sample with silver paste at the contact point. The pumping process was carried out down to a pressure of 10^{-3} millibars.

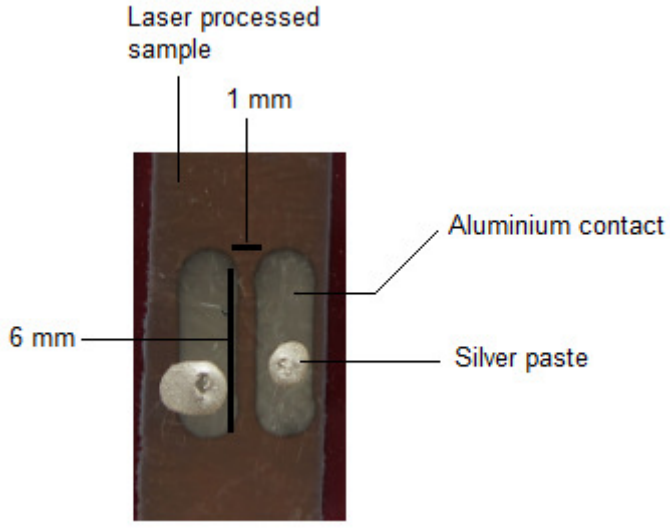

Figure 4.5: Typical sample preparation for conductivity measurement. Both contact is 6 mm length and separated by a gap with 1 mm width.

For field emission measurements, the sample is required to have a conductive layer at the bottom. Thus, a sample with metal coated glass was chosen for the whole experiment. The sample was prepared by coating a Corning 7059 glass substrate with 200 nm molybdenum by sputtering. Then, 300 nm of amorphous silicon was deposited on top of metal layer by PECVD followed by laser irradiation in air. For this process, the laser fluence was set at 131.3, 175, 218.8, 256.6, and 312.5 mJ/cm^2 in the HE scanning scheme. Another sample was produced in similar way and subjected to the same laser fluence but with the LE scanning scheme. The third sample was produced in a similar way but for laser irradiation and the process is carried out in vacuum condition at a pressure of 10^{-2} millibars.

4.3 Results and Discussion on Conductivity Measurements

4.3.1 Dark Conductivity Profile

A sample of untreated 300 nm thick amorphous silicon on Corning 7059 glass was measured, followed by measurements on samples with laser fluence at 131.3, 175, 218.8, 256.6, and 312.5 mJ/cm^2 in the HE scanning scheme. The Arrhenius plots of the thermally activated dark conductivity for all the samples are shown in figure 4.6.

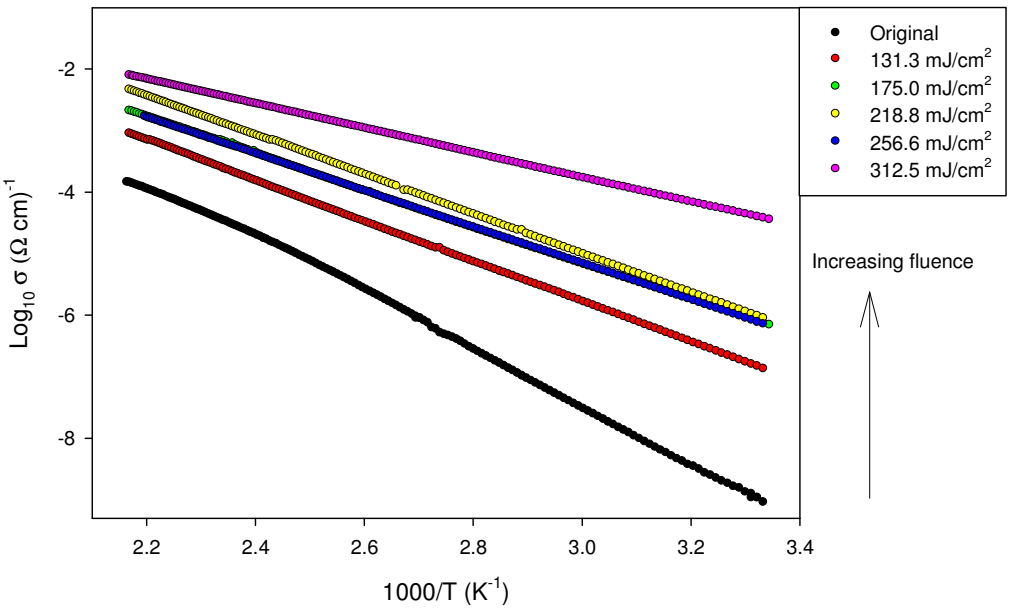

Figure 4.6: Arrhenius plot for 5 different samples irradiated with HE scheme and compared to the plot for the original sample.

As the applied fluence increase, the activated nature of crystallised silicon moves further away from the original. The sample at laser fluence of 256.6 mJ/cm^2

had a slope similar with sample at 175 mJ/cm^2. And as expected, the slope for the sample with the highest applied laser fluence shows almost flat feature (small activation energy), compared to the rest of the samples.

An Arrhenius plot for the LE scheme sample is shown in figure 4.7. The plot for the LE scheme samples shows a similar pattern to HE scheme. The sample with the lowest applied laser fluence also has a slope closer to the original sample. And the sample with the highest applied laser fluence has the shallowest test slope.

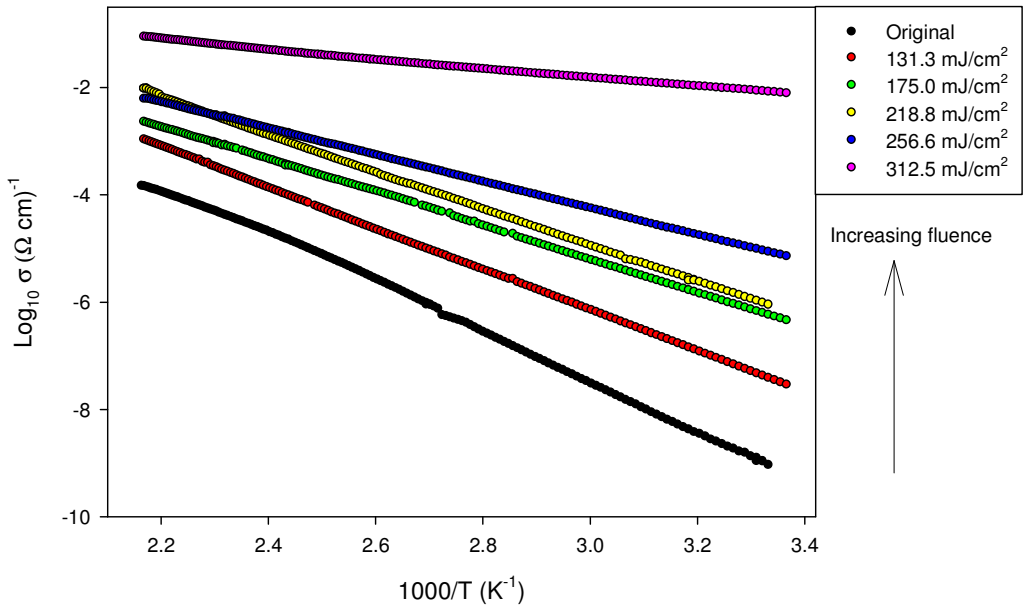

Figure 4.7: Arrhenius plot for 5 different samples irradiated with LE scheme and compared to the plot for the original sample.

(a) HE Scheme			
Laser Fluence (mJ/cm^2)	σ_{RT} $(\Omega\ cm)^{-1}$ [T = 300K]	σ_T $(\Omega\ cm)^{-1}$ [T = 450K]	Ratio σ_T/σ_{RT}
0	1.19E-04	1.79E-02	150.75
131.3	1.04E-03	4.05E-02	39.06
175.0	2.18E-03	5.88E-02	26.90
218.8	2.35E-03	8.17E-02	34.71
256.6	2.14E-03	5.78E-02	27.03
312.5	1.20E-02	1.10E-01	9.16

(b) LE Scheme			
Laser Fluence (mJ/cm^2)	σ_{RT} $(\Omega\ cm)^{-1}$ [T = 300K]	σ_T $(\Omega\ cm)^{-1}$ [T = 450K]	Ratio σ_T/σ_{RT}
0	1.19E-04	1.79E-02	150.75
131.3	6.00E-04	4.18E-02	69.58
175.0	1.94E-03	6.05E-02	31.10
218.8	2.35E-03	1.05E-01	44.69
256.6	6.28E-03	9.72E-02	15.49
312.5	1.24E-01	3.27E-01	2.63

Table 4.1: Data of electrical conductivity at 300 and 450 K and their ratio at various laser fluences for HE scheme (a), and LE scheme (b).

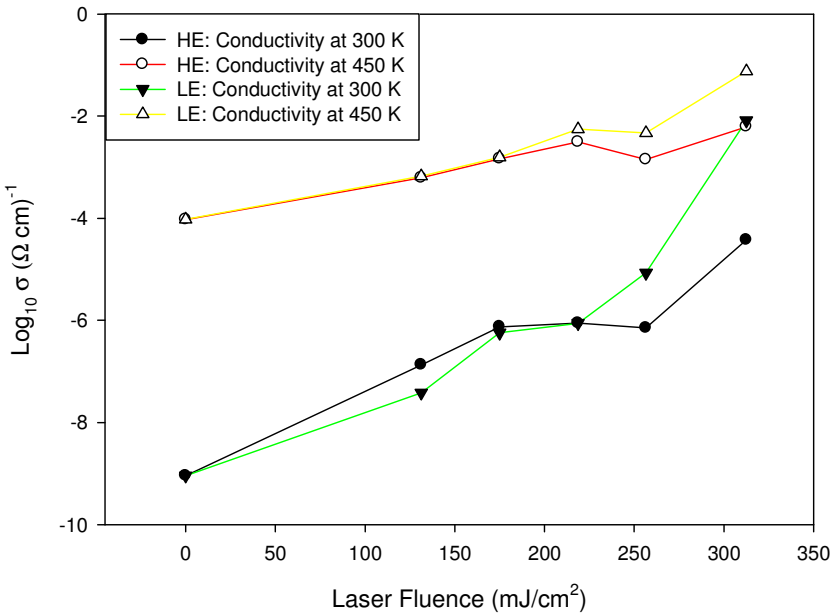

Figure 4.8: Logarithmic plot of conductivity at minimum temperature of 300 K and maximum temperature at 450 K against the applied laser fluence for HE scheme and LE scheme.

Further observation is made by extracting data from the same measurements and these data is organised as in the table 4.1. From this table, the electrical conductivity of the samples as a function of the applied laser fluence is plotted and shown in figure 4.8. From the graph, at 300 K the electrical conductivity for HE scheme samples increase steadily as the value of applied laser fluence increase. Electrical conductivity for LE scheme also has a steady increase for original sample until laser fluence at 218.8 mJ/cm^2. For laser fluence at 256.6 mJ/cm^2 and beyond, the plot shows a rapid increase. At 450 K, electrical conductivity for both samples shows a steady increase from original sample and as the first applied laser fluence applied and increases to the maximum. Both plots have a similar value of electrical

conductivity at low laser fluence until laser fluence reaches 218.7 mJ/cm^2. Beyond this value, the HE scheme tends to reach a steady state while the LE scheme continues to increase steadily. From these results, another apparent observation from the graph is at maximum laser fluence of 312.5 mJ/cm^2, the value of electrical conductivity for HE scheme at 450 K is similar to LE scheme at 300 K.

Another observation between these two schemes is made by plotting the ratio of electrical conductivity at 450 K to 300 K against the applied laser fluence. This will provide the idea of how many times the electrical conductivity is changed, between these two temperatures and its variation towards the increase the laser fluence. The plot is showed in the figure 4.9. For original sample, the ratio is very high, at 150 times. At the lowest laser fluence, the ratio for HE scheme is nearly 40 while the ratio for LE scheme is nearly 70. For the second lowest laser fluence, the ratio for both samples decreases and have similar values of approximately 30. At the highest laser fluence, the ratio for HE scheme is nearly 10 while the ratio for LE scheme is almost 3, which is the smallest ratio of all the samples. The value indicates that, within that temperature range, there is only a small variation of dark conductivity for this particular sample.

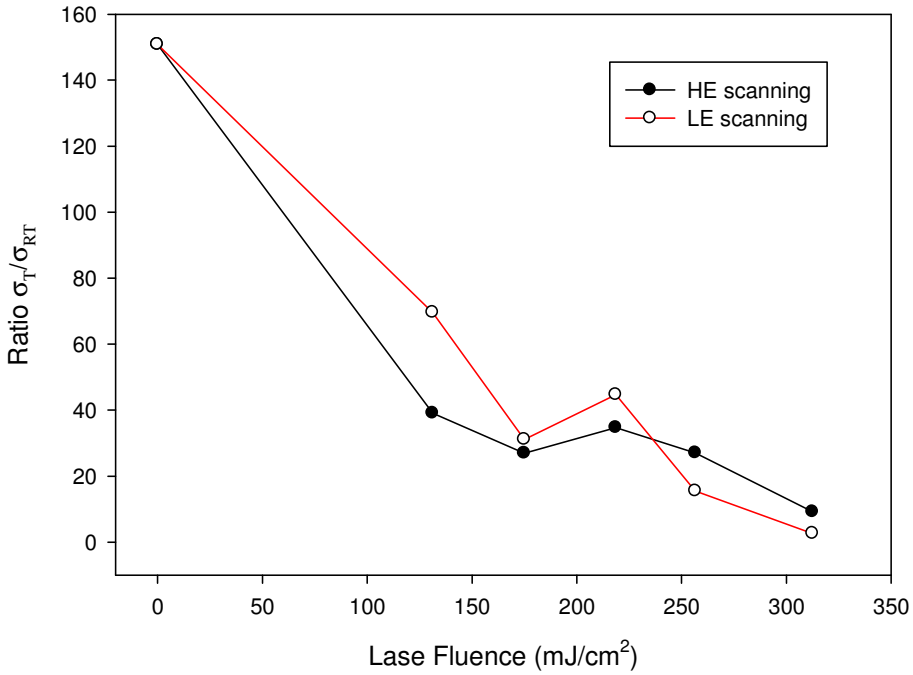

Figure 4.9: Plot for ratio of σ_T/σ_{RT} against the applied laser fluence.

4.3.2 Activation Energy

Other derivations from the conductivity measurement data are the values of activation energy E_a and pre-exponential factor σ_o. A summary of these data is shown in table 4.2. A plot of the activation energy for both schemes against the applied laser fluence is given in figure 4.10. From this plot, variations of activation energy towards different laser fluence can be observed.

Laser Fluence (mJ/cm^2)	0	131.3	175.0	218.8	256.6	312.5
E_a (eV) [HE Scheme]	0.8957	0.6545	0.5879	0.6334	0.5888	0.3955
E_a (eV) [LE Scheme]	0.8957	0.7576	0.6138	0.6785	0.4894	0.1727
σ_o $(\Omega\ cm)^{-1}$ [HE Scheme]	1.49E+06	1.27E+04	5.62E+03	3.88E+04	5550	166
σ_o $(\Omega\ cm)^{-1}$ [LE Scheme]	1.40E+06	1.96E+05	1.23E+04	2.14E+05	1600	6.06

Table 4.2: Values of activation energy E_a and pre-exponential factor σ_o at various laser fluences for HE and LE scheme.

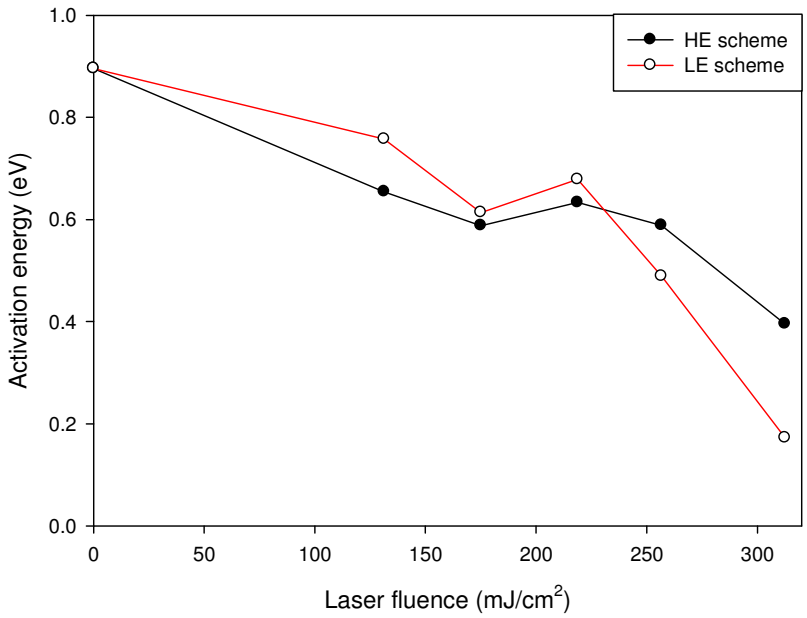

Figure 4.10: Plot for activation energy E_a against the applied laser fluence.

The activation energy of the original sample is the highest compared to the laser processed samples. It has the value of 0.8957 eV. For the laser processed samples, both schemes having the trend of decreasing activation energy with the increase of applied laser fluence. The activation energy for the first three lower laser fluence in LE scheme is bigger than the HE scheme. But after the laser fluence reaches 256.6 mJ/cm^2, the value of activation energy for LE scheme starts to reduce to lower values than with the HE scheme. At the highest laser fluence, the activation energy for the LE scheme is reduced significantly and shows the smallest value. For the HE scheme, it shows a steady decrease of activation energy across the increase in the applied laser fluence. These results suggest that the difference between conduction band and Fermi level is reduced by the applied laser. It is also showed that at high applied laser fluence, the reduction in LE scheme sample is much bigger than in the HE scheme sample.

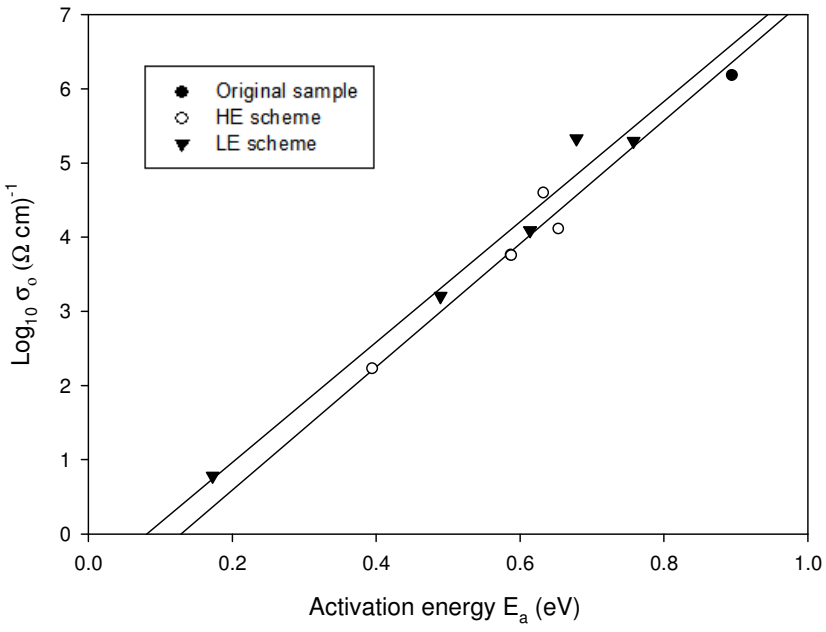

Figure 4.11: Plot for pre-exponential factor σ_o as function of activation energy E_a for various applied laser fluence in HE and LE scheme.

The study of Meyer-Neldel relation for these samples is carried out by plotting the pre-exponential factor against the activation energy. A plot of this relation is shown in figure 4.11. From the plot, a value of the constant σ_{oo} is obtained as 0.0863 and 0.220 Ωcm^{-1} for HE and LE scheme respectively. While the Meyer-Neldel energy E_{MNR} obtained as 120 and 123 meV for HE and LE scheme respectively.

These results showed that the data for both samples fall along the linear line and clearly demonstrates the linear dependencies of activation energy and pre-exponential factor. The laser process samples obey the Meyer-Neldel rule which normally observed in porous and amorphous silicon [84-85] and also microcrystalline silicon [86]. Therefore, it was believed that the samples were not fully crystallised by laser irradiation, instead still inherit hydrogen content with disorder structure from the previous amorphous form. Discussion on hydrogen content in these samples will be showed in next chapter in section 5.3.

4.3.3 Dark Current and Photocurrent

In this section a comparison is made between current generated by unilluminated condition and by light illuminated condition. The dark current I_d reading was taken at 300 K after the samples were annealed as in the previous section. The photocurrent I_p reading was taken by illuminating condition the sample with a 75 W bulb through the glass window. From the results, the differences between dark current and photocurrent was made by comparing the ratio between these two parameters for HE and LE scheme samples. Different values of dark current and photocurrent is summarised as in the table 4.3.

Laser Fluence (mJ/cm^2)	Current [HE Scheme]		Current [LE Scheme]		Ratio I_p/I_d	
	Dark I_d (A)	Photo I_p (A)	Dark I_d (A)	Photo I_p (A)	HE	LE
0	6.95E-11	4.14E-06	6.95E-11	4.14E-06	59600	59600
131.3	1.30E-09	8.34E-07	1.00E-09	1.20E-07	642	120
175.0	1.90E-09	2.9E-07	2.70E-09	1.08E-07	153	4.00
218.8	2.00E-09	7.28E-08	5.00E-09	5.08E-08	36.4	10.2
256.6	6.95E-09	1.23E-08	8.10E-09	1.13E-08	1.77	1.40

Table 4.3: Dark current I_d, photocurrent I_p and their ratio I_p/I_d at various laser fluences for HE and LE samples.

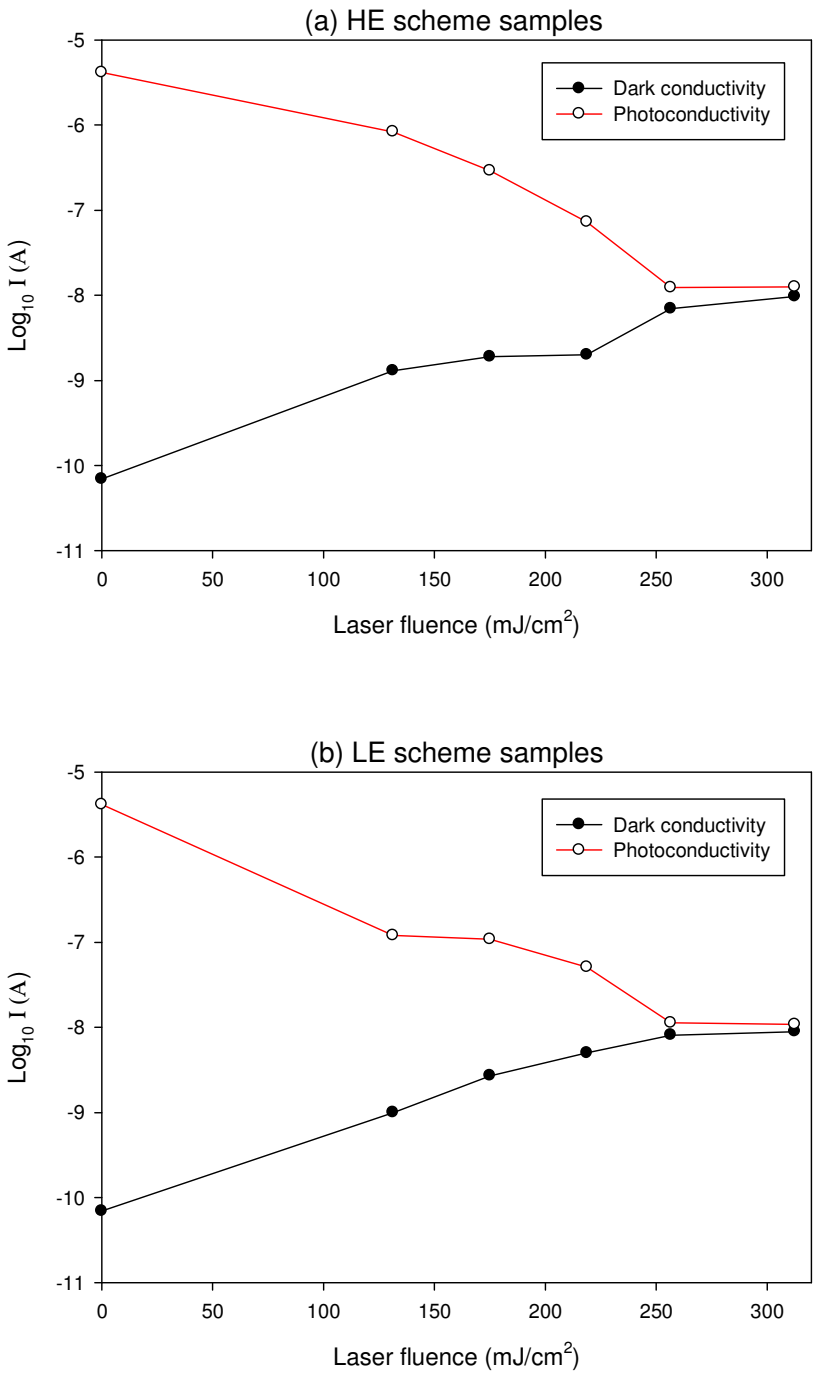

Figure 4.12: Logarithmic plots of dark current I_d, photocurrent I_p against the applied laser fluence for HE scheme (a) and LE scheme (b).

The value of dark current for the original amorphous silicon sample was 6.95 x 10^{-9} while the value of photocurrent was by 4.14 x 10^{-6}. From the table, the values

of these currents are plotted against the applied laser fluences as in figure 4.12 (a) and (b). From the figure, it reveals that the value of dark current for HE scheme samples increases as the applied laser fluence is increases. This is the direct outcome that can be predicted from the previous trend of dark conductivity of this sample. The increase in conductivity is due to the laser processing which crystallised the sample, increases the carrier mobility and consequently increases the generated current. However, the dark current reaches a steady state condition when the laser fluence is increased to a higher value.

Compared to the dark current, the photo generated current shows a decreasing trend with the increase of the applied laser fluence. From the figure it is shown that the plot for photocurrent is steadily decreased for the first four applied laser fluences. At the highest laser fluence, the plot is found to be in a steady state condition. It is very obvious here that the value of dark current and photocurrent are almost the same. It is likely that the number of carriers generated from light illumination is decreased as a result from the increase of crystallisation effect from the laser irradiation. The higher applied fluence reducing the hydrogen content and leading to the formation of microcrystalline silicon with a high concentration of grain boundaries. These grain boundaries which act as defects become recombination centres and reduce the photocarriers.

For the LE scheme sample, the trend is found to be similar. The plot of dark current is very much like the HE scheme samples. However, the plot for photocurrent is slightly lower. As the applied laser fluence increase to maximum, the

plots for both type of current tend to saturate with a similar trend. And at high applied laser fluence, the value of photocurrent is found to be disappeared.

Further analysis is done by plotting the ratio I_p/I_d against the applied laser fluence as in the figure 4.13. From this plot, it is clearly seen that the ratio I_p/I_d for HE scheme samples is bigger than the ratio for the LE scheme. At the lowest applied laser fluence, the given ratios are 642 and 120 for HE and LE sample respectively. Both plots show a steady decrease for the first three lower laser fluence. After the fourth laser fluence, values of these ratios rapidly decrease and is further reduced at the highest laser fluence to 1.77 and 1.4 for HE and LE scheme respectively. For both cases it showed that high laser fluence leading to less photo generated carrier and this is the reason the ratio is almost equal to 1.

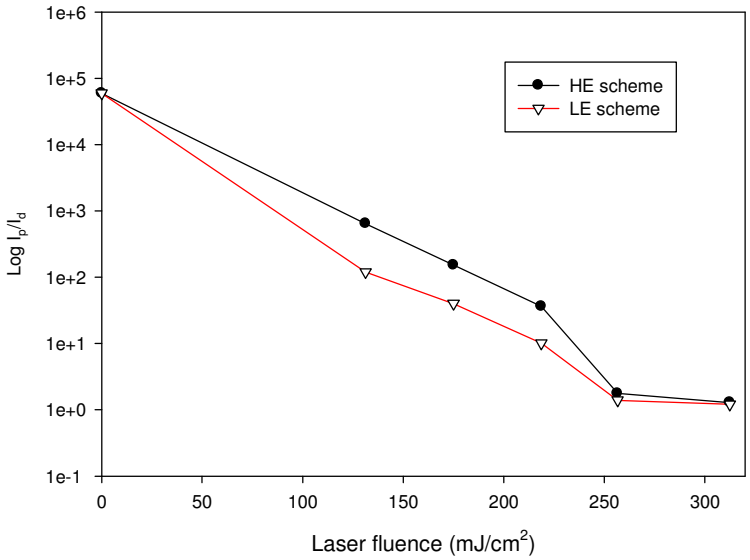

Figure 4.13: Plot of ratio I_p/I_d as a function of the applied laser fluence for HE and LE scheme.

4.3.4 Time-Resolved Terahertz Spectroscopy

Steady state conductivity and photoconductivity has been measured. Transient analysis has been used to append this data. Photoexcitation of carriers can give insight into the structure and electronic material. The dynamics of ultrafast photoconductivity for the laser processed silicon material was measured by colleagues at DTU Fotonik – Technical University of Denmark using the time-resolved terahertz (THz) spectroscopy technique [87]. A 35 ns pulse laser with central wavelength of 800 nm from a Ti:sapphire amplifier was used to generate and detect the THz probe pulse. Results of the photoconductivity dynamics are shown in figure 4.14. From the figure, a near-single photoconductivity exponential decay was observed after an initial fast rise of conductivity after photoexcitation.

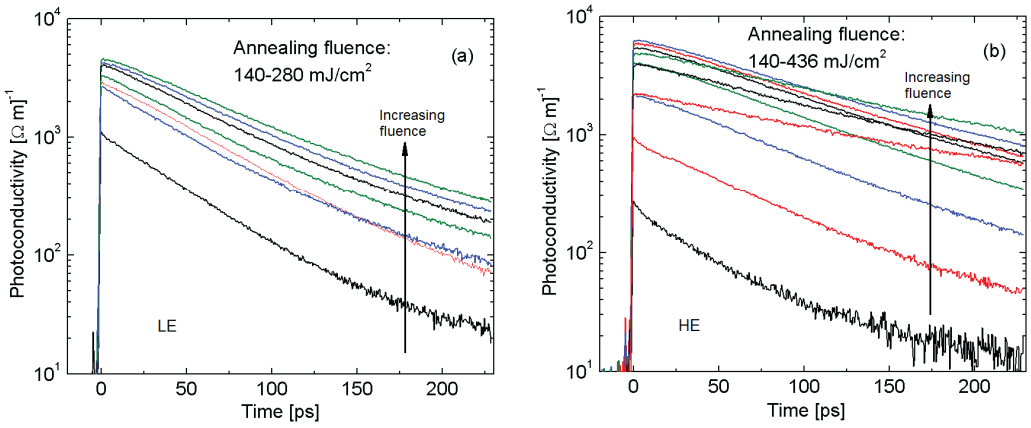

Figure 4.14: Photoconductivity of laser processed amorphous silicon for various laser fluences, (a) between 140-280 mJ/cm^2 using LE scheme and (b) between 140-436 mJ/cm^2 using HE scheme.

The peak conductivity has been extracted from figure 4.14 and plotted against applied laser fluence for both the HE and LE regimes and is shown in figure 4.15 (a). From the results, the highest photo-induced conductivity was demonstrated at a laser fluence of 215 mJ/cm^2 for the LE sample and at 280 mJ/cm^2 for HE sample. Then, conductivity decay curves were fitted with a single exponential decay to extract a decay time and this is plotted in figure 4.15 (b). The slowest decay time was observed for the LE sample at laser fluence of 233 mJ/cm^2 where the largest photo-conductivity was also observed. For the HE samples, it showed that the decay time was increased with the increase in applied laser fluence.

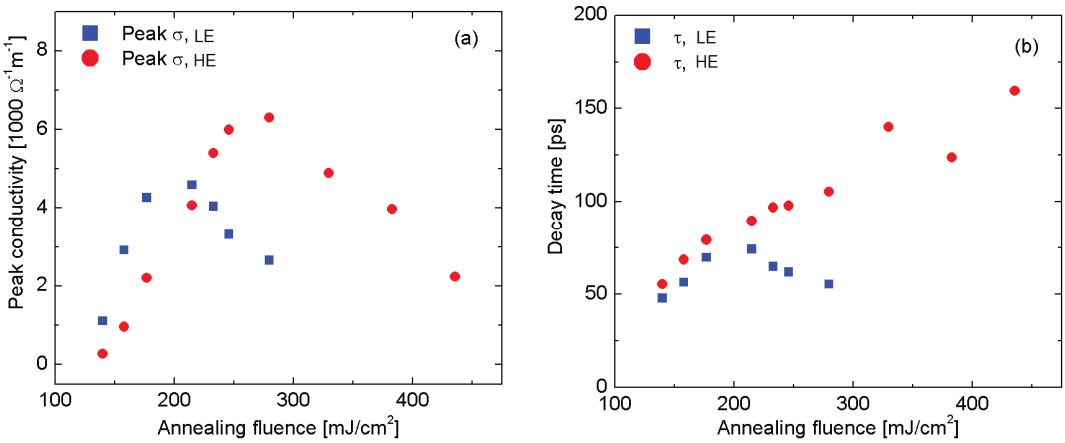

Figure 4.15: (a) Peak conductivity from figure 4.13 as a function of the applied laser fluence for the two different schemes. (b) Decay time of the photoconductivity as a function of laser fluence for the two different schemes.

From this measurement technique, it showed that amplitude and decay time of the photoinduced conductivity of laser processed amorphous silicon were dependent strongly on the applied laser fluence and type of scanning scheme. This will be related to the other measurement methods, such as the field emission and Raman spectroscopy that follows, that we have employed to probe the material this and contributes to a picture of highly conducting crystalline nanoscale features in a composite that allows such a photoconductive response.

4.4 Results and Discussion on Field Emission Measurements

In this section, electron field emission results from samples processed with the HE scheme, LE scheme, and laser processed in vacuum are presented. The Samples were 300 nm amorphous silicon on 200 nm Mo coated corning glass. The results give insights into the emission properties of these samples and their internal structures and provide a comparison with previous work. A fixed gap sandwich structure was used to measure the emission current, and the size of the gap between the sample and anode was measured to be 170 μm.

4.4.1 Field Emission Profile for HE Scheme

In this first section, the field emission results from the HE scheme samples are presented. There are five different laser fluences used, which are 131.3, 175.0, 218.8, 256.6, and 312.5 mJ/cm^2. The threshold field is defined when the minimum applied field yields an output current of 1 nA. There are four steps of measurement done for each sample, giving two full cycle of increasing and decreasing voltage. Figure 4.16 (a) to (e) shows *I* versus *E* plots for each samples.

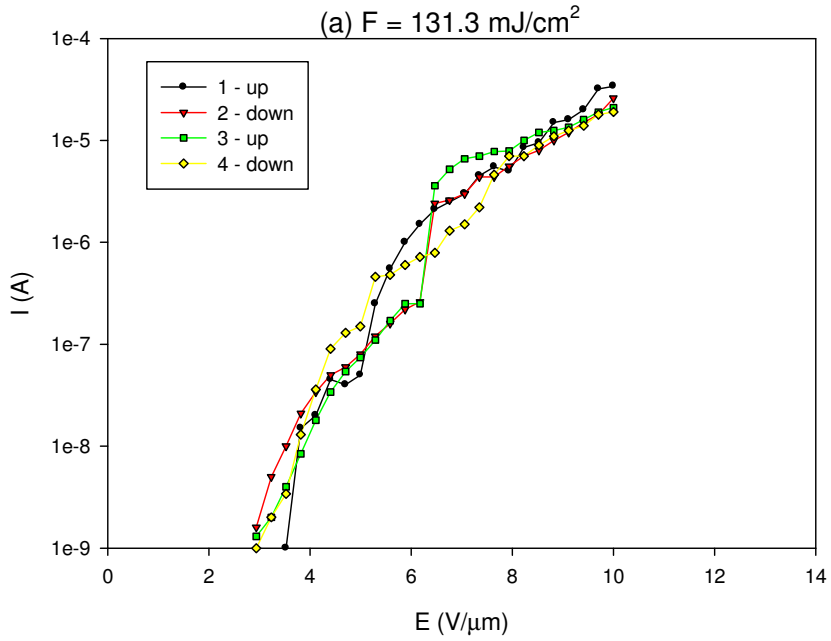
(a) F = 131.3 mJ/cm2
1 - up
2 - down
3 - up
4 - down
I (A)
1e-4
1e-5
1e-6
1e-7
1e-8
1e-9
0
2
4
6
8
10
12
14
E (V/µm)

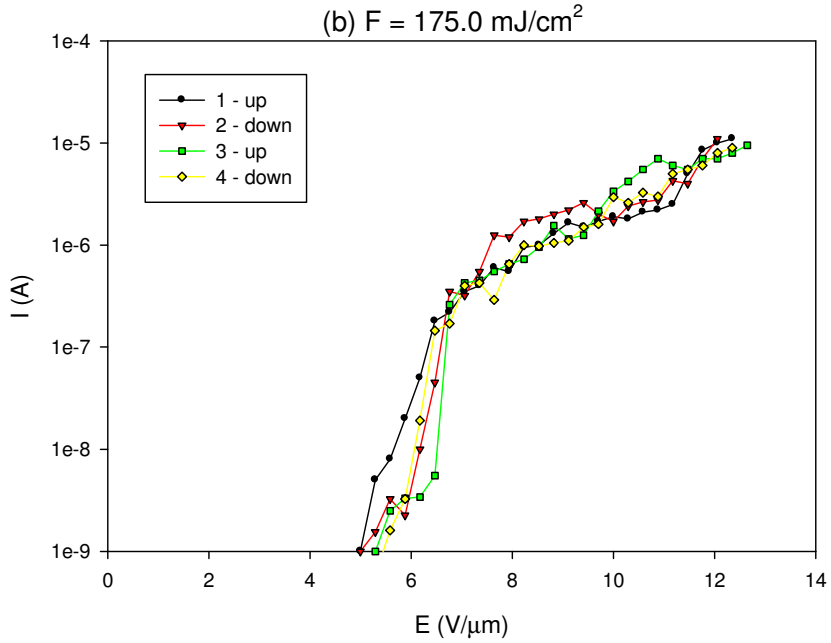
(b) F = 175.0 mJ/cm2
1 - up
2 - down
3 - up
4 - down
I (A)
1e-4
1e-5
1e-6
1e-7
1e-8
1e-9
0
2
4
6
8
10
12
14
E (V/µm)

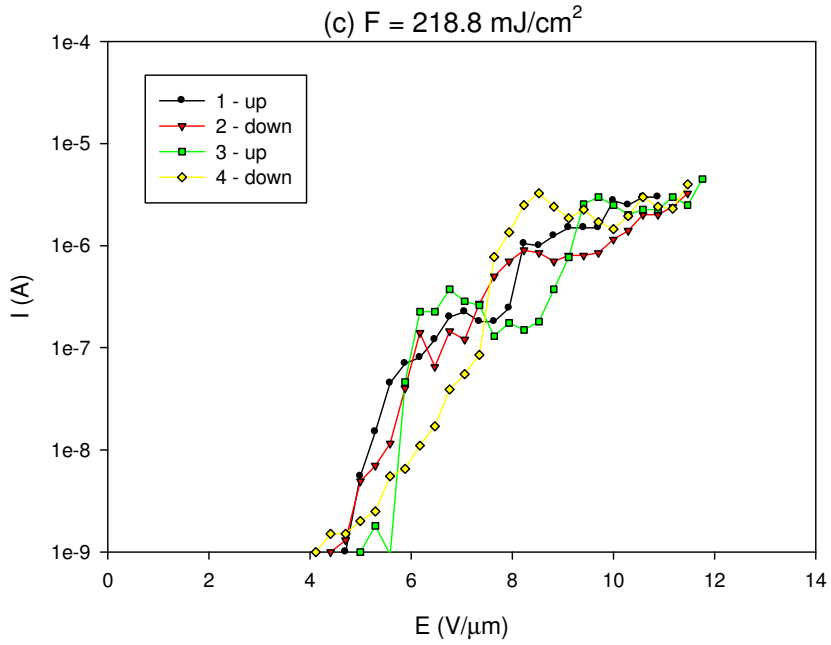
(c) F = 218.8 mJ/cm2
1 - up
2 - down
3 - up
4 - down
I (A)
E (V/µm)
1e-4
1e-5
1e-6
1e-7
1e-8
1e-9
0
2
4
6
8
10
12
14

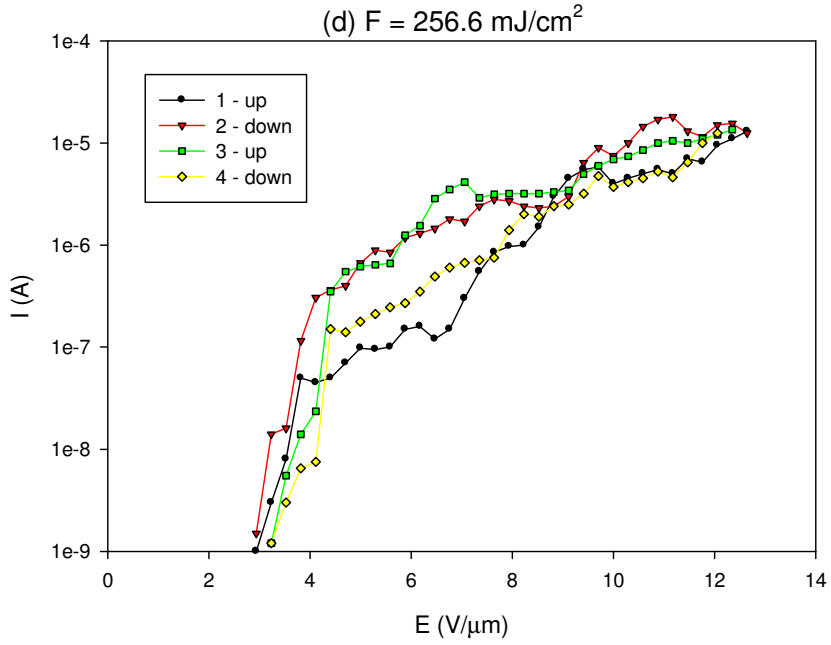
(d) F = 256.6 mJ/cm2
1 - up
2 - down
3 - up
4 - down
I (A)
E (V/µm)
1e-4
1e-5
1e-6
1e-7
1e-8
1e-9
0
2
4
6
8
10
12
14

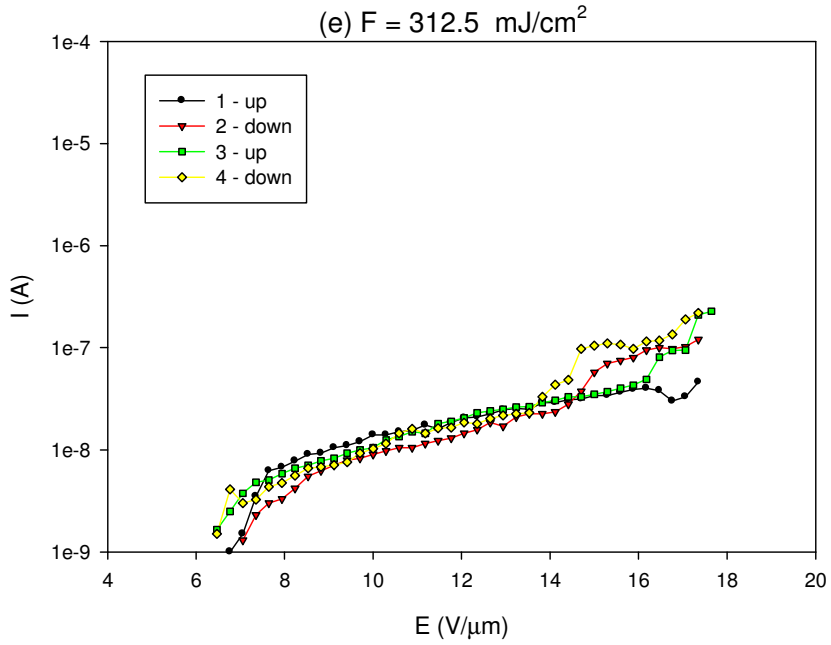

Figure 4.16 (a) to (e): Plots of emission current I against the applied field E for HE scheme samples at applied fluences ranging from 131.3 to 312.5 mJ/cm^2.

Carbon nanotube (CNT) was regarded as the best sample and could produced electron emission at low threshold as low as 1 to 3 V/µm with current density's as high as 1 mA/cm^2 [88]. However, typical threshold for laser process amorphous silicon was around 15 V/µm [65]. For analysis in this section, a logarithmic scale for the current axis is used because the resulting currents increased exponentially with the applied field. The field emission results reveal good electron emission from the samples. For the sample at the lowest laser fluence of 131.3 mJ/cm^2, the threshold field E_{th} is 3.5 V/µm. The emission current was steadily increased until it reached a maximum value of 3.4 x 10^{-5} A at the macroscopic field of 10 V/µm. The results was quite surprising since from the SEM analysis in the previous section of 3.3.4, it was

reveal that there were no sharp spike formed that might contribute to the enhancement factor.

For laser fluence 175.0 mJ/cm^2, the emission was achieved at macroscopic field of 5 V/μm. The maximum current was achieved at 1 x 10^{-5} A at macroscopic field of 12 V/μm. Although from the SEM analysis the microscopic spike was formed, the E_{th} value was found to be slightly bigger than the first sample without microscopic protrusions. The third sample at a laser fluence of 218.8 mJ/cm^2 showed sharper and bigger surface microstructure features and give emission with E_{th} of 4.7 V/μm. The maximum emission current was achieved at 3 x 10^{-6} A at macroscopic field of nearly 11 V/μm.

For the fourth sample at 256.6 mJ/cm^2, the E_{th} was achieved at nearly 3 V/μm which is the lowest among all the samples. The microstructure of this sample also has the highest microstructure compared to the others. Maximum current was achieved at 1.3 x 10^{-5} A at a microscopic field of 12.6 V/μm. For the highest applied laser sample at 312.5 mJ/cm^2, the E_{th} was achieved at 6.8 V/μm. The maximum current was achieved at 2.3 x 10^{-7} A for a microscopic field of 17.6 V/μm. The value of is E_{th} for this sample is the highest among other samples. It showed here that minimum current is achieved at the highest applied external field. Although the external of microstructure features for this sample is quite similar to the sample at 256.6 mJ/cm^2, it showed that the emission property is different.

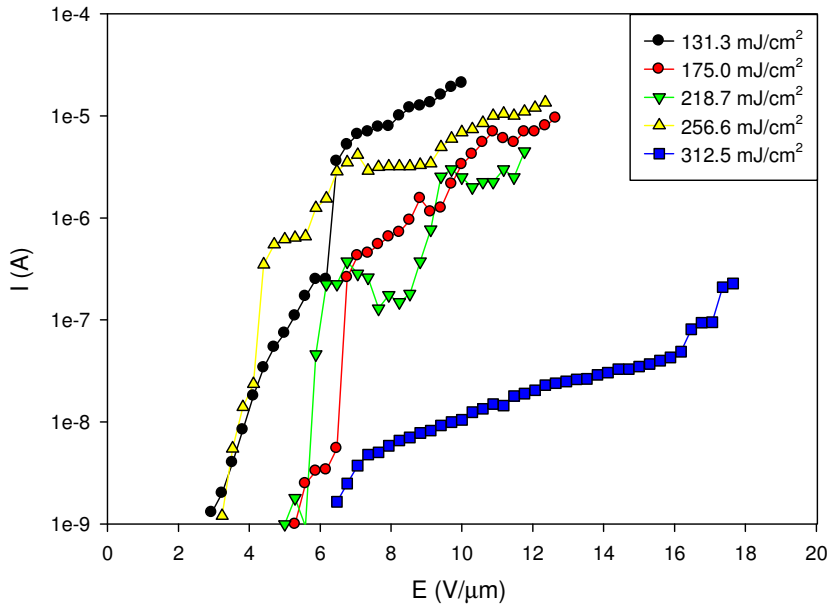

Figure 4.17: Combination plots of the third emission current I measurement against the applied field E for HE scheme samples at applied laser fluences ranging from 131.3 to 312.5 mJ/cm^2.

For comparison between the different laser fluences and the emission results, the third emission measurement of each plot is combined together in a single graph of figure 4.17. From the plot, we see that for the HE scheme samples, the lowest value of E_{th} was achieved from the sample at the lowest fluence. The maximum current also was achieved by this sample at fairly low macroscopic field. For the sample with the highest applied laser fluence, the value of E_{th} was the highest and also the maximum emission current as well. Despite the fact that the first four lower laser fluences had lower E_{th}, there are inconsistencies in the plot of the resulting emission current when the macroscopic field is increased. The steady increase in emission current was only found for samples at the highest applied laser fluence.

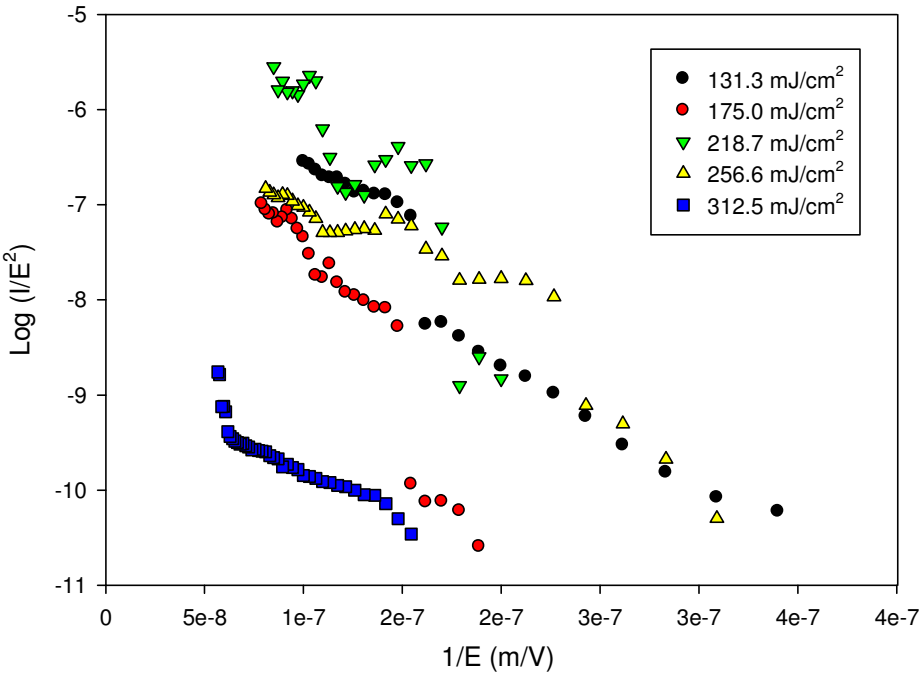

Figure 4.18: Corresponding F-N plot for the I-E graph in the figure 4.17.

From the F-N plot in the figure 4.18, it is revealed that only the sample for applied laser fluence 312.5 mJ/cm^2 shows a clear linear characteristic on a log plot. Other samples such as applied laser fluence 131.3, 175.0 and 256.6 mJ/cm^2 had a linear characteristic only at a certain range. The sample for intermediate applied laser fluence does not show a linear relation of the F-N plot. These results suggested that the F-N model alone is not sufficient to explain the emission from this type of sample.

4.4.2 Field Emission Profile for the LE Scheme

An investigation of the field emission for samples in the LE scheme was carried out to compare with the results produced by the HE scheme. From the surface morphology study in section 3.3.3, the LE scheme gives blunt microstructures (as opposed to the sharp spiky feature in HE scheme). The field emission resulting from this feature will be presented in this section. Similar laser fluence was used to produce five different samples as in the previous section. The I-E plots for these samples are shown in figure 4.19 below.

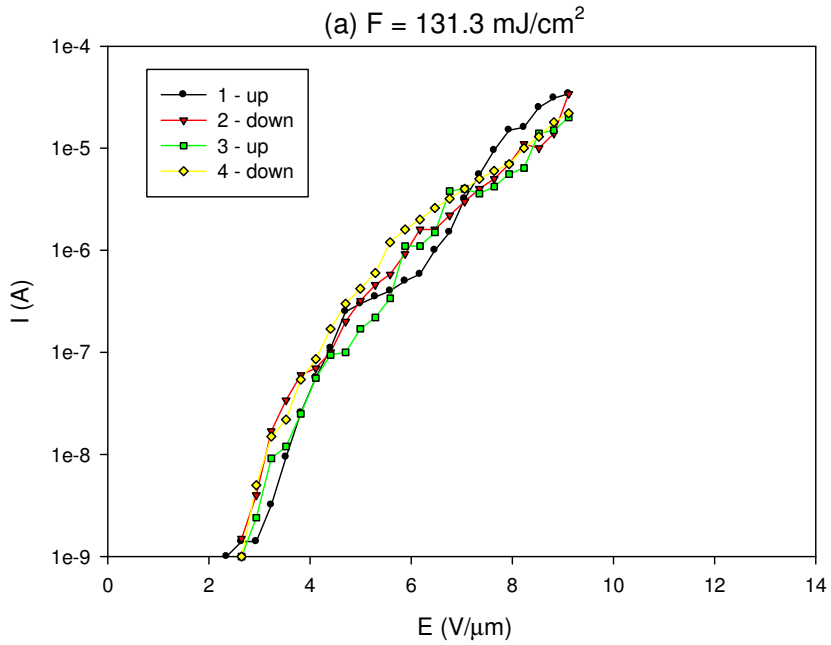

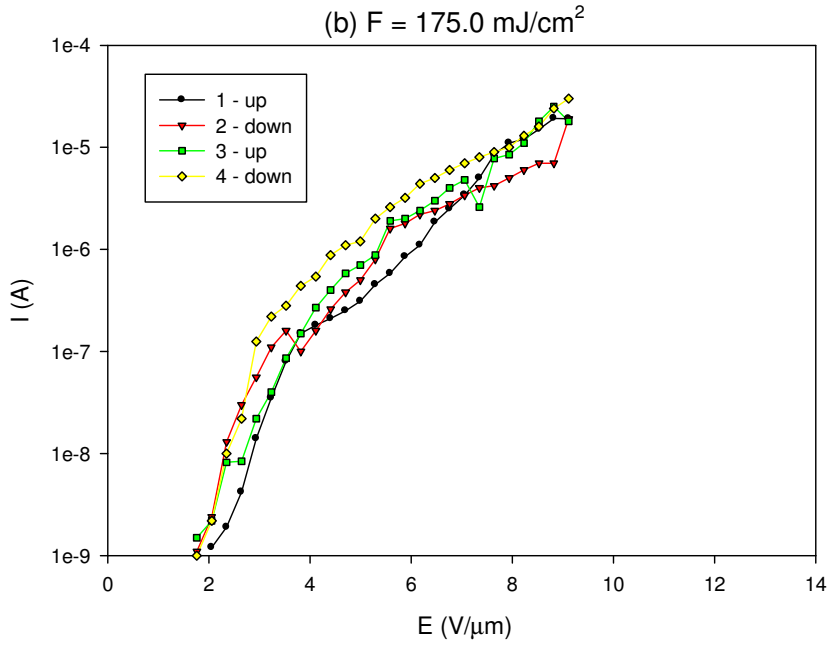
(b) F = 175.0 mJ/cm2
1 - up
2 - down
3 - up
4 - down
I (A)
E (V/µm)
1e-4
1e-5
1e-6
1e-7
1e-8
1e-9
0
2
4
6
8
10
12
14

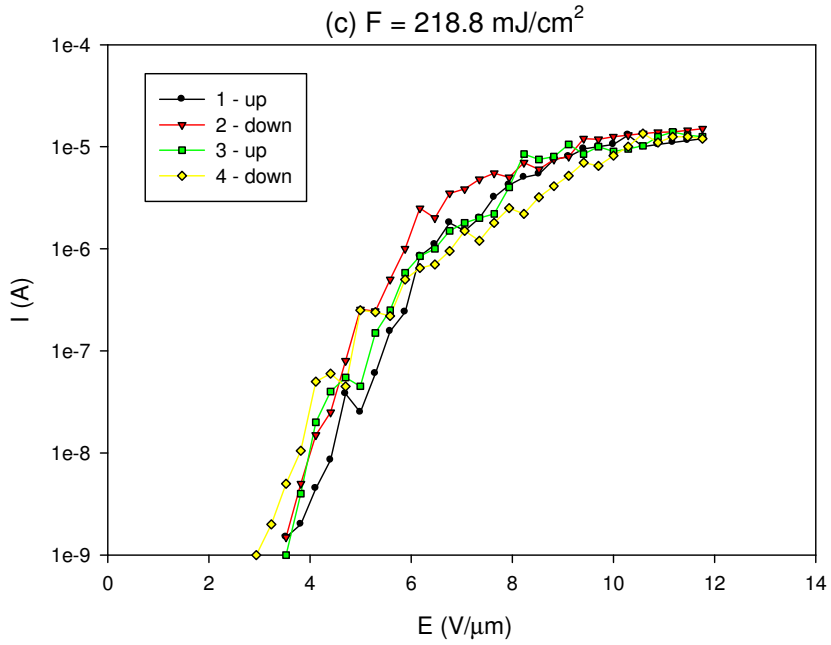
(c) F = 218.8 mJ/cm2
1 - up
2 - down
3 - up
4 - down
I (A)
E (V/µm)
1e-4
1e-5
1e-6
1e-7
1e-8
1e-9
0
2
4
6
8
10
12
14

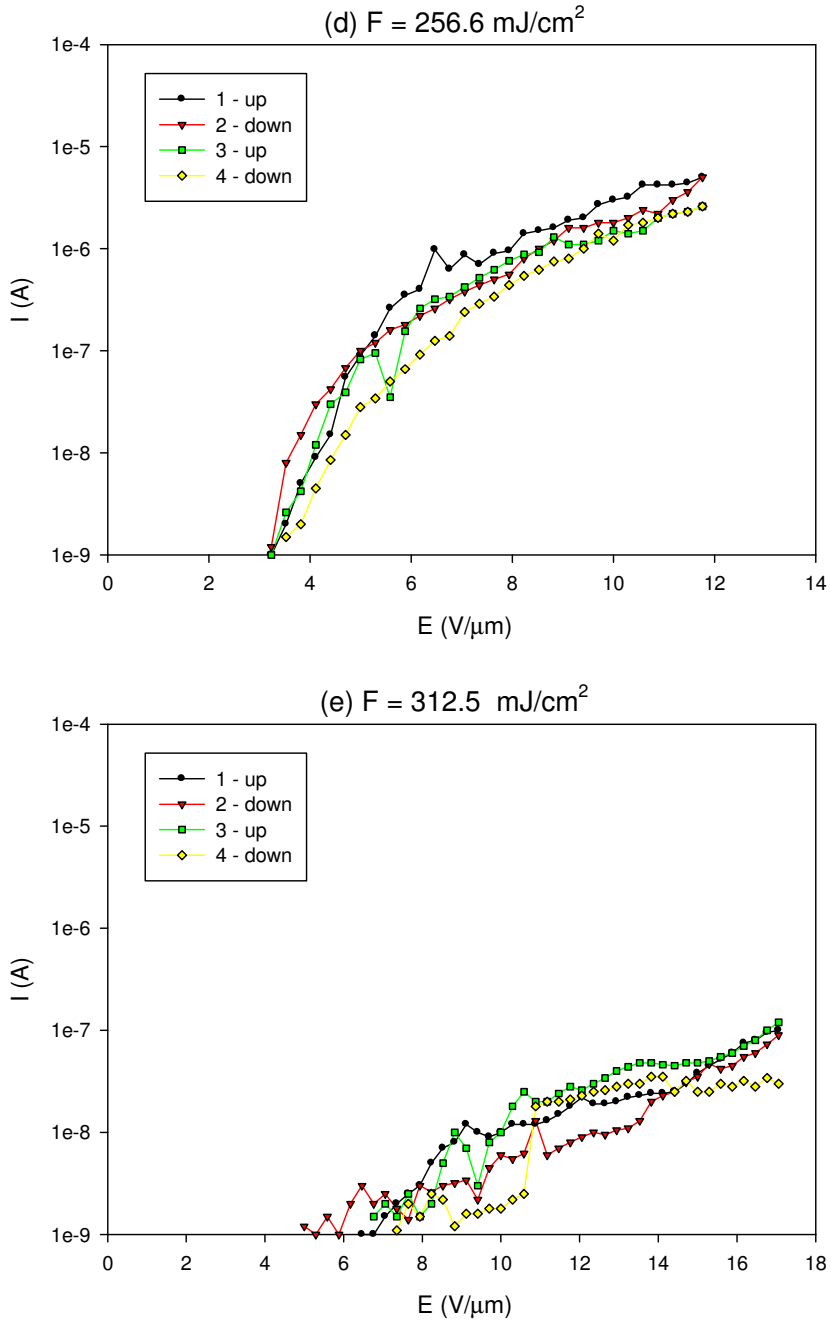

Figure 4.19(a) to (e): Plots of emission current I against the applied field E for LE scheme samples at applied fluences ranging from 131.3 to 312.5 mJ/cm^2.

The field emission results for the LE scheme samples reveal a slightly different I-E plot compared to the HE scheme. Sample at the lowest applied laser

fluence at 131.3 mJ/cm^2 has a low E_{th} and produced a good I-E plot for each measurement cycle process. Although this sample does not feature protrusion or microstructures, it manages to produce a minimum current of 1 nA at E_{th} of 2.4 V/μm. The emission current was steadily increased until it reached the maximum value of 3.4 x 10^{-5} A at the macroscopic field of 9.1 V/μm. This is further proof that electron emission is not a geometric field enhancement such as found in the Spindt tip type.

For the second sample, the minimum current emission was achieved with E_{th} of 2 V/μm, the lowest among all samples. This sample also shows a steady increase in current emission during all measurements. The maximum current achieved for this sample was 1.9 x 10^{-5} A at the macroscopic field of 9.1 V/μm. This sample is the first to feature microscopic structure and it from a slightly lower E_{th}.

The third sample had E_{th} of 3.5 V/μm and the achieved maximum current was 1.2 x 10^{-5} A at macroscopic field of 11.7 V/μm. The size of microstructure for this sample was bigger than the second sample. However, it is shown here that this sample requires a bigger macroscopic field. For the fourth sample, the E_{th} value was 3.2 V/μm, very close to that of the third sample. The achieved maximum current was 5 x 10^{-6} A at a macroscopic field of 11.7 V/μm.

For the last sample, the minimum current was achieved at a higher E_{th} of 6.5 V/μm. This sample only achieved maximum current of 1 x 10^{-7} A at a macroscopic field of 17.0 V/μm. Compared to other sample in the LE scheme, the electron emission was not steady and consistent. This outcome was also different from the

results produced by the HE scheme sample although the limitation in emission current was similar.

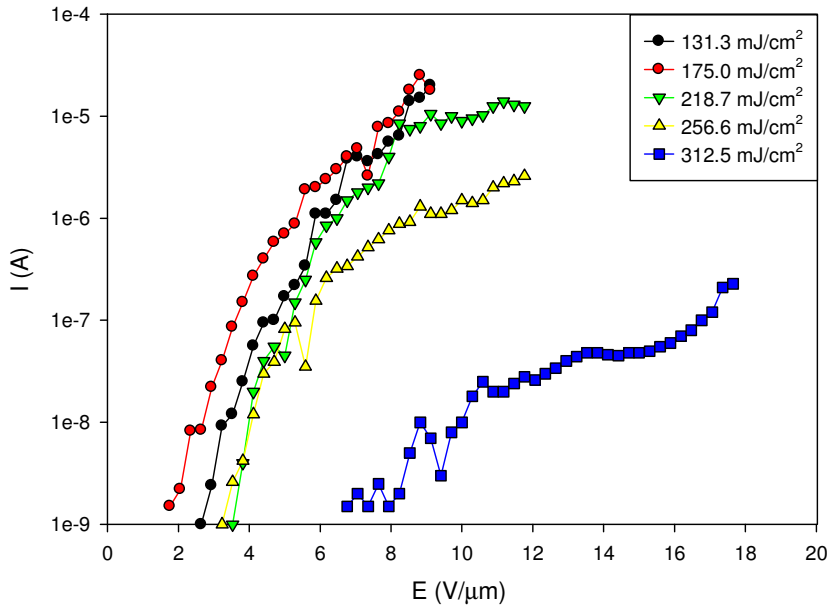

Figure 4.20: Combination plots of the third emission current I measurement against the applied field E for LE scheme samples at applied laser fluences ranging from 131.3 to 312.5 mJ/cm^2.

A similar comparison plot at different applied laser fluence as in the HE scheme is shown in figure 4.20. From the figure, it is found that the LE scheme samples produced a better and consistent electron emission than in the HE scheme, except for the sample at the applied laser fluence of 312.5 mJ/cm^2. The sample at 175 mJ/cm^2 achieved the lowest E_{th} as well as yields the highest emission current at low macroscopic field. Another interesting result was all the samples, except the

highest one, showed similar feature and range of I-E plot which is totally different from the results featured by the HE scheme samples.

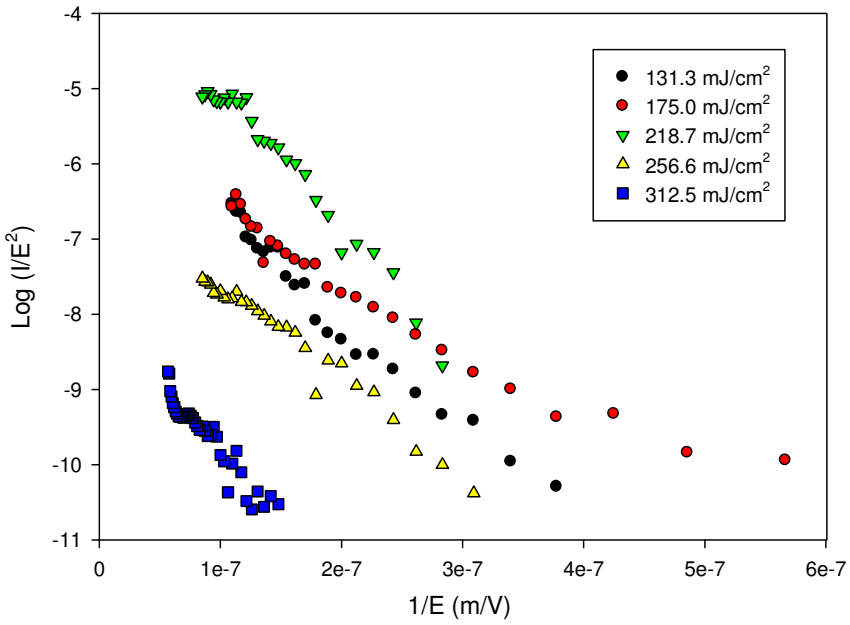

Figure 4.21: Corresponding F-N plot for the I-E graph in the figure 4.20.

The combination of F-N plots for these samples is shown in figure 4.21. From the plot, it reveals that most of the samples demonstrate a nearly linear relation of log I/E^2 against 1/E. A linear fitting line was expected for all plots except at the applied laser fluence of 218.7 mJ/cm^2. Although this LE scheme sample has blunt microstructures, it has the tendency to agree with the F-N theory even though not in terms of geometric field enhancement. Therefore it is believed that the field enhancement was also contributed by other factors such as ENH.

4.4.3 Field Emission Profile for Laser Process in Vacuum

In this section, another type of sample is used to study the emission properties of laser processed amorphous silicon. For the third sample, the irradiation was carried out in a vacuum environment as opposed to the previous HE and LE scheme samples which were irradiated in air. The irradiated sample in vacuum does not have microstructure feature to contribute as geometric enhancement factor. The results from this section will be compared to the previous samples with microstructure features and will provide information on whether the emission produced by the sample is better than the previous samples or vice versa.

A similar setup was used and four different laser fluences applied to the amorphous silicon film at 131.3, 175.0, 218.8 and 256.6 mJ/cm^2. The field emission tests were carried out and the results plotted in figure 4.22.

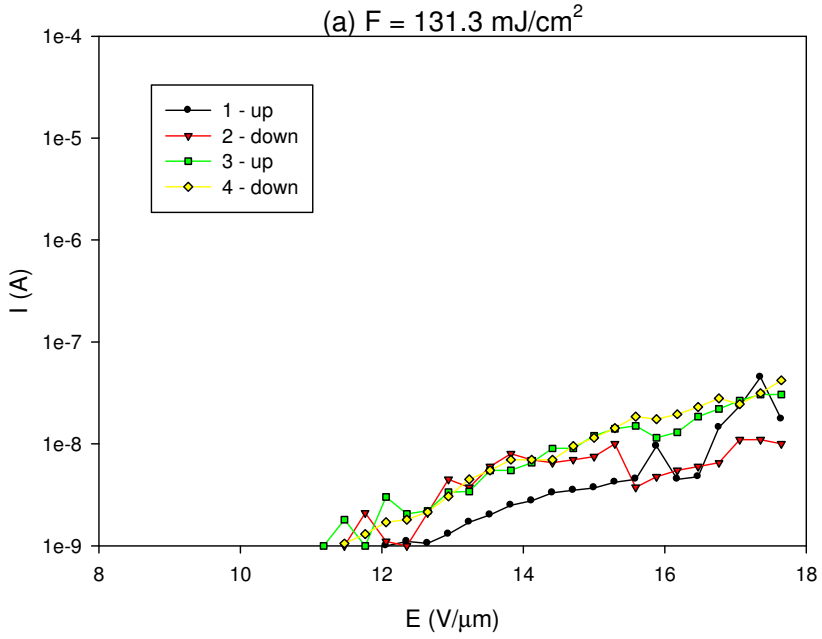

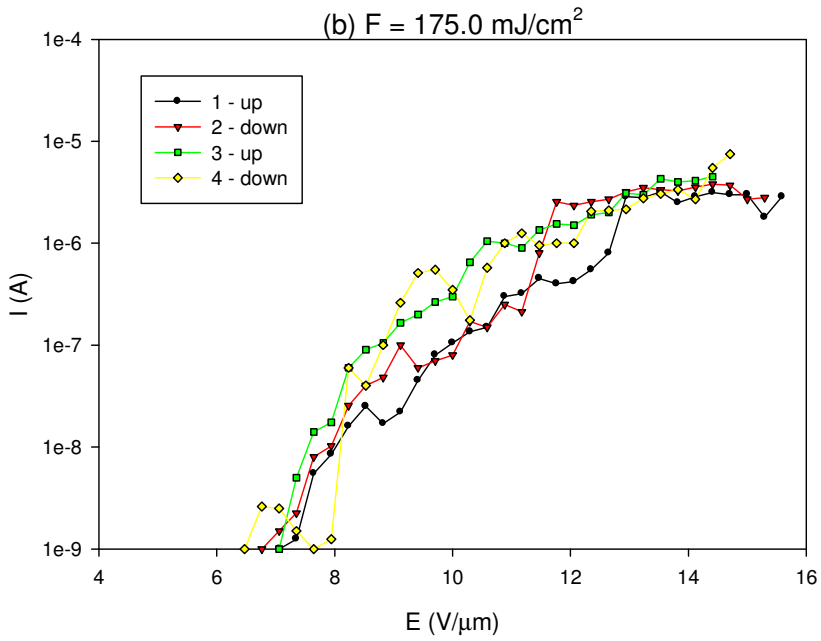
(b) F = 175.0 mJ/cm2
1e-4
1e-5
1e-6
1e-7
1e-8
1e-9
I (A)
1 - up
2 - down
3 - up
4 - down
4
6
8
10
12
14
16
E (V/µm)

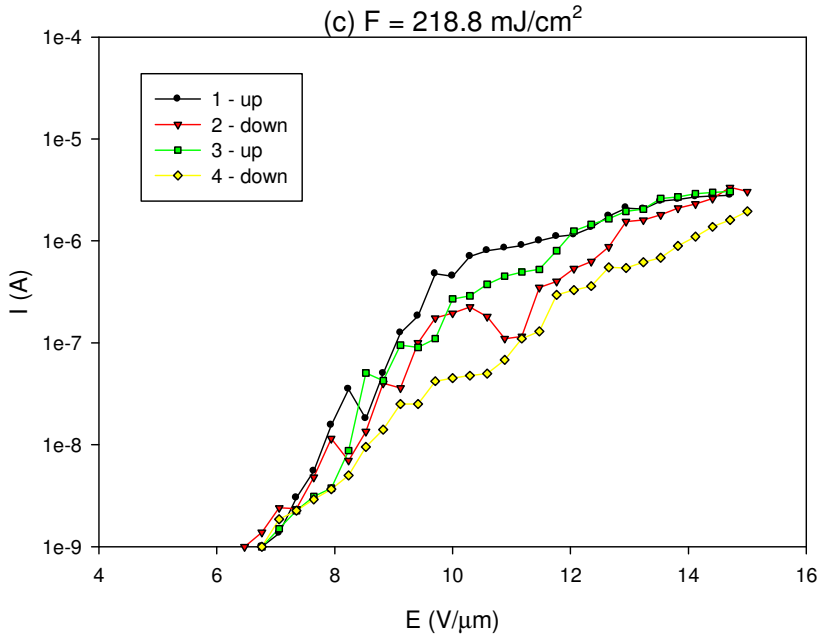
(c) F = 218.8 mJ/cm2
1e-4
1e-5
1e-6
1e-7
1e-8
1e-9
I (A)
1 - up
2 - down
3 - up
4 - down
4
6
8
10
12
14
16
E (V/µm)

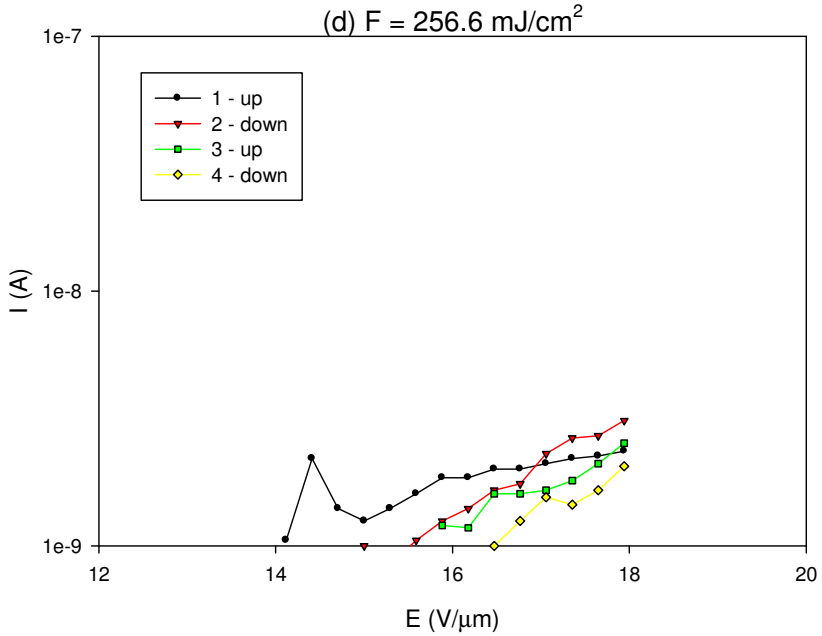

Figure 4.22(a) to (d): Plots of emission current I against the applied field E for sample irradiated in vacuum at laser applied fluences ranging from 131.3 to 256.6 mJ/cm^2.

From the I-E plot, it was verified that the emission was achieved with this type of sample. At the lowest laser fluence, the minimum current of 1 nA was achieved at E_{th} of 12.1 V/µm. The graph however also showed that the emission current varied for different measurements suggesting instability. The maximum current of 4.5 x 10^{-8} A was achieved at macroscopic field of 17.4 V/µm. From the SEM analysis in section 3.3.5, at this fluence, the samples show minimal surface modification compared to other fluences.

For the second sample at applied laser fluence of 175.0 mJ/cm^2, minimum emission current was achieved at E_{th} of 7 V/µm. The maximum current of 3.2 x 10^{-8} A was achieved at macroscopic field of 13.5 V/µm. The previous SEM analysis

reveals that this sample has surface modification with rough features. The crystallisation process was believed to be involved to provide good emission results, although the emission was found to be not stable for all measurement cycle.

The third sample at an applied laser fluence of 218.8 mJ/cm^2 also shows good emission. The minimum emission current was achieved at E_{th} of 6.8 V/μm. This value is the lowest E_{th} among this type of sample. The maximum current of 2.8 x 10^{-6} A was achieved at a macroscopic field of 14.7 V/μm. The surface for this sample has rougher surface features than the second sample. Sub micron protrusions and valleys are also present although not in the same scale as the sample processed in air. However the emission current was also not stable for all measurement cycle.

The last sample at an applied laser fluence of 256.6 mJ/cm^2 produced emission current at E_{th} of 14.7 V/μm. The maximum current of 2.8 x 10^{-9} A was achieved at macroscopic field of 18 V/μm. It was also shown that the emission current was not stable and varied for different cycle measurements. Although the sample morphology was similar with the third sample, it was believed that higher E_{th} was due to the difference in the internal structure and electronic properties within the material.

The combination plot from of the third measurement is shown in figure 4.23. It shows that this type of sample also produces field emission current although at higher E_{th} than the samples processed in air. Good I-E plots were produced by samples in the intermediate applied laser fluence. However the emission for all samples was not stable to compare with the results in the previous sample.

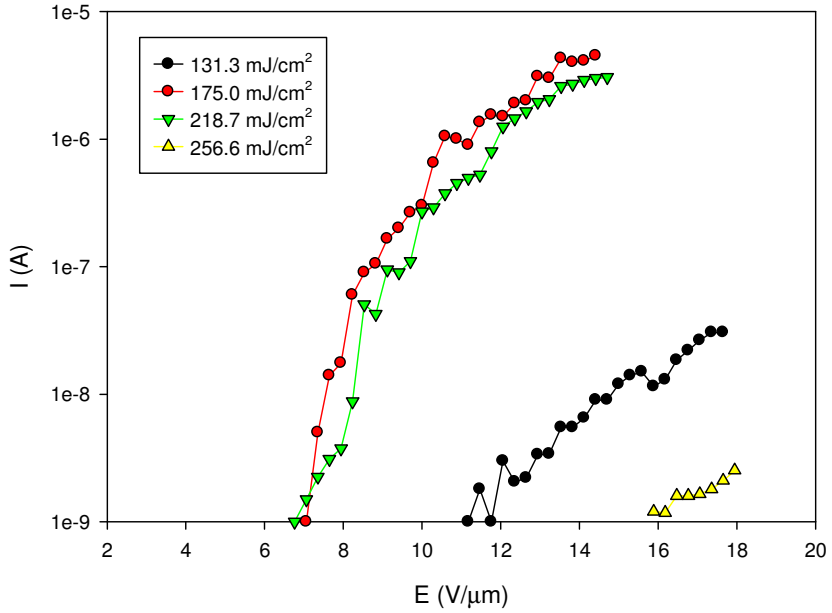

Figure 4.23: Combination plots of the third emission current I measurement against the applied field E for LE scheme samples at applied laser fluences ranging from 131.3 to 312.5 mJ/cm^2.

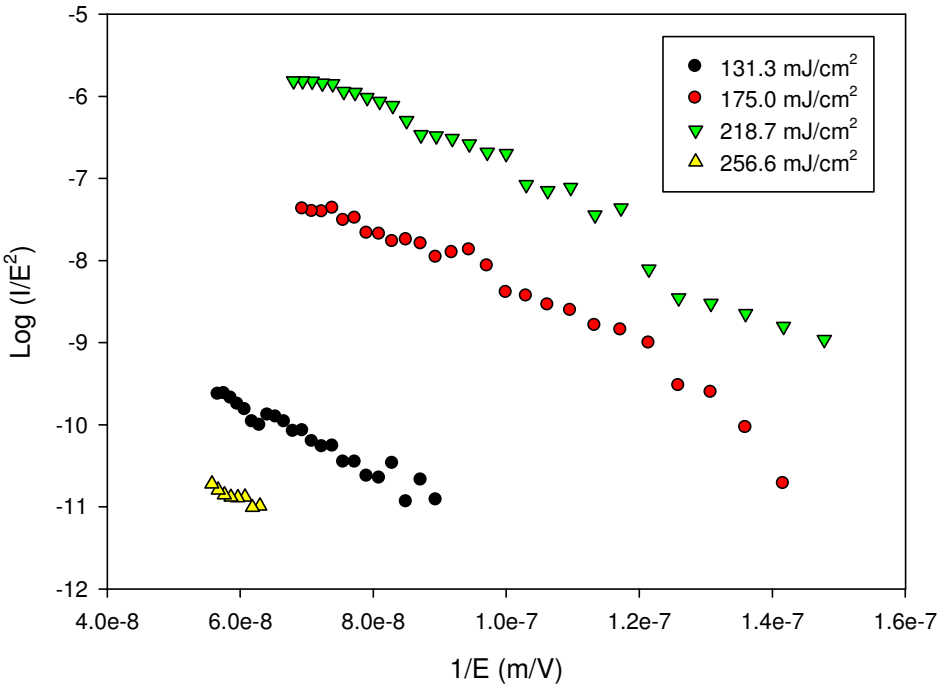

Figure 4.24: Corresponding F-N plot for the I-E graph in the figure 4.23.

The combination of F-N plots for this sample is shown in figure 4.24. From the plot this sample demonstrates almost linear behaviour of log I/E^2 against 1/E for all applied laser fluence. F-N model can be used to explain the field emission although some modification is required to satisfy certain issues which were similar to the case of samples irradiated in air.

4.5 Chapter Summary

In this chapter, dc dark conductivity test and field emission test has been carried out. In the conductivity test, a decreasing in Arrhenius plots has been observed with the increase of the applied laser fluence, which directly translated as the decrease in activation energy. The decrease was believed due to the increase in the crystallisation effect. The Meyer-Neldel rule was also obeyed by HE and LE samples suggested that the samples were not fully crystallised. In the field emission test, low threshold as 3 V/μm and 2 V/μm has been achieved for HE and LE samples respectively. Analysis from the plot suggested that F-N theory was not sufficient to explain the emission properties and enhancement factors. This is because the electron emission has been observed in sample without sharp geometry, which is contradicted to the F-N theory.

Chapter 5 Optical Properties

5.1 Introduction

The surface morphology of laser processed amorphous silicon has a strong effect on the optical properties. Any change in hydrogen contents leads to different profile in IR absorption spectra. FTIR measurements were carried out to analyse the effect of laser fluence on hydrogen content. UV-Vis spectroscopy measurements were used to analyse the properties in light transmission and absorption. Finally, simulation models were developed and used to study the effects on light localisation in ordered and disordered photonic crystals structures to see if the external and internal structural changes might be exploited as a metamaterial.

5.1.1 Hydrogen Content

In hydrogenated amorphous silicon, the typical hydrogen content ranges from 4 at. % to 40 at. % [89]. The role of hydrogen is to lower the defect density by passivating the dangling bonds which have a density of around $10^{15} – 10^{16}$ cm^{-3} [90]. The presence of hydrogen is important, especially in terms of opto-electronic properties where the dangling bonds are the efficient recombination centre for electrons and holes. The optical absorption profile of hydrogenated amorphous silicon is showed in figure 5.1. It shows that the absorption coefficient in the UV region is the highest.

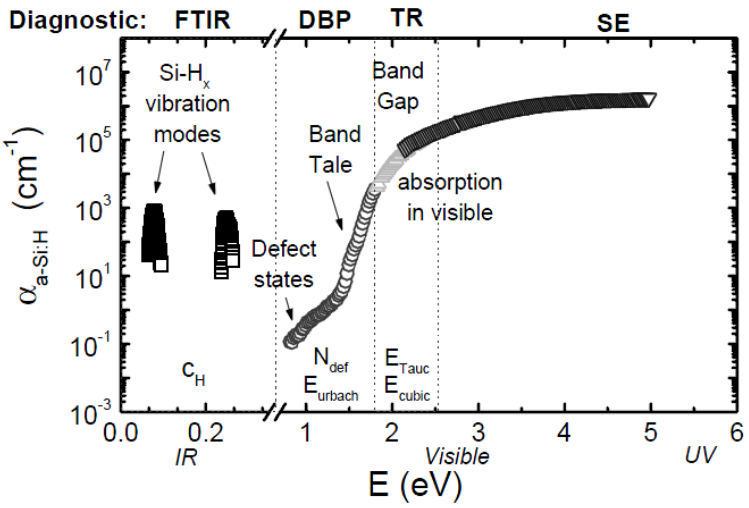

Figure 5.7: Plot of optical absorption coefficient against photon energy for hydrogenated amorphous silicon, measured by various techniques [89].

Another well known property is the Staebler-Wronski effect (SWE) [91] which is the creation of metastable defects in the film when it is illuminated. Usually this defect is reduced by annealing the film up to around 200^{o}C. Several models have been proposed to elucidate the metastable SWE [91-93], however none of them was accepted as a definite mechanism. The presence of hydrogen and its role in the amorphous silicon network is usually considered as the main factor [93].

Hydrogen is incorporated into the amorphous silicon structure and forms Si-H_x hydride bonding. In the IR region, there are three absorption characteristics which are simplified as in table 5.1. The vibration at 840 – 890 cm^{-1} was assigned to the Si-H_2 bonding (dihydride) and both of the stretching modes was assigned to all type of hydride (monohydrides, dihydrides and trihydrides). The stretching modes were categorised into two types, low stretching mode (LSM) for 1980 – 2030 cm^{-1} and high stretching mode (HSM) for 2060 – 2160 cm^{-1}.

Vibration modes	Graphical representation	Wavenumbers
Wagging	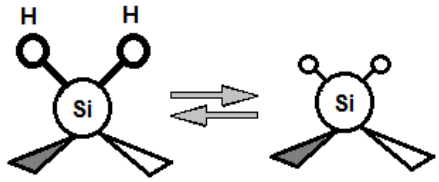	640 cm^{-1}
Bending or scissor doublet	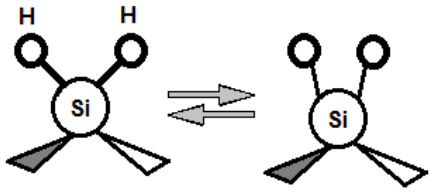	840 – 890 cm^{-1}
Stretching	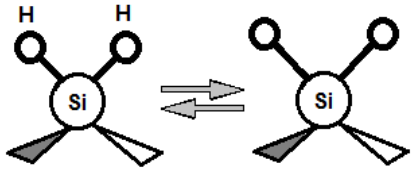	1980 – 2030 cm^{-1} and 2060 – 2160 cm^{-1}

Table 5.1: The characteristic absorption of a-Si:H.

5.1.2 Optical Absorption

A report produced by Mazur and co-workers describes the creation of arrays of sharp conical spikes by using a laser-chemical etching technique [5]. Later, they demonstrated that the structure exhibits very good absorptance in the region from near ultraviolet to near infrared [6]. Based on the reports, several experiments including UV-Vis and transmittance-reflectance measurements have been used to study the absorption properties of microstructures produced by laser processed amorphous silicon. Comparable results using this system will give advantages over of the latter technique as it less complicated and suitable for large area applications.

5.1.3 Localisation of Light

The motion of electrons in crystals is depicted by energy band diagrams where bands are separated by forbidden gaps as a result of the wave nature of electrons and periodicity of the crystal. The disorder in the amorphous silicon structure deters the electron conductivity at certain energy where the localisation of the wavefunction takes place [23]. Although the phenomenon was discussed first in 1958, only in the 1980's scientist started working on relating this phenomenon to the light propagation behaviour in appropriate dielectric medium [94-96]. The localisation of light was known as an effect that arises from coherent multiple scattering and interference in the scale of the incident wavelength.

The localisation of light occurs at the scale of classical physics, however it also has an effect at the quantum level. A complete photonic bandgap is shown when a dielectric medium microstructure having no propagation modes for a certain range of frequencies. This type of microstructure could possibly be made up from periodic arrays of high dielectrics spheres (3-D), or pillars (2-D) in the size comparable to the incident wavelength. For a given microstructure which has no propagation modes in the forbidden frequency, introduction of impurity atoms will introduce localised modes in the gap. But with a transition frequency in the band gap, it will not exhibit spontaneous emission of light; instead it will form a bound state to the atom [94-98]. The effect on localisation of light in high density disorder pillars structure will be studied in this chapter by developing simulation models based on the parameters of microstructures produced by laser irradiation of amorphous silicon, and represents an analogue of the Anderson localisation described earlier in section 2.3.3.

5.2 Experimental Techniques

5.2.1 Fourier Transform Infrared Spectroscopy

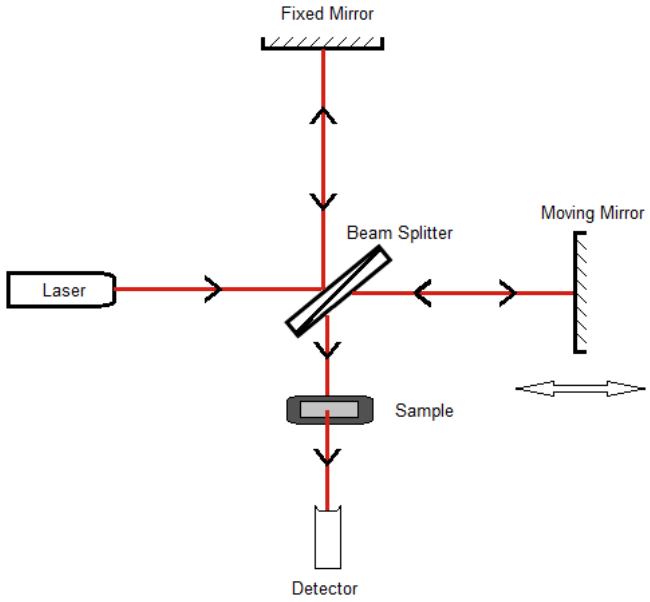

Figure 5.2: Schematic layout of an FTIR system.

FTIR is known as the preferred method in infrared spectroscopy. The optical path inside the FTIR system is shown in figure 5.2. The work flow of an FTIR system is as follows. The IR from the laser source reaches the beam splitter and divides the initial beam into two optical beams. One of the beams reflects to the fixed mirror before it is reflected back. The other beam goes straight to the moving mirror before reflecting back to the beam splitter. The moving mirror is assigned to move at a very short distance around several millimetres further from the beam splitter. Back at the beam splitter, the two beams meets and since the beams have different optical paths, interference occurs which gives a unique signal for every sample data.

The data from FTIR measurement spectra represent the molecular absorption and transmission and is usually referred to as the molecular fingerprint of the material. The unique feature of FTIR made this spectroscopy very useful to identify the presence of material, and to determine the amount and the consistency of a material in a sample. In the experiments, the FTIR spectroscopy is used to identify and measure the hydrogen and oxygen content in the laser processed amorphous silicon film. The employed device was a Mattson 7000 Galaxy spectrometer which has a measurement range from 400 to 4000 cm^{-1} at a scan rate of 0.4 cm s^{-1}. During operation, the sample space was flushed continuously with nitrogen in order to reduce the background absorption spectra of CO_2 and H_2O.

The total concentration of bonded hydrogen in the amorphous silicon film was determined using method developed by Goldie and Persheyev [99]. This method involves Gaussian curve fitting at the vibration peak for the particular vibration mode of Si-H_x bonding.

5.2.2 Ultraviolet and Visible Transmission Spectroscopy

UV-Vis spectroscopy is used to measure the wavelength and intensity of transmission in the region of the near UV and visible spectrum of the laser processed amorphous silicon sample. For the measurement, a Shimadzu UV-Vis 1201 Spectrophotometer was used. The optical path inside the UV-Vis system is shown in figure 5.3. There are two types of light sources, a tungsten lamp which provides visible wavelength at 400 to 1100 nm, and a deuterium lamp for UV wavelengths

from 200 to 400 nm. A beam from the sources is separated into its component wavelength by the concave grating. Then, each of the monochromatic beams is passed to a section mirror which divides it into two beams. One of the beams passed through a reference which in this case is the Corning 7059 glass and the other beam passed to the laser crystallised sample. Both beams combine at the grid mirror and the intensity of the beam is measured by a photomultiplier. The data from the photomultiplier is collected throughout all the spectrum of UV and visible wavelengths and then will finally gives the transmissions plot of the sample.

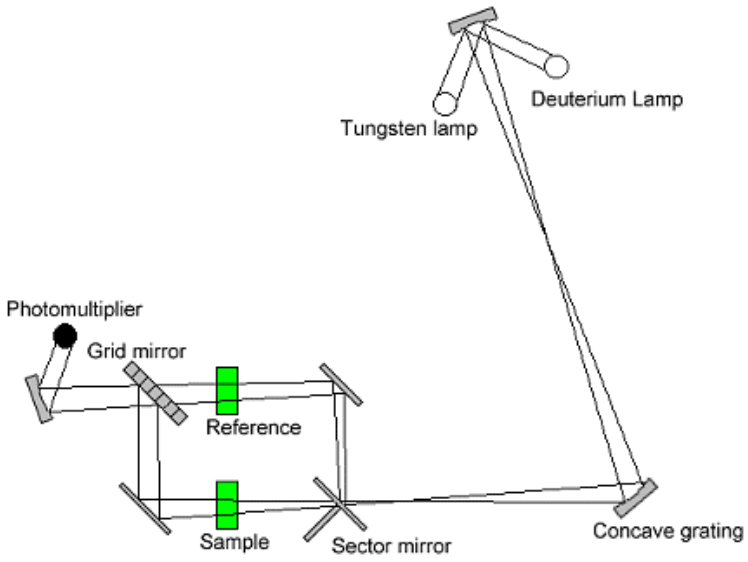

Figure 5.3: Schematic layout of UV-Vis measurement system [100].

5.2.3 Transmission-Reflectance Measurements

Another setup was created to compliment the study of the absorption properties of laser processed amorphous silicon. The setup was used to study the transmission and reflectance characteristics of the sample. As shown in figure 5.4, it consists of a laser source which passes through the sample, held by a rotating stage. There are two photodetectors used, one on the left and the other one on the right. The intensity of the transmitted beam is collected by the photodetector on the right, while the reflected beam is collected by the other photodetector. The signals from both photodetectors are saved onto a PC for analysis. With this setup, the variation in transmission and reflection according to different incident angles was also studied.

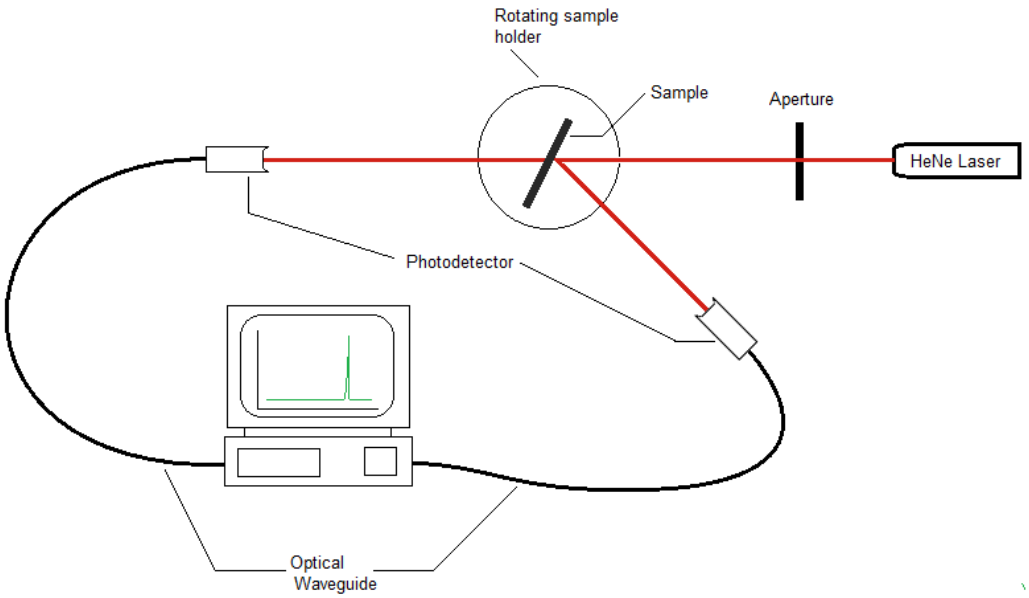

Figure 5.4: Schematic layout of T-R measurement system.

5.2.4 Sample Preparation

For FTIR measurements, the samples are required to sit on a transparent substrate so that the IR laser beam could penetrate. Therefore, only for this time the sample was prepared on n-type silicon wafer. 300 nm amorphous silicon films were prepared by PECVD as in the previous sample preparation condition. Then, the laser irradiation process was carried out at several energy densities to represent the effect at low, intermediate and high fluence. Then the sample was ready for FTIR measurement.

For UV-Vis measurement, the samples were prepared by depositing 300 nm amorphous silicon on Corning 7059 glass substrate by PECVD. Then the sample was subject to irradiation at laser fluences of 131.3, 175, 218.8, 256.6, and 312.5 mJ/cm^2 in the HE scanning scheme. Another sample was produced in a similar way with the LE scanning scheme. Then the UV-Vis measurement was carried out to measure the absorption spectra for non treated sample, and HE and LE scheme samples. Analysis and comparison was made based on the acquired results. Finally, the similar sample preparation as in the UV-Vis measurement samples were made for the transmission-reflectance measurement.

5.3 Results and Discussion on Hydrogen Content

5.3.1 HE Scheme Sample

The FTIR spectroscopy measurements were carried out to investigate the absorption peak of the laser processed amorphous silicon. From the absorption peak, analysis can be done to identify the type of bonding involved quantitatively and further analysis was carried out to calculate the percentage of hydrogen content. Figure 5.5 shows the FTIR absorption spectra for the HE scan sample at different laser fluence and comparison with the original untreated amorphous silicon.

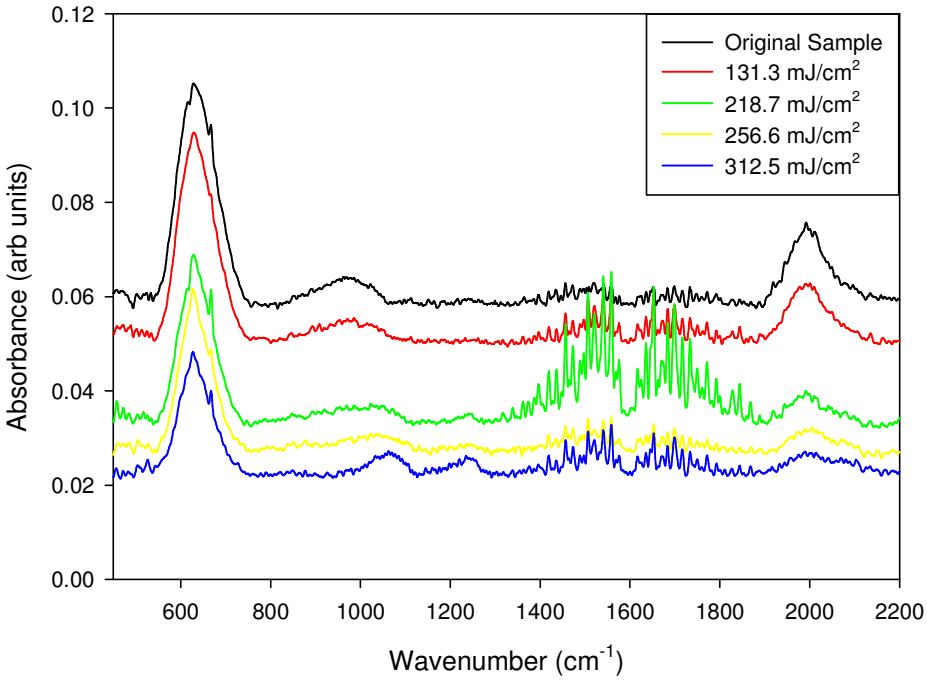

Figure 5.5: FTIR absorbance spectra against wavenumber of HE samples for laser fluence at 131.25 mJ/cm^2 to 312 mJ/cm^2 HE and the original film sample.

All of the spectra feature strong absorbance peaks occurring at 640 cm^{-1} on the left and between 1980 and 2100 cm^{-1} on the right. Quantitative analysis will cover strong absorbance demonstrate at these two peaks. The absorbance features belong to specific SiH_2 and SiH_3 bonding between 840 and 890 cm^{-1} are not detected in the spectra and it was believed due to very low concentration as been described by Persheyev for similar sample [99]. The presence of an absorbance peak between wavenumber at 1350 and 1850 cm^{-1} was due to the existence of water molecules. The features in figure 5.5 are associated with the Si-H bonds that have a bend mode at 640 cm^{-1} and two stretch modes at 2000 and 2095 cm^{-1}. While, the Si-H_2 bonds have a wag mode at 640 cm^{-1} and a stretch mode at 2095 cm^{-1} [101-102]. The feature for the original sample is the typical FTIR absorbance spectra of hydrogenated amorphous silicon prepared by PECVD. The absorbance peak at the wavenumber of 640 cm^{-1} is much stronger than the other peak at the wavenumber between 1980 and 2100cm^{-1}. The presence of water absorbance peaks are usually low and could be easily reduced by routinely flushing the sample prior to measurement.

The FTIR absorbance spectrum shows a changing feature with the application of laser irradiation. At low laser fluence 131.25mJ/cm^2, the difference was not very clear except for small decreases for those two peaks. Additionally, it also shows that there is a small increase in the water absorbance peaks. For the second lowest applied laser fluence 218.7 mJ/cm^2, the reductions for both absorbance peaks are getting more obvious. The water absorbance peaks also increased although the process of flushing the sample prior to measurement was already taken into account to reduce these peaks. Further increases in the applied

laser fluence effectively reduced both of the absorbance peaks to a much lower value. At wavenumber of 640 cm^{-1}, the peak was still obvious with a quite different feature from the original sample. However, for the peaks between 1980 and 2100cm^{-1}, the features are completely different and almost unrecognisable if not carefully observed. The effect from the laser irradiation clearly shows the reduction in the Si-H_x absorption which are directly translated as the reduction of hydrogen content from the process of hydrogen liberation due to the rapid melting and resolidication of the amorphous silicon.

5.3.2 LE Scheme Sample

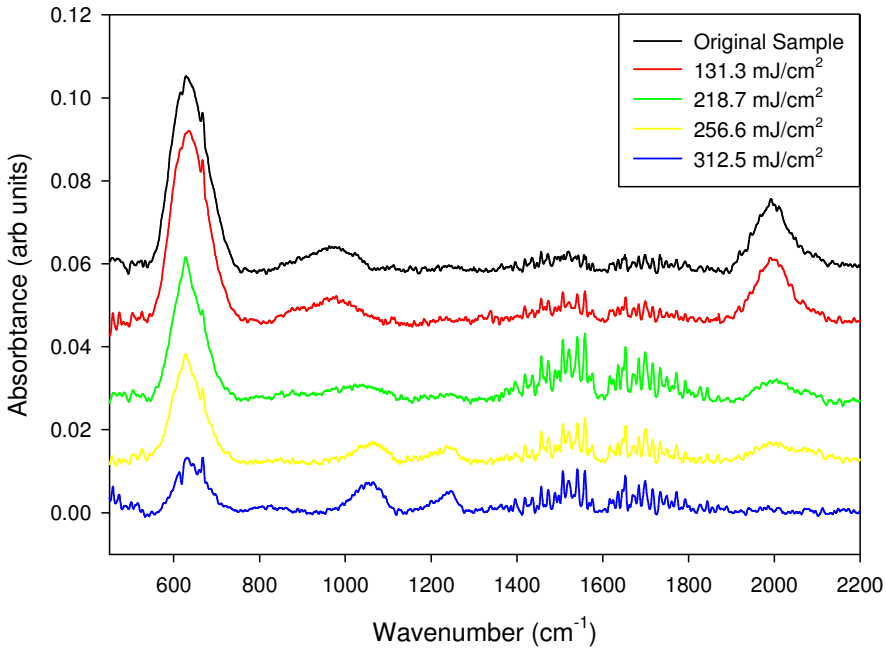

Figure 5.6: FTIR absorbance spectra against wavenumber of LE samples for laser fluence at 131.25 mJ/cm2 to 312 mJ/cm^2 and compared to the spectra of the original film sample.

The hydrogen peak spectra for the LE scheme sample is shown in figure 5.6. Similar features are shown if to be compared with the trend in the laser process HE scheme samples. For the lowest laser applied fluence at 131.3 mJ/cm^2, the feature is much like the original sample. The difference in the feature started to become obvious with the second lowest applied laser fluence. It can be seen from the spectra that the reduction at both absorbance peaks was much clearer. Additionally, the water absorbance peaks are the highest at this laser fluence, which was similar to the case of the HE scheme. With the application of a much higher laser fluence, the reduction of the absorbance peaks became clearer. For the highest applied laser fluence of 312.5 mJ/cm^2, only a small absorbance peak showed at wavenumber of 640 cm^{-1}, while the other peaks between 1980 and 2100cm^{-1} almost completely disappeared from the spectra. At this point, it can be seen that the LE scheme gives more reduction of the absorbance peaks compare to the previous HE scheme. Further observation is made by comparing the concentration of bonded hydrogen in the following section.

5.3.2 Concentration of Bonded Hydrogen

In this section, analysis was carried out to determine the amount of bonded hydrogen in the film samples. The analysis was carried out by using non-linear, quasi-Newton algorithm to perform Gaussian fitting at restricted wavenumber regions of the FTIR data [99]. This analysis was possible by using a Mathcad software program which was dedicated to do this calculation and was developed by Goldie. The software works first by calibrating and deconvolution fitting the

recorded spectrum, and then the area of the interested wavenumber is calculated. The results from the analysis are shown as in the figure 5.7.

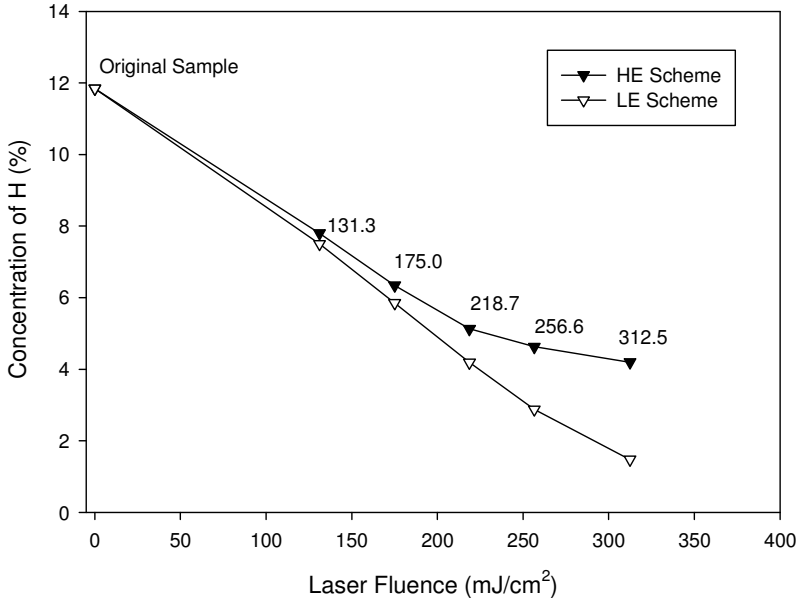

Figure 5.7: Percentage concentration of bonded hydrogen against the applied laser fluence for HE and LE scheme samples.

From the analysis, the concentration of bonded hydrogen for original amorphous silicon film sample was nearly 12%. For the HE scheme sample, the laser irradiation at the lowest laser fluence 131.3 J/cm^2 leads to the reduction of hydrogen concentration to 7.8%. The increase of the applied laser fluence leads to further reduction where at the highest laser fluence 312.5 mJ/cm^2, the hydrogen concentration drops to 4.2%. From the plot, it could be predicted that if much higher fluence was applied, the concentration will reduce to a steady state value around 4% if the film was not completely ablated. This value was very close to 5% which previously reported [103] for explosive crystallisation of amorphous silicon using

step-by-step crystallisation method. For the LE scheme samples, the trend was very similar except that the hydrogen reduction was higher than in the HE scheme samples. At the lowest laser fluence, the hydrogen concentration was almost the same. But as the laser fluence increases, the hydrogen reductions are much greater and at the highest applied laser fluence, the concentration was further reduced to 1.5%. If much higher laser fluence was applied, the hydrogen concentration was believed to stay around this value until the film completely ablated. From this observation, it shows that although the same laser fluence was applied to the amorphous silicon film, different scanning scheme will give different results to the final concentration of bonded hydrogen. This will definitely affect the electrical performance as has been observed and discussed in the previous chapter 4.

Further analysis using Photothermal Deflection Spectroscopy (PDS) as shown in figure 5.8 reveals the plot of absorption coefficient for both HE and LE scheme samples and comparison with a crystalline silicon sample. The plot shows clear evidence that the laser processed samples do not possess the absorption profile as expected from a crystalline sample, but instead the absorption profile is more closely related to the profile demonstrated in amorphous silicon and electron bombarded microcrystalline silicon [104-105]. Additionally, elemental analysis using Energy-dispersive X-ray spectroscopy (EDX) in figure 5.9 for microstructures demonstrate the presence of silicon and oxygen peaks. The oxide matches with the gas environment and volume expansion. Therefore, this is evidence that other than having an amorphous characteristic, the processed materials also contain oxygen incorporated into the structure.

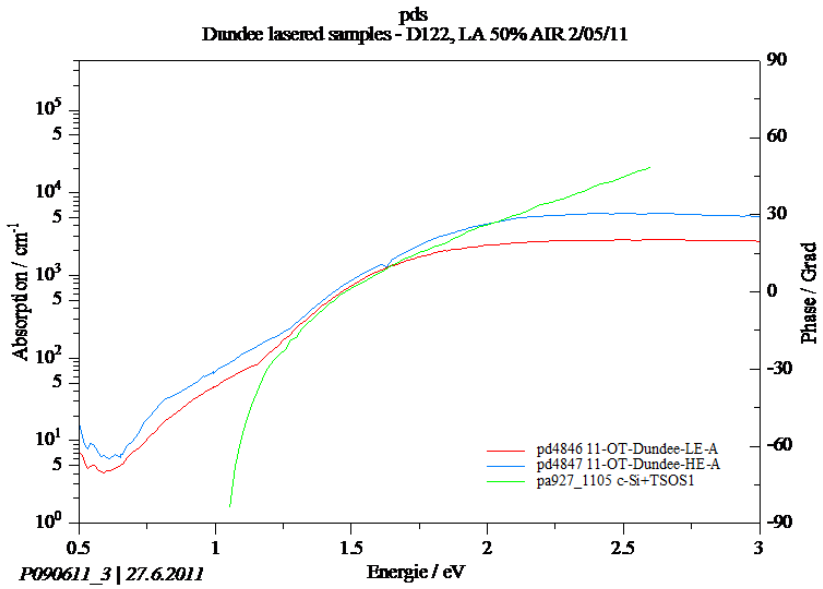

Figure 5.8: Plot of absorption coefficient against energy for LE scheme (red), HE scheme (blue) and crystalline silicon (green) samples using PDS technique. (PDS measurements were carried out by R. Carius from Forschungszentrum Juelich GmbH).

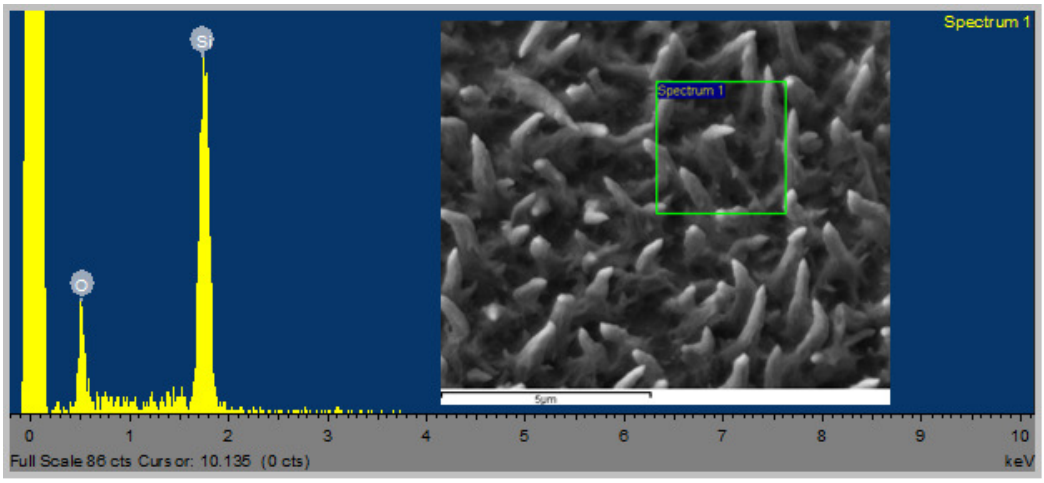

Figure 5.9: Plot of EDX spectroscopy analysis reveals only silicon and oxygen were detected. The green box represents area of interest.

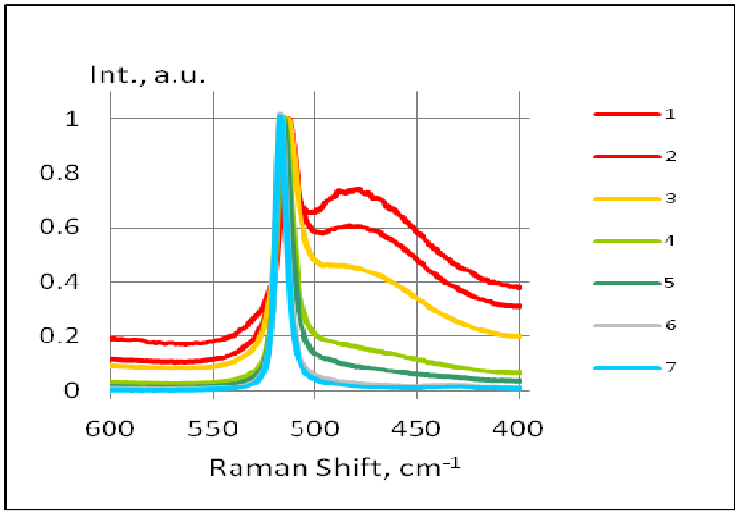

Figure 5.10: Raman spectroscopy results of laser processed amorphous silicon film. Laser fluences were varies at 1-140, 2-156, 3-177, 4-213, 5-233, 6-260, 7- 277 mJ/cm^2.

Analysis using Raman spectroscopy was carried out using the same material and the results are presented in figure 5.10. (The author is grateful to Prof. Ravi Silva of the Advanced Technology Institute at the University of Surrey for these measurements). From the results, it reveals transformation in laser processed amorphous films from low (140 mJ/cm^2) to higher (277 mJ/cm^2) laser fluence. The plot at the low fluence shows a broad Raman scattering which indicates an amorphous phase and has a peak at 480 cm^{-1}. As the laser fluence increased to maximum, the Raman scattering showed a spectral shift with a peak at 520 cm^{-1}, which demonstrates nanocrystalline character. These results point to the formation of a nanocomposite materials that preserve some amorphous character with the inclusion of nitrogen and oxygen, but with increasing crystal fraction with increasing energy. The implication of these results together with the hydrogen content, conductivity and electrical characterisation will be discussed in Chapter 6.

5.4 Results and Discussion on Optical Transmissions

5.4.1 HE Scheme Samples

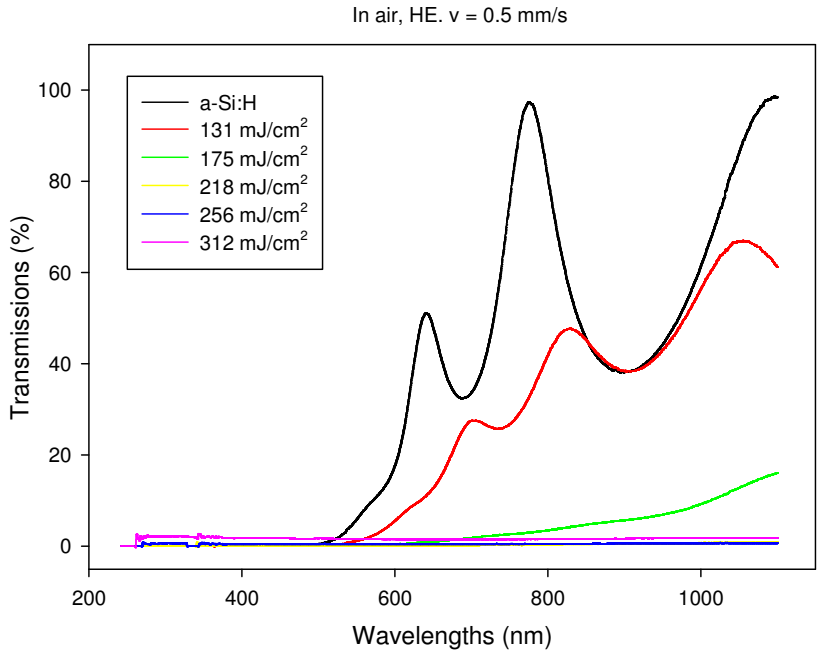

Figure 5.11: The transmission profile from the UV-Vis measurements for HE scheme sample at different laser fluences.

In this section, the discussion will cover the optical transmission results from the UV-Vis measurements. The measurements cover the wavelengths between 200 to 1100 nm. The results will reveal the transmissions profile of the laser processed amorphous silicon. The results for HE scheme samples measurements are shown in figure 5.11. The transmission profile for the original film has been included for comparison.

From the results, it is shown that wavelengths below 500 nm which were in the region of UV were completely absorbed by the original amorphous silicon film.

The wavelengths beyond 600 nm were not highly absorbed by the film, hence the transmission was increased steadily reaching a maximum value at the highest wavelength of 1100 nm in the IR region. The profile shows ripple characteristic due to thin film interference. The first sample at the lowest laser fluence showed an increased in the absorption and it can be seen that the absorption edge was shifted slightly to 550 nm. Ripple is existed but at lower scale due to decrease in film thickness after laser processed. The increased laser fluence in the second sample shows a further increase in the absorption and the absorption edge was shifted further. For the applied laser fluence at 218.7 mJ/cm^2 and higher, the wavelength within 200 to 1100 nm in these measurements was shown to be absorbed by the sample by 98 %. At this point, it was demonstrated that higher absorbance was achieved by the laser processed samples compared to the original amorphous film. The following section will shows the results for LE scheme samples.

5.4.2 LE Scheme Samples

The results for LE scheme samples measurements are shown in figure 5.12. The transmission profile for the original sample was also included for comparison purposes. The results for LE scheme were quite surprising. At the lowest laser fluence, the absorption edge was shifted much further compared than the HE scheme sample. Furthermore, this was the only sample that produced a transmission profile. All other samples at higher laser fluence demonstrated blocking all wavelengths in this spectral range.

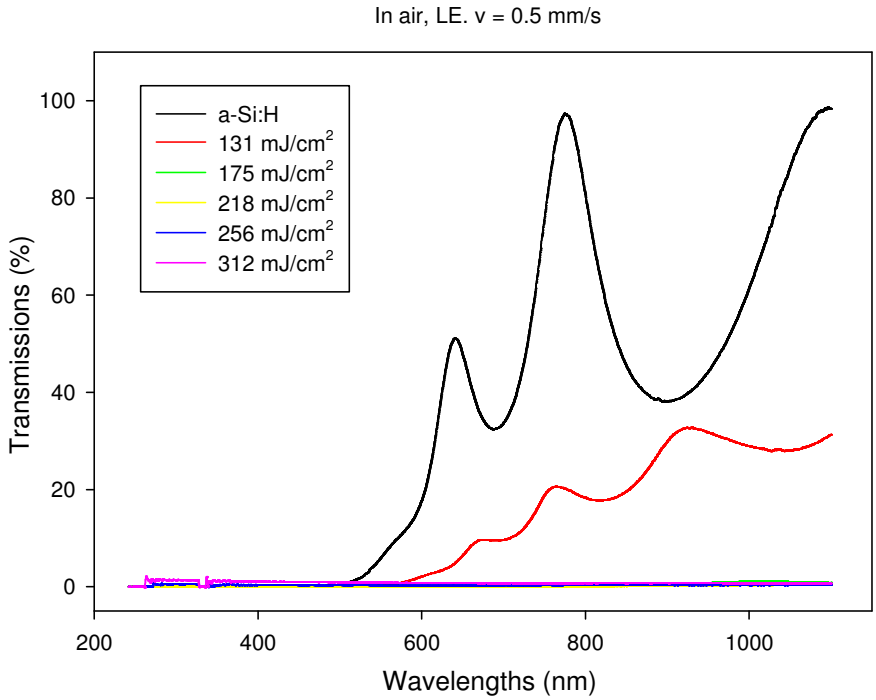

Figure 5.12: The transmission profile from the UV-Vis measurements for LE scheme sample at different laser fluences.

Overall, the optical absorption demonstrate by LE scheme samples were better than the HE scheme samples. The absorption trends in this region could be explained from the surface morphology analysis of the samples. The original amorphous film has a smooth surface compared to the laser processed film. At lower laser fluences, the film surface began to roughen and absorb much more incident light. High fluence leads to the formation of microstructures which traps the light further and reduced the transmittance to nearly zero. The LE scheme sample demonstrates a much higher absorption profile than the HE scheme samples due the microstructure features which cover a bigger surface and traps light more effectively than the sharp spikes as in the HE samples.

5.5 Results on Transmission-Reflectance Measurement

In this section, measurements were carried out as an extension and compliment to the UV-Vis measurements. The Optical Spectrum Analyser (OSA) was used to records the light intensity. Similar samples were used as in the previous section. First, a 75 W bulb was used a light source which has a spectral range of 400 to 800 nm. Then, the bulb was replaced by a He-Ne laser as a powerful source due to limitation of output signal produced by the bulb. The He-Ne laser has a peak power at wavelength of 652nm.

5.5.1 Effect of Transmission towards Angle Variation

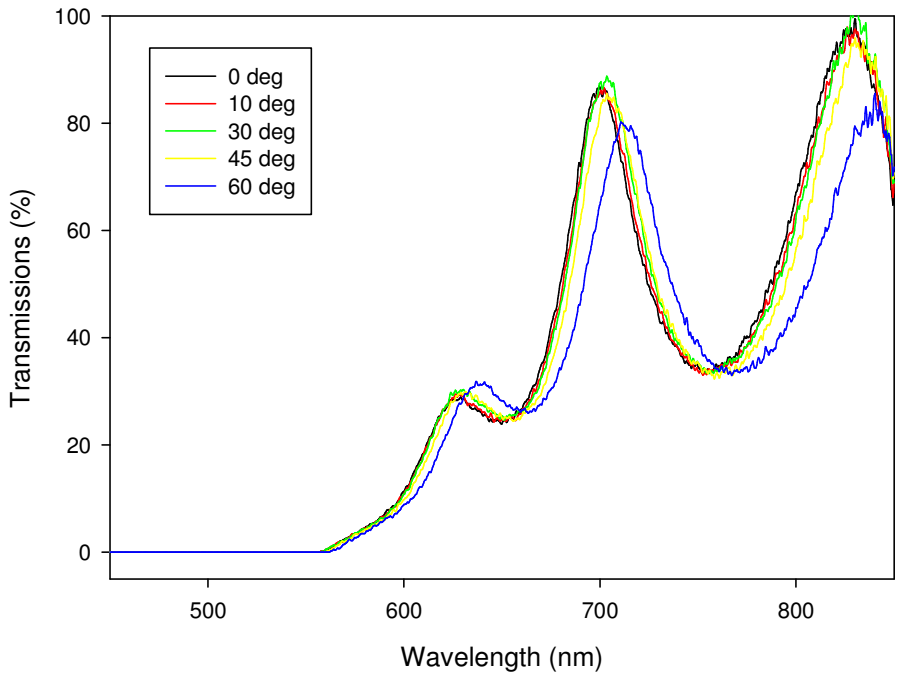

Figure 5.13: Transmission profile at various incident angles for original amorphous silicon film.

The variation of transmission for original amorphous film according to different incident angle is showed as in the figure 5.13. It was revealed that at incident angles below 45^{o} from the normal, the transmission profiles were very much similar if compared to the transmission at 0^{o}. There was only small variation for the transmission profile at incident angle of 60^{o}.

The angle dependent variation for sample with sharp microstructure features is shown in figure 5.14. Although the signal was very small (less than 4%), the drop in the transmission with the increase in incident angles was very clear. At a wavelength of 750 nm, the transmission drops from 1.5% at 0^{o} to 0.3% at 60^{o} from incident angle.

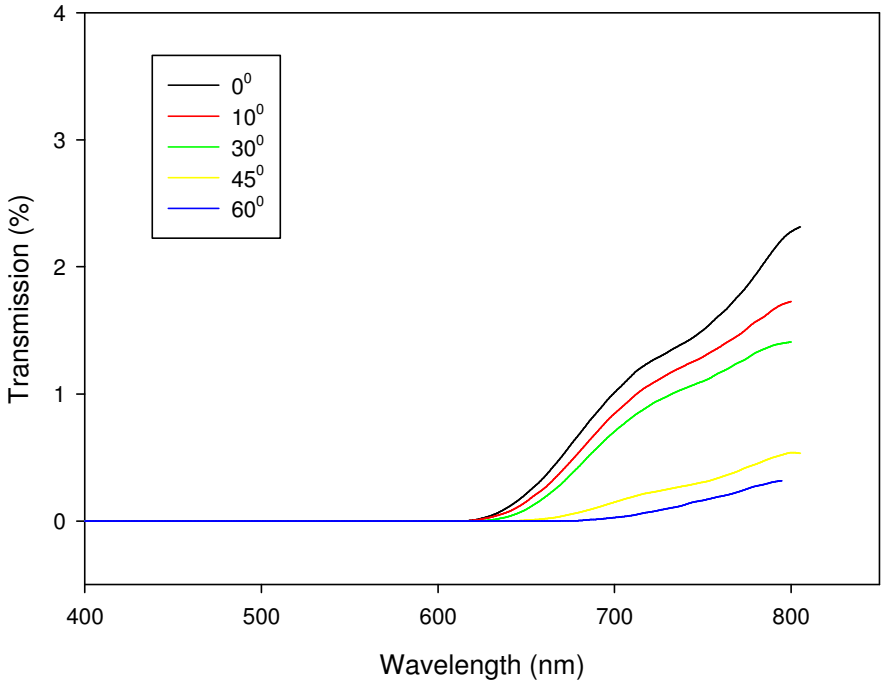

Figure 5.14: Transmission profile at various incident angles for sample irradiated with laser fluence of 218.8 mJ/cm^2 in HE scheme.

The transmission profile for the blunt type of microstructures obtained using LE scheme is shown in figure 5.15. It also reveals the reduction of transmission with the increase of incident angle. However, the reduction trend was not same as in the previous case of the HE scheme sample. The trend was much closer to the transmission signal of the original sample. It showed that the transmission signal at incident angle of 0^o to 45^o from the normal were almost alike. Although the signal reduction at 60^o was very clear. At wavelength of 750 nm, the transmission signal dropped from 1% at 0^o to 0.5% at 60^o.

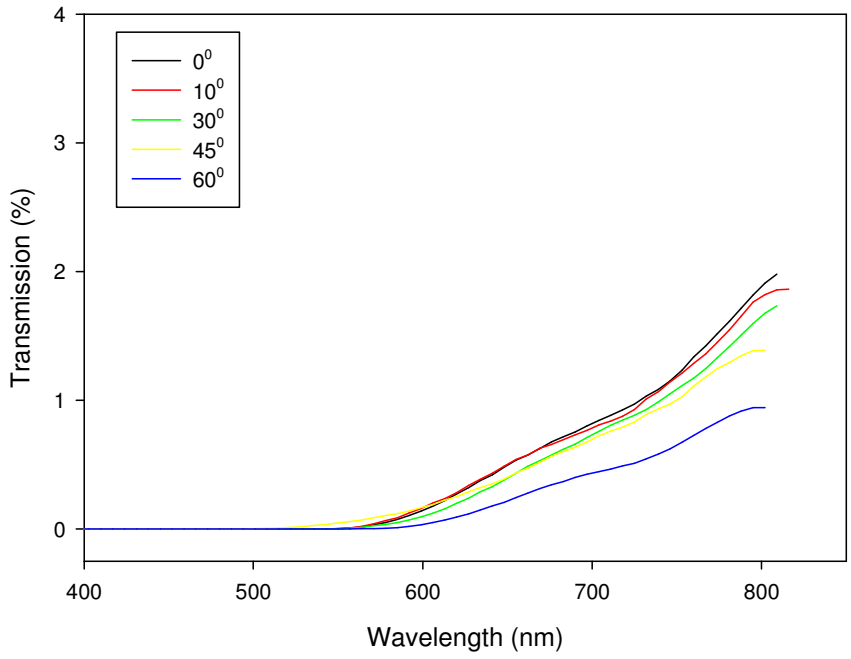

Figure 5.15: Transmission profile at various incident angles for sample irradiated with laser fluence of 218.8 mJ/cm^2 in LE scheme.

The surface roughness was the main factor behind the different results in the transmission signal measurements. The original sample has a smooth surface compared to the laser irradiated samples. Therefore, when the incident angle increased the effect was not very substantial except in the case where the incident angle was at 60^{o}, where the shift in the transmission signal was apparent. This was normally seen in glass optical transmissions due to the decrease in the light intensity at higher incident angle [106].

The HE scheme sample shows a steady decrease in the transmission profile due to the presence of sharp spike features on the surface. The maximum transmission was achieved at an incident angle of 0^{o}. When the incident angle was slightly moved away from the normal, the conical sharp feature on the surface partially absorbed and scattered the incident light, thereby reducing the transmission signal as detected by the sensor. As the incident angle moved further away, the structure absorbs and scatters more of the incident light resulting in further decrease in the transmission signal. Effect of increasing incident angle to the output of the optical transmittance is depicted in figure 5.16.

The LE scheme sample shows little difference in the transmission profile despite the existence of microstructures on the surface. Although previously it showed that this type of structure absorb more light, the variation in the incident angle was not affecting the light transmission much as seen in the HE scheme sample. This was due to the blunt shape of microstructure that does not highly absorb and scatter the incident light as oppose to the sharp spike. However, the

increase in the process of absorbance and scattering of incident light occurs when the incident angle exceeds 60^{o}.

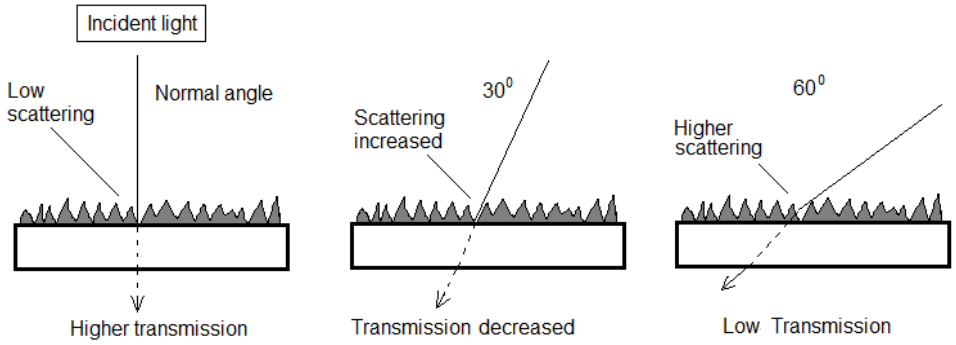

Figure 5.16: Angle dependent of the output optical transmittance for a laser process sample.

5.5.2 Absorbance and Scattering Analysis

The previous measurements were carried out using a 75 W bulb as the light source. However, except for the transmission profile, the reflectance signal was too weak to be detected by the detector. The reflectance measurements were also a very important part of the experiment since with the combination of transmission, the absorbance and scattering analysis can be carried out. For the next measurement, a He-Ne laser was used as the light source. The laser has peak intensity at the wavelength of 652 nm. Figure 5.17 (a) and (b) shows the combination of transmission and reflection profile at different incident angle against the applied laser fluence for both the HE and LE scheme samples.

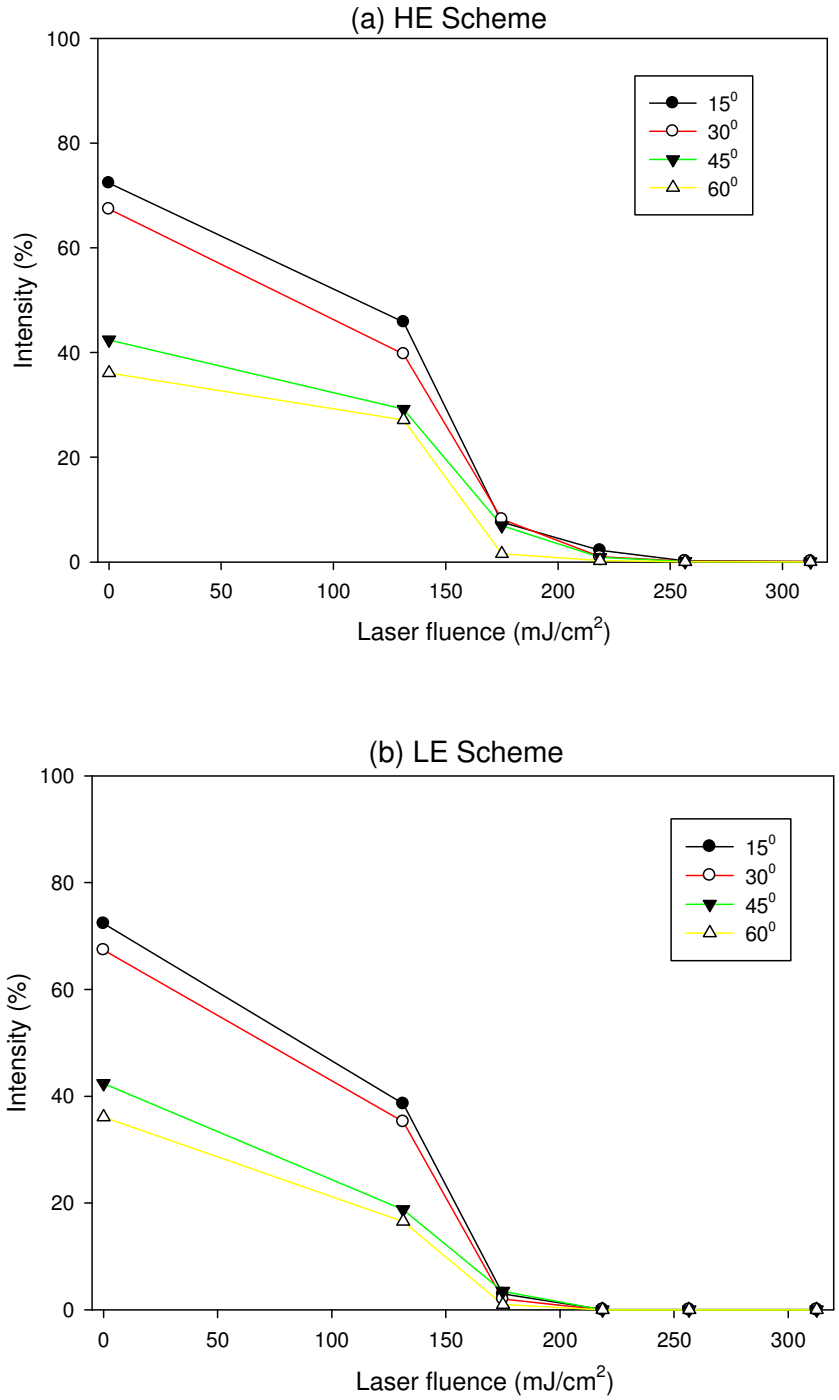

Figure 5.17: Combinations of transmission and reflectance intensity at various incident angles and their variation towards the applied laser fluence for (a) HE and (b) LE scheme samples.

Both of the plots show trends of decreasing intensity of transmission and reflection with increasing the incident angle. And the intensity also decreases when the applied laser fluence increases. As described before, the LE scheme sample demonstrate less intensity compared to the HE scheme sample. On the other hand, the small output intensity suggests that the light absorbance and scattering were very high. It is believed that the increase in applied laser fluence leading to the increase of the microstructure size which then more effectively absorbs and scatters the light source.

5.6 Results on Simulations of Photonic Crystal

5.6.1 Introduction

The experimental work in this thesis, in combination with the microstructure analysis suggests an opportunity to study light interactions with the highly dense array of surface features on the material and to exploit this as a disordered photonic crystal. The apparent random nature in the distribution of the features suggests also that we may be able to find an amorphous band gap analogue for the photonic structure and perhaps be able to localise light in this material.

The laser processed materials forms a two dimensional array of pillars, and can be classed as a metamaterial. The material can be classed as a two dimensional disordered photonic crystal. This section describes the structure of the features and predicts a number of applications by examining the interaction of the structures with electromagnetic radiation. Because of the interaction of the structure with e.m. radiation we should find an analogue of the photonic band gap in ordered arrays with a disordered system band gap such as that found in an amorphous material.

The Bloch condition in an ordered crystal leads to the band structure familiar to semiconductor crystals such as silicon. A disordered system following the Anderson model should lead to a localisation of states in the band gap, such as the exponential distribution found in amorphous silicon. An ordered array of pillars will exhibit a photonic band gap. A disordered array should show the photonic equivalent of the optical gap as well as localised modes of light. This is analogous to the localisation effect described in chapter 2, for the case of electrons. There we

discussed the widening energy band gap and localisation of electrons in a disordered silicon matrix. In the case of light, widening in optical gap is expected. This can be exploited in a number of applications.

Three different models based on finite element analysis are presented in order to analyse the propagation of electromagnetic waves thorough the silicon pillars. The E&M Waves module of COMSOL Multiphysics was used to model the arrays and the interactions with e.m. radiation. The first model will represent the results for an ordered array photonic crystals. The second model represents the realistic scale and parameter of the disorder silicon pillars created from laser processed amorphous silicon, and the third model is the same as the second model except at a much smaller physical scale.

5.6.2 Transmission Profile in Ordered Photonic Crystal

The first model geometry is shown in the figure 5.18 for a 2-D square lattice of silicon micropillars and follows the work of Butt et al. [107]. It represents a section of a 2-D lattice of infinite vertical pillars made of silicon in the x-y plane. The pillars dielectric constant was set to $\varepsilon = 13$ and the surrounding was set to fill with air with $\varepsilon_{air} = 1$. The lattice constant of the pillars a was 1.5 µm with a radius r of 0.25 µm. The source of electromagnetic field wave was set to contain a field of 1 V/m and was set propagate from the left side of the geometry to the right. The transverse mode of the electric field was used where the waves are polarised in the z axis and was parallel to the axis of silicon pillars. The simulations were carried out with wavelengths varying from 0.1 to 7 µm.

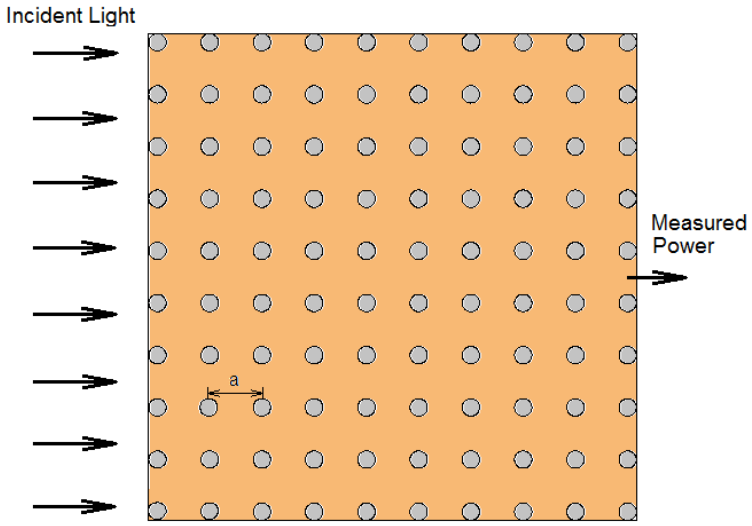

Figure 5.18: Geometry of a 2-D square lattice of silicon pillars surrounded by air with a = 1.5 µm and r = 0.25 µm. Electromagnetic source originated from left and propagate through the pillars to the right direction.

The transmissions intensity of the propagated waves at the middle point on the right side was extracted for the whole wavelength range and is shown in figure 5.19. The plot demonstrates that there is one band gap region. The band gap lies in the range between 3.4 to 5.4 µm where it clearly shows that no wave propagation took place within this wavelength range.

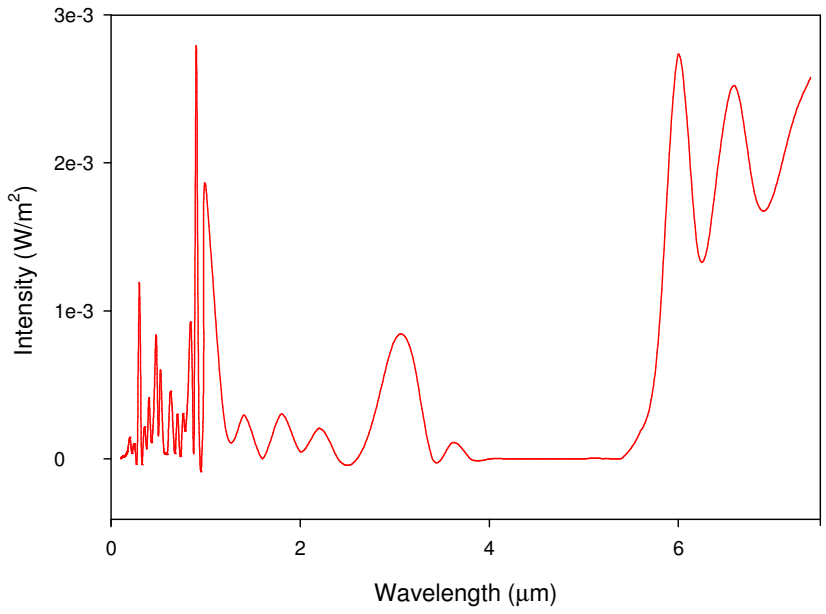

Figure 5.19: Plot of transmission intensity of the wave propagation at the point showed in the middle of the right side of figure 5.18 where it clearly shows a band gap in the range of 3.4 to 5.4 µm.

For deeper analysis, the propagation of electric field across the lattice at wavelengths of 0.9, 3, 4, and 6 µm were simulated and shown in figure 5.20 (a) to

(d). For each wavelength, the first figure on left shows the intensity of the electric field from the plan view of the geometry. The second figure on right shows the intensity of electric field in a 3-D view where the wave propagation took place from left to right. Finally the third figure is the colour chart representing the intensity of the electric field from the minimum (blue) to maximum (red).

The first result at a wavelength of 0.9 μm demonstrates that the wave propagation penetrates across the geometry with very strong scattering. From the 3-D profile in the figure 5.20 (a), it reveals that at the early stage of propagation, the ampitude of the electric fields were of similar amplitude. As the wave propagates, the amplitude of electric field at the centre increased opposed to the electric field on left and right side of the geometry which were decreased. The highest peaks contribute to the maximum value of electric field 5.3 V/m recorded near the measured point.

(a) $\lambda = 0.9\ \mu m$

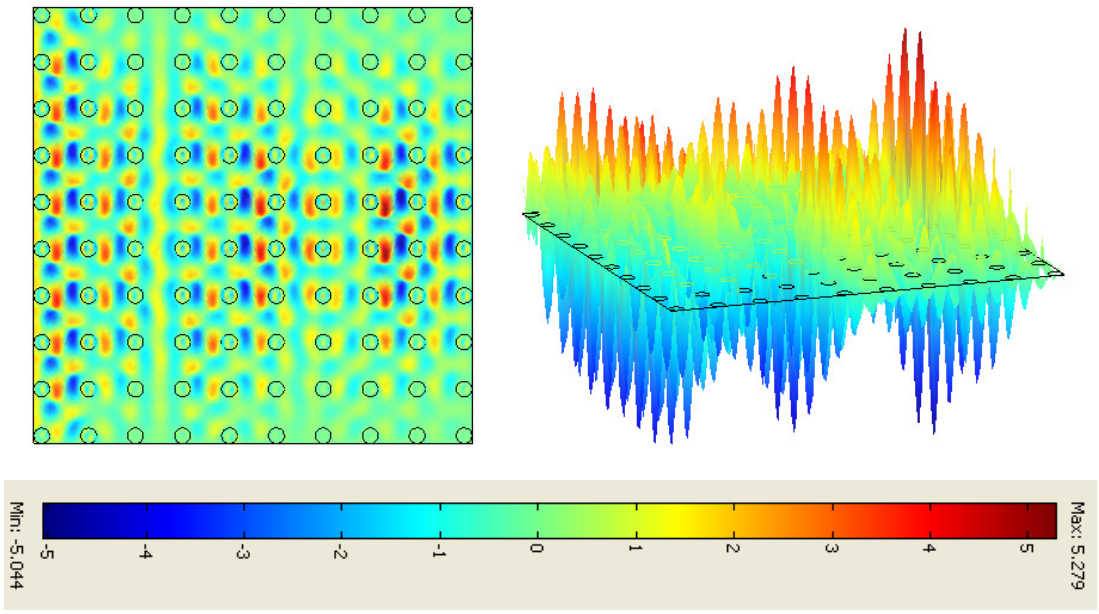

(b) $\lambda = 3\ \mu m$

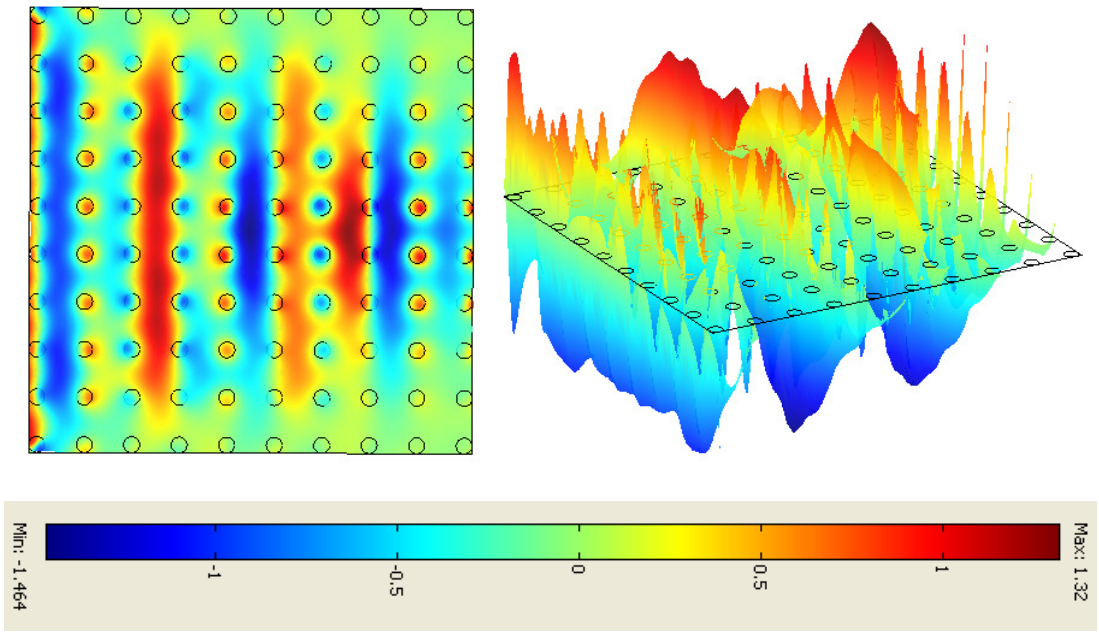

(c) $\lambda = 4\ \mu m$

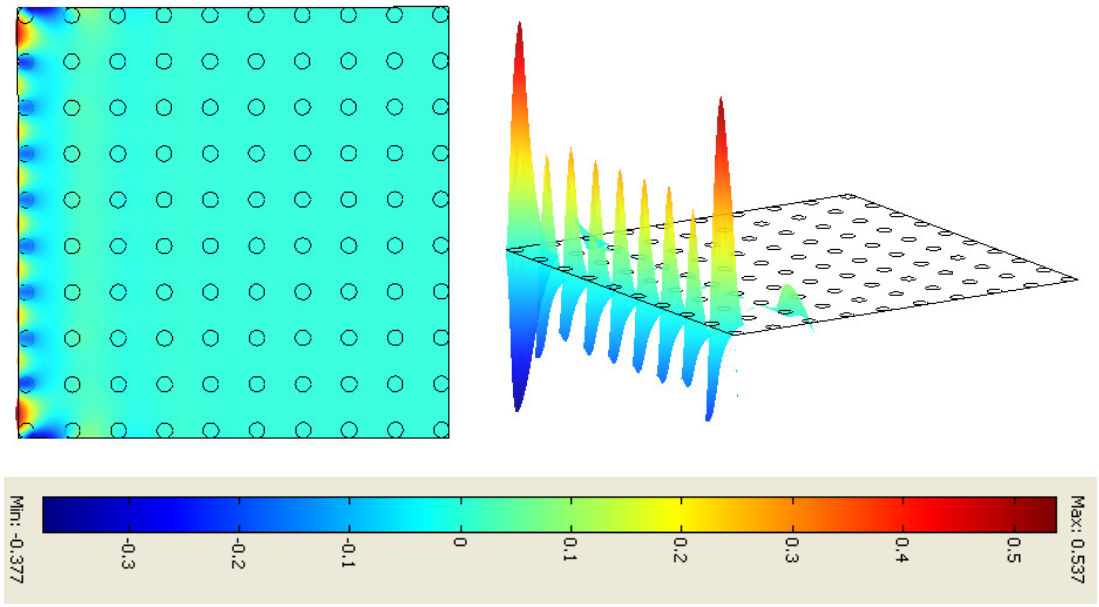

(d) $\lambda = 6\ \mu m$

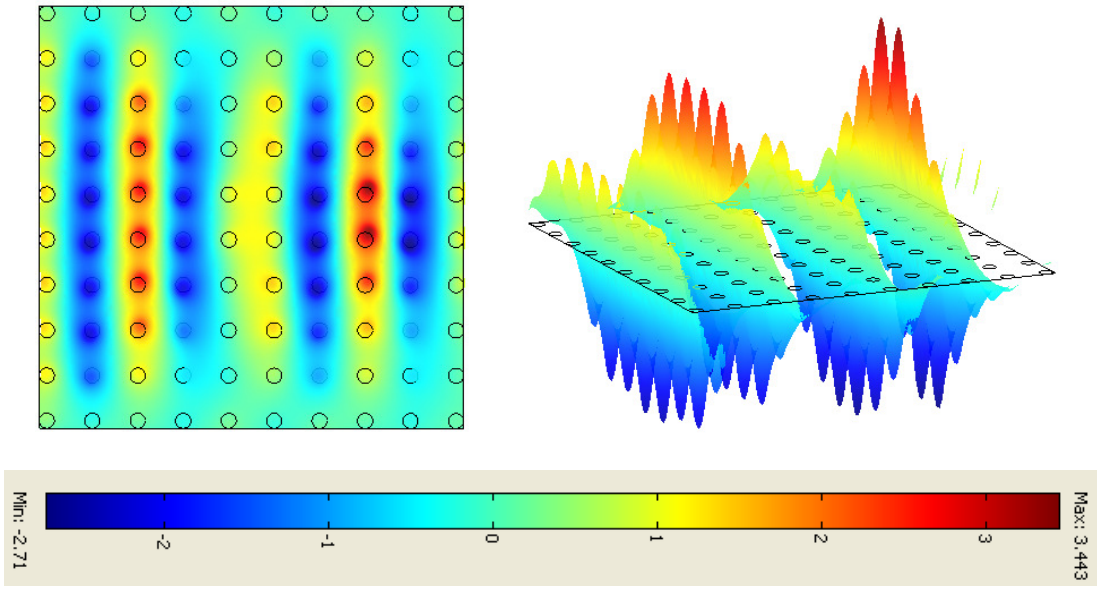

Figure 5.20: Simulation of the wave propagation across the silicon pillars lattice for incident wavelength at (a) 0.9 μm, (b) 3 μm, (c) 4 μm, and (d) 6μm. For each figure, the wave propagate from left to right as showed in the plan view (top left), 3-D view (top left) while the colour chart indicates the intensity of the electric field.

Figure 5.20 (b) shows the propagation of wavelength at 3 μm where this wavelength represents the observed peak in the figure 5.19 which divided the two band gaps. There were two types of peaks noticeable in the wave propagation profile. First, the sharp peaks formed within the silicon pillars and second, constructive peaks formed within the space lattice. The intensity peaks also became concentrated to the centre as the wave propagates across the geometry. Wavelength at 4 μm belongs to the bandgap. As showed in the figure 5.20 (c), the wave was hindered from entering the pillars array at the edge of geometry. The figure also visualised the electrical signal for this type of wavelengths belonging to this region where it was not able to propagate.

For wavelengths above 5.4 μm, the waves were allowed to propagate across the geometry without any problem. Figure 5.20 (d) represents the wave propagation profile for wavelength at 6 μm. It shows an example of a normal propagation mode of the photonic crystal structure. It also shows a similar case to other previously propagation wavelengths where the peak intensity increased towards the centre of the geometry as the wave propagates.

5.6.3 Transmission Profile in Disorder Photonic Crystal 1

Second simulation model was created to represent an analogy of the pillars created from laser processed amorphous silicon. The model geometry is shown in figure 5.21 below and it consists of different sizes of vertical silicon pillars scattered across the geometry. The pillars were assumed to have the similar dielectric constant value as before and the surrounding was set to fill with air as the previous model. The pillars have three different radius values at 0.2, 0.25 and 0.3 μm and distributed randomly without any specific order. The parameters of the incident electromagnetic waves were set to be similar to the previous model. The incident wavelength was also set in the range between 0.1 to 7 μm.

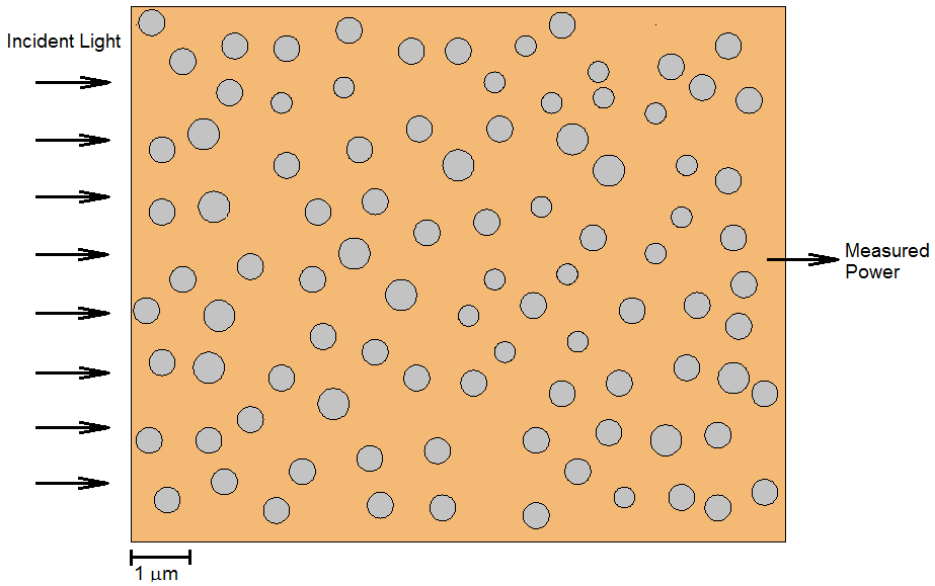

Figure 5.21: Geometry of a 2-D square lattice of disorder silicon pillars surrounded by air. The pillars have three different radiuses sizes at 0.2, 0.25 and 0.3 μm and scattered randomly across the geometry. Electromagnetic source originated from left and propagate through the pillars to the right direction.

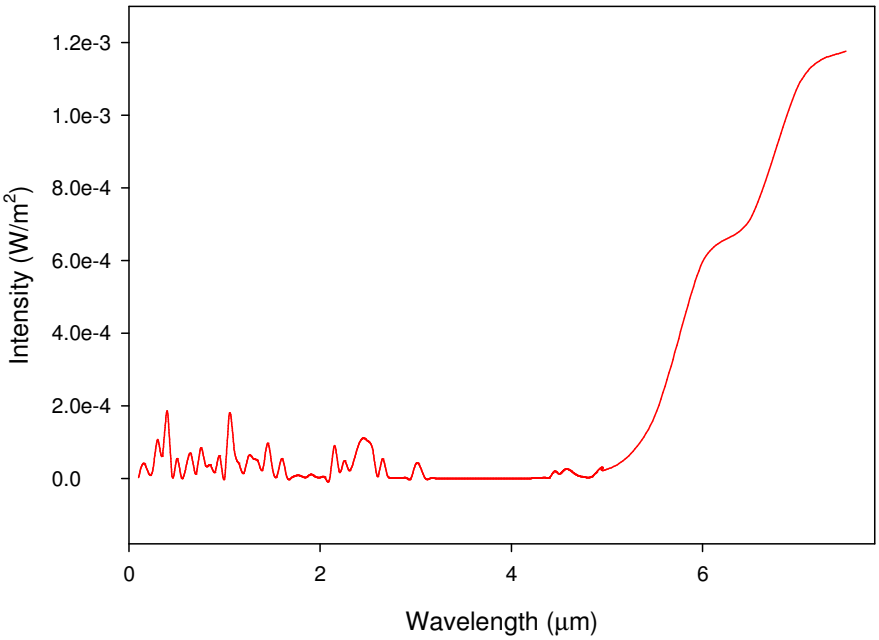

Figure 5.22: Plot of transmission intensity of the wave propagation at the point showed in the middle of the right side of figure 5.21. This model has a clear band gap at wavelength from 3.1 to 4.4 µm.

The transmission intensity of the propagated waves on the same location was extracted for the whole wavelength range and shows in figure 5.22. Although the structure was disordered, it also presents a band gap region between wavelengths of 3.1 to 4.4 µm. Other part of the plot shows transmission with high scattering accross the spectra. For this model, profile of electric field propagation across the geometry at wavelengths of 1, 2, 4, and 6 µm were simulated and showed in figure 5.23.

(a) $\lambda = 1\ \mu m$

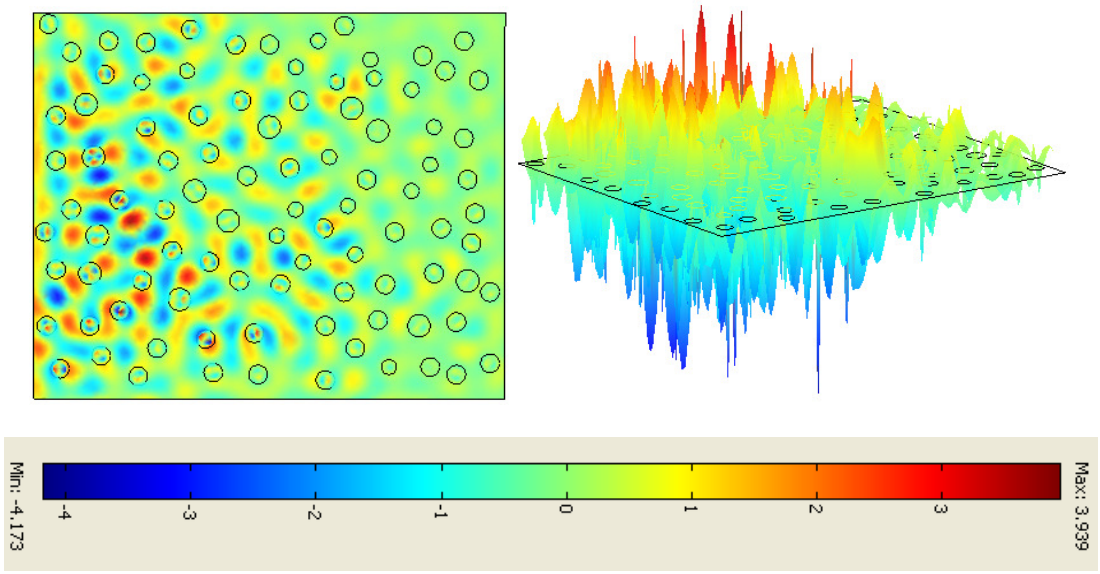

(b) $\lambda = 2\ \mu m$

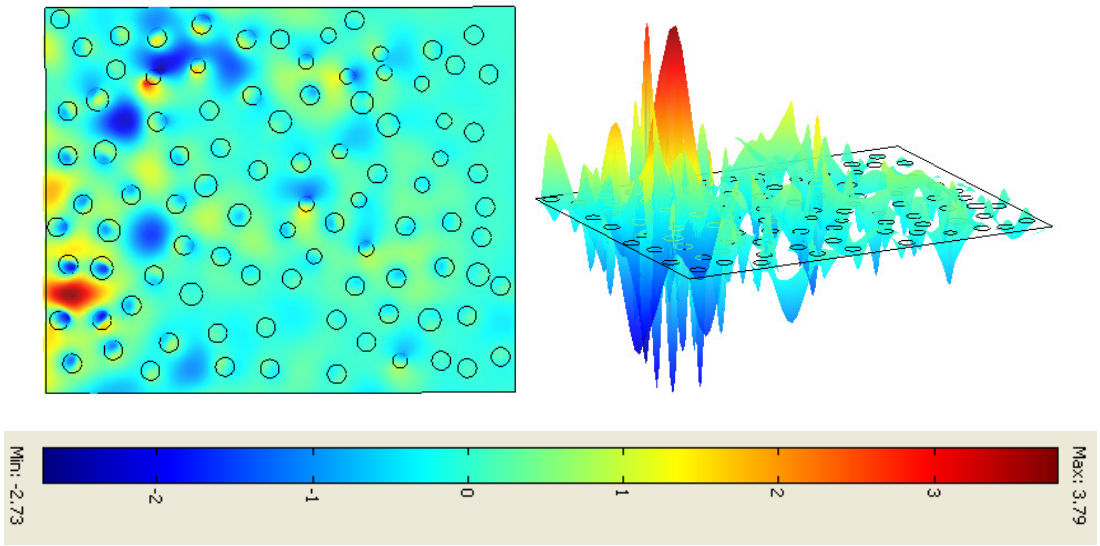

(c) $\lambda = 4\ \mu m$

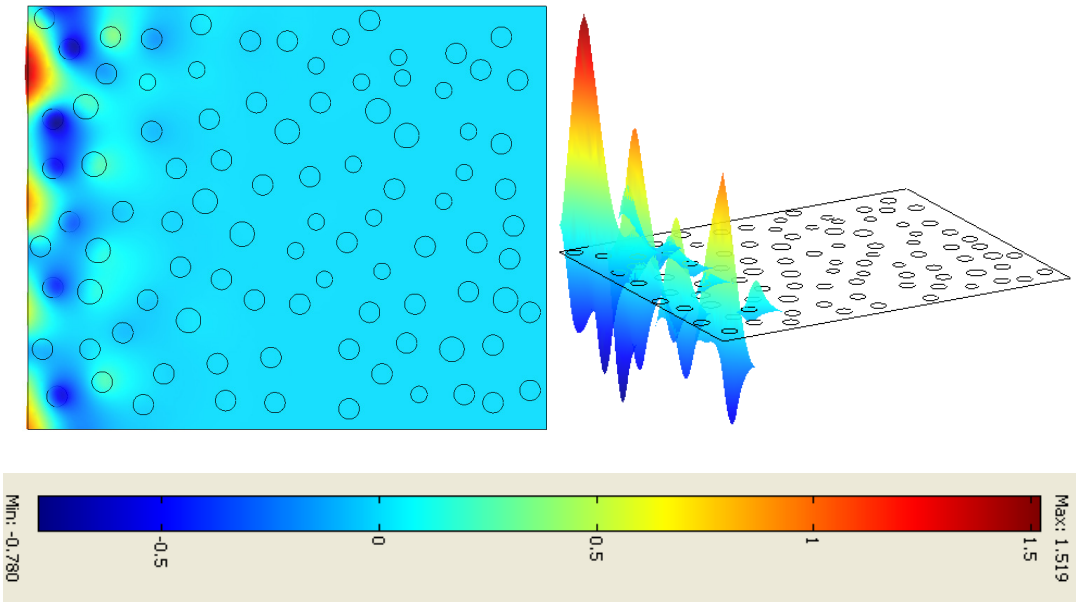

(d) $\lambda = 6\ \mu m$

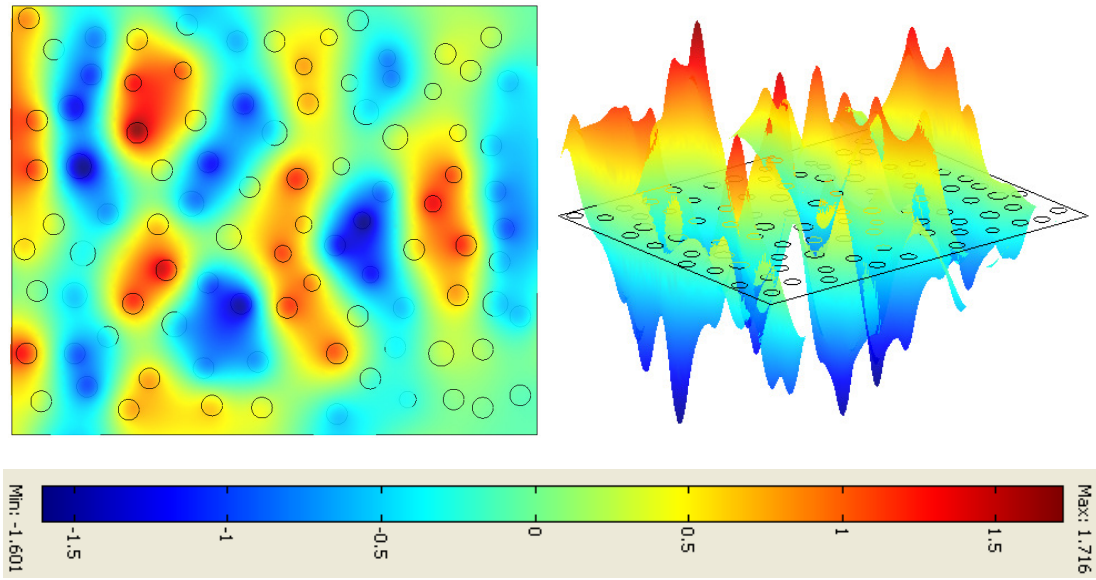

Figure 5.23: Simulation of the wave propagation across the silicon pillars lattice for incident wavelength at (a) 1 μm, (b) 2 μm, (c) 4 μm, and (d) 6μm. For each figure, the wave propagate from left to right as showed in the plan view (top left), 3-D view (top left) while the colour chart indicates the intensity of the electric field.

Wave propagation in the disordered structure was different when compared to the ordered structure. Figure 5.23 (a) shows transmission profile for wavelength at 1 μm, where the wave propagates through the pillars with strong diffusion. The intensity distribution shows many fluctuations due to interference. However very strong scattering leads to transmisssion of light at the end of the geometry but with lower intensity. Localisation of light was also observed due to enhanced backscattering phenomenon within the structure. At a wavelength of 2 μm (figure 5.23 (b)), the diffusion was not as strong as shown by the 1 μm wavelength and this leads to very low intensity detected at the measurement point. However, strong peaks of interference were presented on the left edge.

The next wavelength at 4 μm shown in figure 5.23 (c) belongs to the band gap. Compared to the ordered structure which not allowed any waves belong to the band gap to propagate, it was showed that the wave managed to propagate for the first quarter of the geometry. Figure 5.23 (d) shows the profile for a wavelength of 6 μm which represents the propagation of the electric field for longer wavelengths accross the disorder structure. The diffusion of light occurs in bigger scale where it is scattered randomly and finally reaches the end of the structure with high signal amplitude.

5.6.4 Transmission Profile in Disorder Photonic Crystal 2

A third simulation model was created to study the transmission profile of a disorder photonic crystal at a smaller scale than in the section 5.6.2 to reflect changing conditions in laser processing of the material. Comparison is also made with wave propagation and the effect on light localisation. The geometry of the model is shown in figure 5.24. It consists of three different sizes of vertical silicon pillars with radius of 0.05, 0.075 and 0.1 μm with a random distribution accross the geometry. The surrounding was filled with air as in the previous models. The parameters of the incident electromagnetic waves were set as before, but the incident wavelength was set in the range of 0.1 to 3 μm.

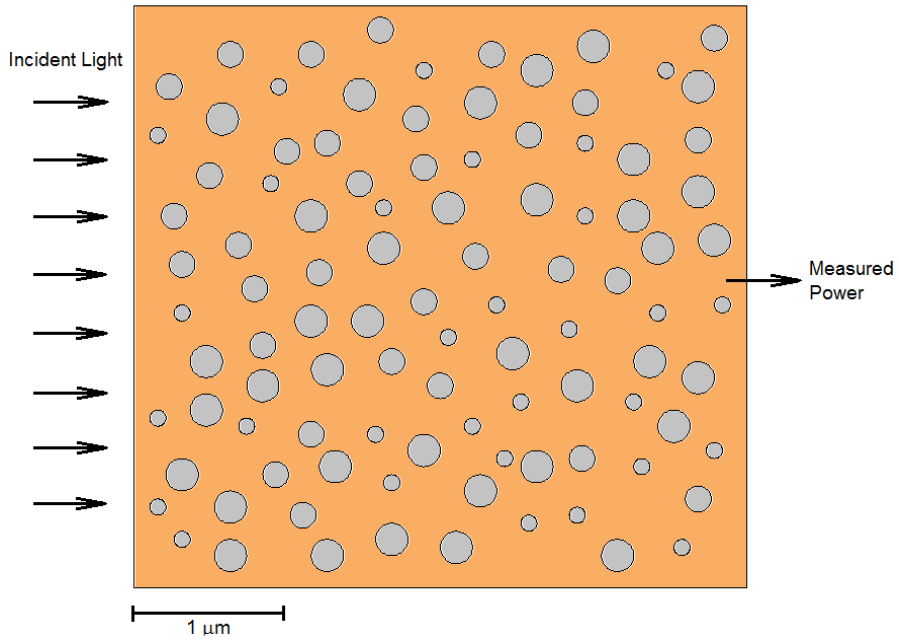

Figure 5.24: Geometry of a smaller scale 2-D square lattice of disorder silicon pillars surrounded by air. The pillars have three different radiuses at 0.05, 0.075 and 0.1 μm and scattered randomly across the geometry. Electromagnetic source originated from left and propagate through the pillars to the right direction.

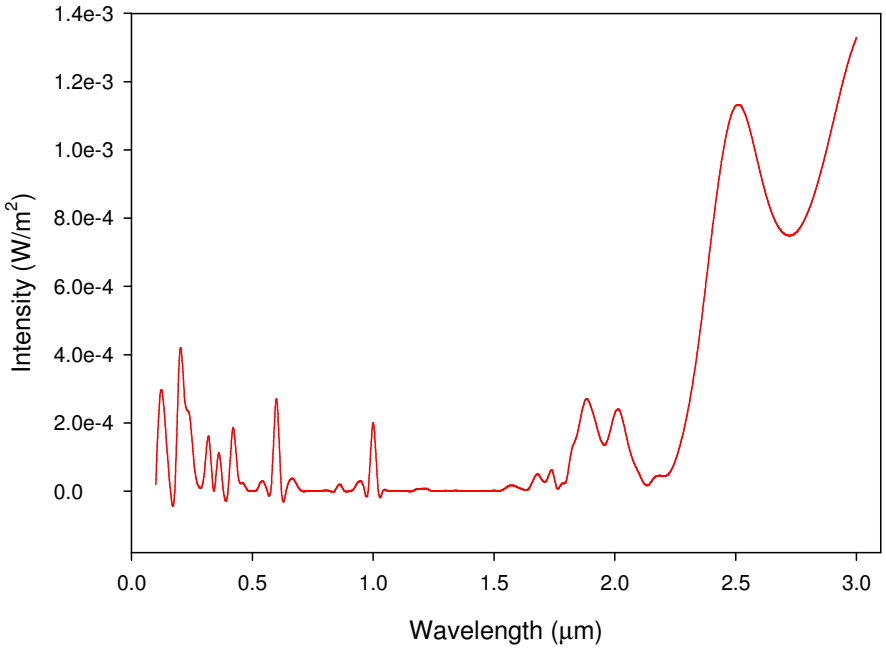

Figure 5.25: Plot of transmission intensity of the wave propagation at the point showed in the middle of the right side of figure 5.24. This model has a small band and a bigger band gap at region between wavelength 0.7 to 0.85 µm and 1.1 to 1.6 µm respectively.

The transmissions intensity of the propagated waves on the same location was extracted for the whole wavelength range and shows in figure 5.25. The transmission plot revealed a shift in band gap region as results from small dimension of pillars and space between pillars. There were two band gap regions identified at wavelength of 0.7 to 0.85 µm and another at 1.1 to 1.6 µm where the first was very narrow while the latter was much wider. A profile of electric field propagation across the geometry at wavelengths of 0.2, 0.5, 1, and 1.3 µm were simulated and are shown in figure 5.26.

(a) $\lambda = 0.2\ \mu m$

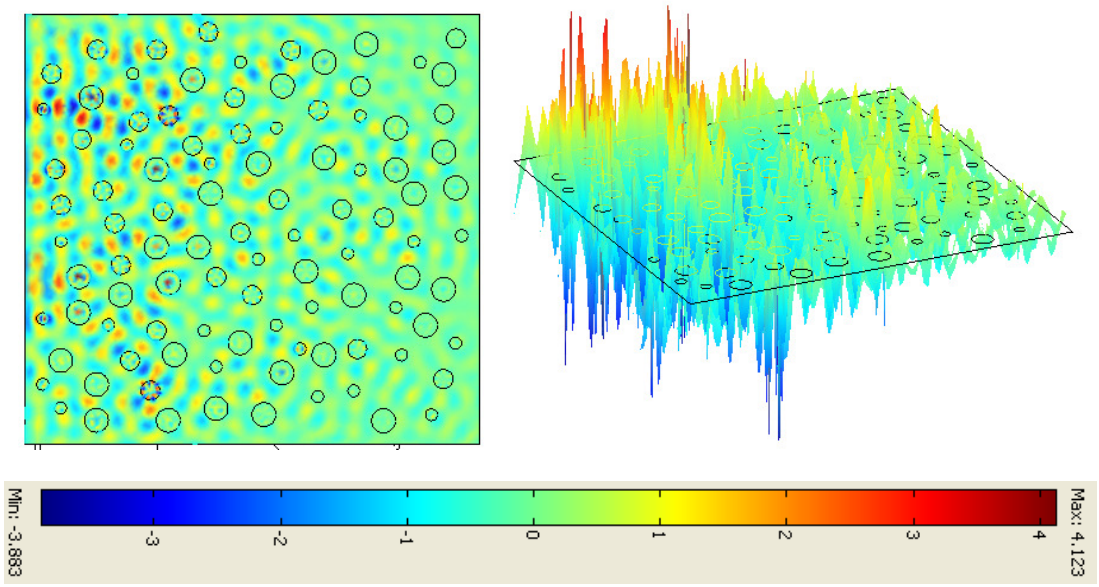

(b) $\lambda = 1\ \mu m$

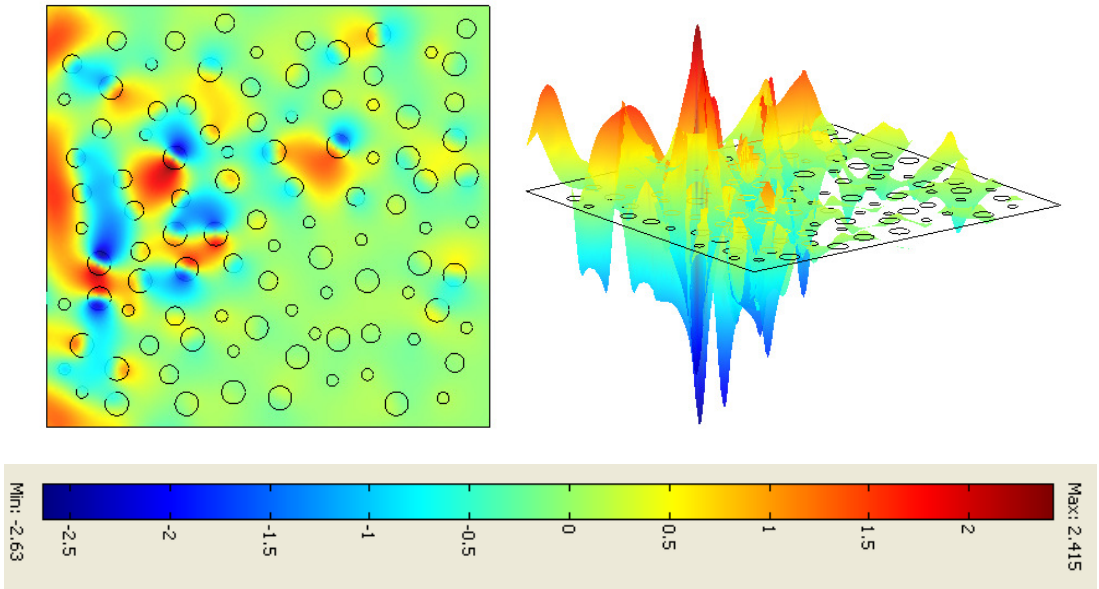

(c) $\lambda = 1.3\ \mu m$

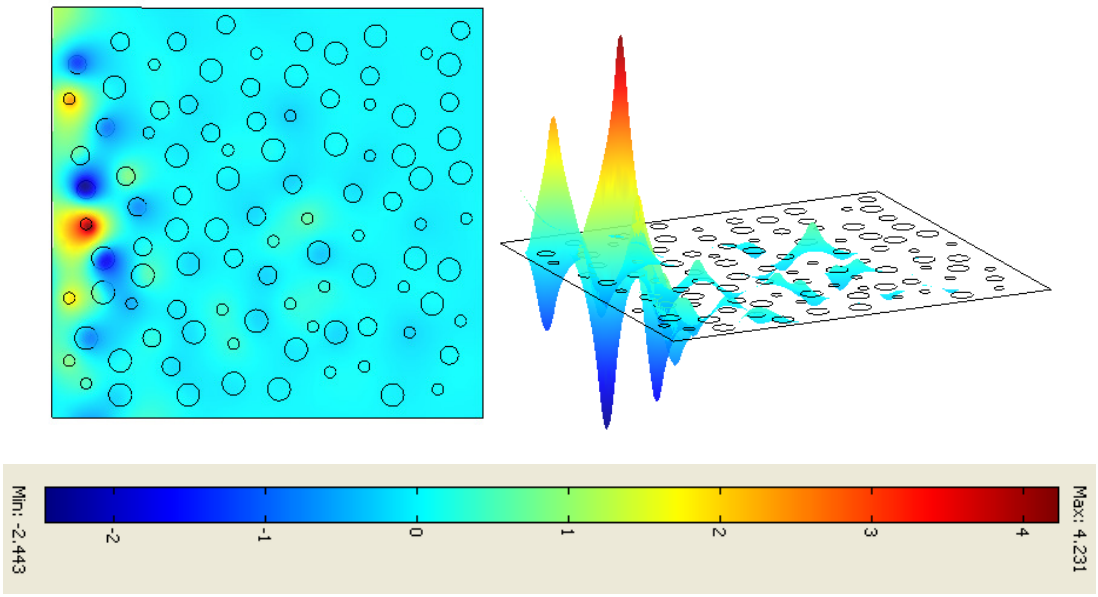

(d) $\lambda = 2.5\ \mu m$

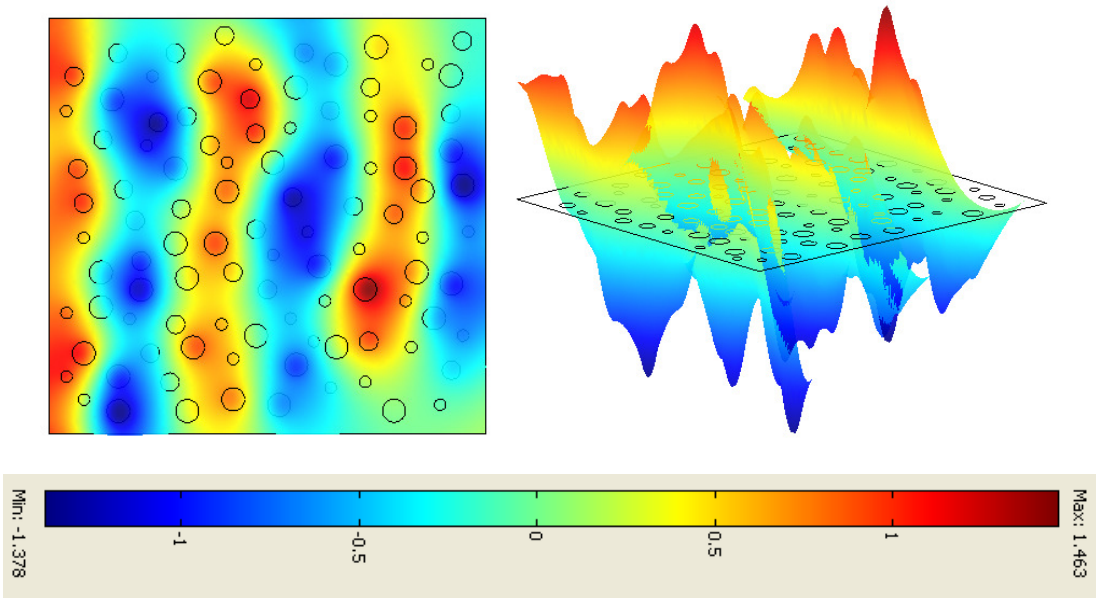

Figure 5.26: Simulation of the wave propagation across the silicon pillars lattice for incident wavelength at (a) 0.2 μm, (b) 1 μm, (c) 1.3 μm, and (d) 2.5μm. For each figure, the wave propagate from left to right as showed in the plan view (top left), 3-D view (top left) while the colour chart indicates the intensity of the electric field.

The wave propagation profile in the second disordered structure was similar to the first disordered structure. Figure 5.26 (a) shows a transmission profile for wavelength at 0.2 μm. As previously shown, short wavelengths demonstrate very strong diffusion as the waves propagate through the disordered pillars. Interference processes leads to many fluctuation in intensity distribution. Therefore, sharp peaks intensity could be observed and the wave was able to propagate through the pillars and gave a reading at the measured point. Localisation of light occurred due to enhanced backscattering phenomenon within the structure.

At a longer wavelength of 1 μm in figure 5.26 (b), the wave propagates with less diffusion process. As the scattering was still high, strong intensity peaks of localised light were observable on several parts of the geometry. The wavelength at 2.5 μm in figure 5.26 (c) represents the wave propagation profile belong to the band gap. Although there was no signal detected at the measured point, however a strong localised peak was found on the left edge of the geometry. Other than that, some weak signals were also detected on some parts of the geometry. Figure 5.26 (d) shows the profile for a wavelength of 2.5 μm. Within geometry dimension this wavelength was considered as long enough to propagate accross without much problem. The light diffuses on the bigger scale where it scattered and interfered randomly and finally reached the right side of the structure at high signal amplitude.

The implication of this modelling may be profound. It shows clearly that an analogue of the electron case can be found as predicted. However, the evidence for localisation enable the design of devices such as sensors, detectors and laser devices described in the next chapter.

The laser processing of thin film silicon has shown that both the external and internal structure is changed significantly and this is controlled by the laser beam shape and energy. This allows tuning from insulating behaviour (oxynitride) to semiconducting (with crystal inclusions). The materials then go through a dramatic change in refractive index affecting the way e.m. radiation interacts with the structures. Coating in metal brings the structures to the metallic domain, offering even more applications, such as THz filters.

5.7 Chapter Summary

In this chapter, present of Si-H_x bonds has been shown by using FTIR measurements. Strong absorbance peaks has been observed at wavenumbers of 640 cm^{-1}, between 1980 and 2100cm^{-1}, and at 2095 cm^{-1}. After laser process, these peaks show reduction with the increase in laser fluence. Concentration of bonded hydrogen has been shown to decrease from 12 % in original sample, to 4.2 % and 1.5 % for HE and LE samples respectively, after irradiated at 312.5 mJ/cm^2. Optical transmission and absorbance measurement reveals 98 % of the incident light absorbed by the laser process sample irradiated by laser fluence from 218.8 to 312.5 mJ/cm^2. Changing incident angle by moving away from normal also has been shown to increase the optical absorbance with 98 % is absorbed at 60^0. Finally, simulation on light transmission across disordered material had revealed a strong scattering occurred that could possibly leads to localisation of light phenomenon in physical world.

Chapter 6 Summary and Conclusion

6.1 Introduction

In this chapter an overall discussion will be given based on the results and analysis of chapter 3, 4 and 5. It will follow the order of discussion from the thermal aspects which were about the formation process of microstructures and the effect of parameter variation. On the electrical and optical aspect, findings from conductivity measurement, field emission, FTIR, UV-Vis, TR measurement and photonic crystals simulation will be summarised. A discussion on possible applications is presented in the last section. Finally, conclusion of this thesis will be given followed by future work suggestions.

6.2 Thermal Aspect

6.2.1 Formation of Microstructures

It has been demonstrated that the main outcome from KrF laser irradiation on amorphous silicon film was the formation of homogeneous and a high density of randomly distributed conical microstructures. The microstructures resulted from the repetition process of rapid melting and resolidification of amorphous silicon film in SLG regime. The tallest feature achieved was 5 μm compared to the original film at thickness of 0.3 μm. This means that the microstructure gained more than 16 times of the original film thickness through volume expansion.

Although the process and features was similar in some ways to results presented by Mazur's group [5-6], the background interaction was very different. The formed microstructures resulted from reactive chemical etching by irradiation of femtosecond laser pulses due to the present of SF_6 in the surounding environment [5] whereas the former rapid melting and resolidification proces takes place using pulses of UV laser in normal air condition. Other parameters involved includes intensity of the applied laser fluence, shape of beam pulse hence direction of scanning scheme and effective number of pulses. Varying these parameters lead to a new material with various kinds of structures with possibities of different potential appications.

6.2.2 Effect to Microstructure by Varying Parameters

KrF excimer laser irradiation was the source of energy used to transform the amorphous silicon surface. The excimer laser has fixed wavelength output and pulse duration at 248 nm and 20 ns respectively. The optical path was adjusted so that the beam has an asymmetrical shape as discussed in section 3.2.2. The distance between the laser aperture and sample stage was also fixed and the affected irradiation area was approximately 0.32 mm^2. The variable parameters were the percentage of output energy, scanning direction and frequency of irradiation.

The variation in output energy leads to different laser fluence irradiation onto the amorphous film surface, hence the capacity of absorbed energy. In section 3.3.2, it has been shown that the microstructures started to form when the laser fluence at

175 mJ/cm^2 was high enough to melt the amorphous silicon. An increase of the applied laser fluence leads to bigger and taller size of the microstructures. However, the density per unit area of the microstructures was reduced. Higher laser fluence at 359.4 mJ/cm^2 and beyond leads to the process of ablation where the material left the substrate and exposed underlying substrate.

The laser asymmetrical beam profile has a role in determining the final shape of the microstructures. The two possibilities were whether the sample experienced high energy first (termed as HE scheme) or low energy first (termed as LE scheme). The former scheme yields sharp microstructure feature while the latter scheme yields to blunt and rounded microstructure features. Different microstructure feature resulted from different irradiation processes where the sample experience a sudden increase to lower energy in the HE scheme and slower increase to higher energy in the LE scheme.

The number of laser irradiation pulses on the film surface depends on irradiation frequency and scanning speed. At frequency of 50 Hz and 0.5 mm/s scanning speed, the total numbers of pulses delivered on specific location were 400. In section 3.3.7, it has been shown that the surface deformation took place right after the first irradiation process. However, the microstructures existed only after the sample was scanned and subjected to hundreds of laser pulses. A combination in the repetition process of rapid melting, capillary waves action and resolidification finally leads to the formation of microstructure as depicted in figure 3.24.

The existence of a metal layer between amorphous silicon film and glass substrate also leads to different result in heat absorption profile. Metal was very well

known as a good heat conductor acting as a heat ballast layer. During laser irradiation, heat from the film layer was quickly absorbed by the metal layer and temperature was maintained at a certain level before dissipated to the substrate layer. Therefore, high temperature from the film surface was prohibited from reaching the substrate. This feature suggests that an appropriate thickness of film sample could be deposited on variety of substrates with low melting point such as polymer for application in flexible electronics as an example.

Another factor contributing to the formation of microstructures was the present environment. It has been shown in section 3.3.5 that the microstructures were not formed if irradiation was carried out in vacuum. Therefore it was believed that oxygen and nitrogen, the main constitute of a normal atmosphere, played the crucial role. Additionally, EDX spectroscopy reveals evidence about the existence of oxygen incorporated within the structure.

6.3 Electrical Aspect

6.3.1 Conductivity Results

A study on the dark conductivity profile was carried out to examine the thermally activated carriers from laser irradiated samples with the HE and LE schemes and to give more insight into the composition and structure of the material. Given the black nature of the material and its apparent high absorption, photoconductivity measurements were carried out as a comparison to measure any photo generated carrier. Arrhenius plots of these samples shows a shifting in the

slope which was directly related to the value of activation energy of the samples. The slopes for HE and LE samples looks similar as did the conductivity profiles of both samples as well. For both samples, the results show that the activation energy decreases as the applied laser fluence increases.

Ratios for conductivity at 450 K to room temperature conductivity (σ_T/σ_{RT}) vary from high as 150 in untreated amorphous silicon to 9.16 and 2.63 for HE and LE samples respectively. A similar case was observed in comparison between the ratios of photocurrent to dark current (I_p/I_d). The ratios vary extremely from 59600 in untreated amorphous silicon to 1.77 and 1.40 for HE and LE samples respectively. The decrease in the ratios was attributed to the increase in the crystallisation effect which leads to formation of microcrystalline silicon with high concentration of grain boundaries and defects. Furthermore, extra defects were created resulting from the hydrogen liberation process which left empty states as effective traps in the matrix. The difference in HE and LE profiles must also reflect the nature of the liberation of the hydrogen and the subsequent internal structure of the material.

Analysis of the relation between the pre-exponential factor, $\sigma_{o,}$ as a function of activation energy E_a demonstrates that these samples obeyed the Meyer-Neldel rule which is normally seen in porous, amorphous and microcrystalline silicon. This suggests that the samples were not fully crystallised into crystalline silicon by the laser irradiation.

6.3.2 Field Emission Results

Analysis of field emission results were carried out for samples irradiated in air using the HE scheme and LE scheme and samples irradiated in a vacuum environment. It has been shown that a comparatively good field emission had been produce by laser irradiated samples in normal air condition. For HE scheme samples, the lowest emission was demonstrated at E_{th} as low as 3 V/μm, from a sample irradiated with a laser fluence of 256.6 mJ/cm^2. For LE scheme samples, lower E_{th} values than the former samples were demonstrated. The lowest emission threshold at a laser fluence of 175.0 mJ/cm^2 was achieved at E_{th} of 2 V/μm. For samples irradiated in vacuum, the lowest E_{th} was achieved with value of 6.8 V/μm at laser fluence of 218.8 mJ/cm^2 sample.

If surface morphology were taken into account, the HE samples with sharp spike feature were physically closer to Spindt tip emitters. However, it had been revealed that a blunt feature produced electron emission at a lower field. Additionally, samples with small protrusions (low energy irradiation) also demonstrate a good electron emission. Even samples with a flat morphology exhibited field emission at low thresholds, suggesting the internal structure plays a significant role. Similar behaviour was found from samples irradiated in vacuum, where electron emission was produced although at much higher external field. This type of sample was shown to have very small protrusion and pores in the size of 0.1 to 0.2 micron. F-N plot of the samples shown mixes relation between log (I/E^2) and 1/E. For HE scheme samples, the F-N plot demonstrates a linear relation only at a certain range of 1/E values. A different case was observed in the F-N plots for LE

scheme samples where the plots seemed to demonstrate a better linear relation. Additionally, the F-N plot for samples processed in vacuum showed an almost linear relation.

Differences and non-linearity in measured and calculated enhancement factors had been calculated and discussed previously [77,65,108]. It was believed that the emission process was not entirely dependent solely on the geometric field enhancement factor. It was also suggested that internal field enhancement factor responsible for the emission [108]. Electron emission at low threshold which was defined in range of 1 to 10 V/μm had been previously showed to occur from atomically flat surface [109]. And this emission was not exclusively due to geometrical enhancement factor. A good explanation has been proposed by Forbes [83] about existence of electrically conducting nanoparticles inside the laser processed film. The conducting nanoparticles could create field enhancement at the interface of surface/vacuum and lead to a creation of local field. With greater magnitude, this field would allow electrons from the metal layer to tunnel and move across the film and finally escape into vacuum. These nanoparticles which were formed by the laser irradiation process were distributed in random positions within the film. With the application of the external field, a stable filamentary conducting channel was formed between them where the electrons were allowed to tunnel from one nanoparticle to adjacent neighbour and finally escape into the vacuum. The multiple tunnelling processes are depicted in figure 6.1. Tunnelling current was determined by distribution and spacing of the nanoparticles where it will be increased with the decrease of the spacing. Therefore, as suggested previously [83],

overall field enhancement factor was a combination between geometric field enhancement and internal field enhancement. These results were an outcome from laser processing amorphous silicon which produced morphological changes and internal modification.

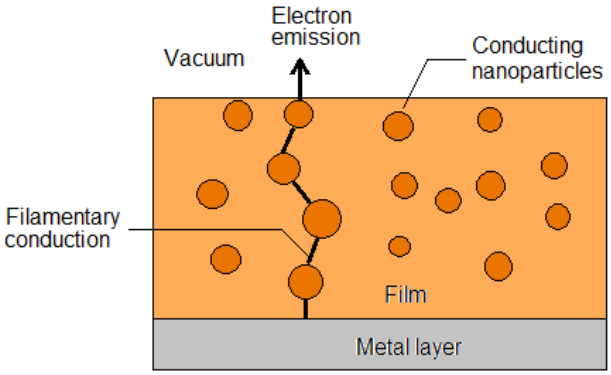

Figure 6.1: Filamentary conduction within film shows process of electronic transport from metal layer to vacuum.

6.4 Optical Aspects

6.4.1 IR Absorbance and Hydrogen Content

FTIR measurement and analysis in section 5.3 gives IR absorbance profile of the samples. The analysis reveals variation of Si-H_x absorbance peaks for original and laser processed amorphous silicon samples. Absorbance spectra from the original sample reveal a strong peak at 640 cm^{-1} which belong to Si-H bend mode and Si-H_2 wag mode. Another peak was shown between 1980 and 2100 cm^{-1} which belong to Si-H two stretch modes and Si-H_2 stretch mode at 2095 cm^{-1}. The plots of the IR absorbance spectra for HE and LE samples were almost identical, except at the highest laser fluence for HE sample at wavenumber of 640 cm-1 where it showed a higher peak than LE samples. All laser processed samples showed a reduction in the Si-H_x absorbance peaks with the increase in applied laser fluence. The reduction was due to the process of hydrogen liberation by multiple laser irradiations.

The laser processed samples also demonstrate an increase in water absorbance peaks compared to the original sample due to present of roughened and structured surface. Analysis in concentration of bonded hydrogen shows a decrease in percentage. For HE scheme samples, the percentage was decreased from 12 % in original sample to 4.2 % for sample with the highest laser fluence at 312.5 mJ/cm^2, whilst the LE sample demonstrate a bigger reduction to only 1.5 % at the same laser fluence. Therefore, it was believed that application of heat from lower to higher as in LE scheme leads to lower hydrogen content as showed in the result. Overall, it was more proof that hydrogen was still present within the samples albeit experienced with multiple processes of rapid melting and resolidification at high temperature. It

is likely that this hydrogen is associated with the local microstructure after irradiation.

6.4.2 Transmission and Absorbance

Analysis and discussion on optical transmission and absorbance were carried out in section 5.4 and 5.5. UV-Vis measurements cover the spectrum within the range from 200 to 1100 nm. It has been shown that wavelengths below 500 nm were completely absorbed by original amorphous silicon film. With laser processing, the results show increases in light absorbance with increases in applied laser fluence. LE scheme samples microstructure demonstrates better absorbance than HE scheme samples where only the sample at lowest laser fluence showed a small transmission beyond wavelength of 600 nm. While, the HE scheme samples demonstrates small transmission with the first two lowest laser fluence. It showed here that blunt microstructures in LE scheme samples absorb light better than sharp spikes.

Analysis in section 5.5 demonstrates a transmission profile at various incident angles. This showed that the original sample was not affected significantly. LE scheme samples show a slight change at all incident angle except at 60^{o}. A dramatic change was seen in HE scheme samples where transmission reduced abruptly with increase in incident angle. The profile of absorbance at various incident angles with increase in applied laser fluence were observed by using a single wavelength source. The absorbance profile for HE and LE scheme were very

similar, although the LE scheme demonstrates better absorbance at lower laser fluence.

6.4.3 Localisation of Light

Analysis in localisation of light was given in section 5.6. The microstructures produced from laser irradiation had a resemblance of photonic crystals pillars with a random size and distribution. Overall, three models were used to simulate light propagation in one ordered and two disordered photonic crystals pillars. The first disordered structure was at a similar scale with the ordered structure, while the second disordered was at a much lower dimensional scale. A plot of intensity of the wave propagation in photonics crystals demonstrate transmission mode with the existence of a band gap.

In the ordered photonic crystal, wavelengths below 1.5 μm propagates with strong scattering. A band gap was identified in the range of 3.4 to 5.4 μm where no light propagation took place. Beyond the bandgap, propagation took place without any scattering. In the first disordered structure, a plot of wave propagation shows a similar profile with the existence of propagation modes and a band gap. However, some discrepancies were observed. The size of the band gap (between 3.1 to 4.4 μm) was smaller and below the band gap propagation of light occurs with strong diffusion. Strong scattering leads to transmission but at a lower intensity than in the ordered structure. Although the band gap exists, the light managed to diffuse within 2 μm into the structure. Localisation of light has been observed due to enhanced

backscattering phenomenon. For the second disordered structure similar transmission profiles including localisation of light were observed, although at a much lower scale. Additionally, there were two band gaps regions observed at 0.7 to 0.85 μm and at 1.1 to 1.6 μm. Wavelength belong to the band gap was showed to diffused into a much greater length into the structure.

6.5 Applications

The results suggest that we have a new material that shows external morphological change that can be exploited in a number of ways, and that its internal structure must also have changed with nanoscale crystal like inclusion making it a nanocomposite material. A combination of both of these features class the material as a metamaterial. The absorption of light has been shown to in excess of 98% making the material a candidate for moth-eye absorber for solar cells. Conventional silicon will show a reflectance of 30%. Coupling this black absorber means more light is gathered. The black absorption also means the material can be exploited as a black absorber in solar thermal devices. The external structure has been modified and can produce degrees of hydrophobicity which can be exploited in self-cleaning applications and in biological research to examine the effect of substrate topology on cell growth.

The interactions with e.m. radiation can be exploited in a number of ways. The external structure and internal nanoparticle structure may offer a route to stealth

wind turbine blades for radar absorption and the materials can also be exploited as terahertz filter.

The internal structure has been modified and it seems that through the volume expansion effect that oxygen and nitrogen are incorporated providing a matrix for the conducting inclusions. The mechanism of transport has been described above as field induced filamentary conduction which can be exploited in field emission applications as a large area ballistic electron surface-emitting display (BSD). The three dimensional morphology lends itself to self-aligned gate technology. However, as the technology was relatively new, further research and development are required to mature and exploit this new material for various possibilities of potential applications.

6.6 Thesis Conclusion

A lot has been achieved during this project which covers a detailed study, simulations and characterisation of microstructures produced by KrF excimer laser irradiation in terms of thermal, electrical and optical properties.

From the thermal analysis, it was revealed that microstructures resulted from the repetition process of rapid melting and resolidification by asymmetrical pulses laser irradiation in air. Different microstructure morphology could be produced by varying scanning direction whether HE scanning scheme (sharp spike) or LE scanning scheme (blunt). The microstructure could be tuned in terms of its external and internal structure, enabling a new large area material that has technological applications in a number of areas.

Good and stable electron field emission has been achieved with a process free of photolithography, one that is easy to realise and relatively cheap over a large area. This provides as the basis for a potential candidate for cold cathode electron field emitters. Analysis from conductivity measurements and FTIR reveals the presence of hydrogen bonding although a laser fluence as high as 312 mJ/cm^2 has been applied. This indicates the material was not fully crystallised silicon. UV-Vis measurements reveal a good optical absorbance has been achieved across UV and optical spectra regions which suggest for application in solar power devices. It is in effect a large area black silicon material.

Approaches of this material as a metamaterial reveals the phenomenon of light localisation existed using computer modelling simulations. It was found that

this localisation was at the barrier of diffusive transmission and Anderson localisation. It was an interesting finding in optical properties of disordered photonic crystals closely related to electron localisation observed in disordered network of amorphous silicon which described earlier.

In summary, a new fundamental technique to produce this new material and basic characteristics has been shown and further work is expected to reveal more interesting results and other potential applications.

6.7 Future Work

This thesis has set a foundation for further work. The aim of the work was to examine the structural, thermal, optical and electrical properties of a novel large area laser processed material. This has shown the material to be useful in a number of ways with a number of potential applications. The changes in external shape of the structures allow tuning of the surface energy that enable hydrophobic differentiation. The surface morphology changes that can be effected and tuned also allow it to be used as a substrate to explore the interaction with living cells. This work has already started and it shows that BV-2 microglia can sense surface topology, where they undergo a phenotypic change in response to a mechanical environmental cue associated with silicon nano-structures. The BV-2 cells adopt a more elongated morphology in the presence of micro-nano spikes and exhibit increased levels of actin-rich microdomains, suggesting enhanced adhesion [110].

The internal structure of the features should be examined by high resolution microscopy. TEM studies proved difficult during the time of this work. It has been shown from field emission studies that there is an internal structure which allows high level of conduction under applied fields. This has been postulated as crystallised features in a more insulating material. The material should be planarised and etched back to expose sections of the spikes, and then examined by scanning current imaging. This would give insights that would enable the material to be tuned to more effective field emission for display applications.

The absorbing nature of the material to e.m. radiation can be readily exploited in solar energy. The antireflection nature of the coating (moth eye) and apparent absorption in excess of 98% translates to devices that will deliver photovoltaics at a lower cost per peak watt. Considering the material as a new nanocomposite, investigation in solar thermal application should be carried out where a combination process of thermionic and field emission could operate as an effective solar thermal device.

The material has been shown to operate as a disordered photonic crystal and this has many implications. The boundary between diffusive transmission and localisation of light can be examined and exploited in a number of ways. A deeper understanding of the refractive index of the material and how it can be modified would allow the material to be exploited as a metamaterial for application such as random lasers and THz filters.

References

[1] *http://hyperphysics.phy-astr.gsu.edu/hbase/tables/elabund.html*

[2] J. R. Woodyard, *United States Patent*, No. 2,530,110 (1950)

[3] W.E. Spear, P.G. LeComber, *Solid State Communications*, **88**, 1015 (1975)

[4] P. G. LeComber, W. E. Spear, A. Ghaith, *Electronics Letters*, **15**, 179 (1979)

[5] T. Her, R. J. Finlay, C. Wu, S. Deliwala, E. Mazur, *Applied Physics Letters*, **73**, 1673 (1998)

[6] C. Wu, C. H. Crouch, L. Zhao, J. E, Carey, R. Younkin, J. A. Levinson, E. Mazur, R. M. Farrell, P. Gothoskar, A. Karger, *Applied Physics Letters*, **78**, 1850 (2001)

[7] *http://www.heise.de/newsticker/meldung/Schwarzes-Silizium-Sensor-Material-der-Zukunft-205681.html*

[8] Y. Fan, M. J. Rose, S. K. Persheyev, M. Z. Shaikh, *Symposium on Photonics and Optoelectronics* (2009)

[9] *http://mysite.du.edu/~jcalvert/phys/silicon.htm*

[10] M. G. Voronkov, *Russian Journal of Applied Chemistry*, **80**, 2190 (2007)

[11] H.F. Sterling and R.C.G. Swann, *Solid-State Electronics*, **8**, 653, (1965)

[12] R. C. Chittick, J. H. Alexander, H. F. Sterling, *Journal of the Electrochemical Society*, **116**, 77 (1969)

[13] P.G. LeComber, W.E. Spear, *Physical Review Letters*, **25**, 509 (1970)

[14] A. Madan, *Invited talk, ICANS21* (2005)

[15] A. J. Lewis, Jr., G. A. N. Connell, W. Paul, J. R. Pawlik and R. J. Temkin, *International Conference on Tetrahedrally Bonded Amorphous Semiconductors, AIP Conf. Proc*. 20, 27 (1974).

[16] R. A. Street, *Technology and Applications of Amorphous Silicon*, Springer-Verlag (2000)

[17] P. K. Weimer, *Proceedings of the IRE*, **50**, 1462 (1962)

[18] W. H. Zachariasen, *Journal of the American Chemical Society*, **54**, 3841 (1932)

[19] H. Overhof, P. Thomas, *Electronic Transport in Hydrogenated Amorphous Semiconductors*, Springer-Verlag (1989)

[20] F. Urbach, *Physical Review*, **92**, 1324 (1953)

[21] C. M. Fortmann, *Physical Review Letters*, **81**, 3683 (1998)

[22] R. A. Street, *Hydrogenated Amorphous Silicon*, Cambridge University Press (1991)

[23] P. W. Anderson, *Physical Review*, **109**, 1492 (1958)

[24] N. F. Mott, E. A. Davis, *Electronic processes in non-crystalline materials*, Clarendon Press (1979)

[25] T. Tiedje, A. Rose, *Solid State Communication*, **37**, 49 (1980)

[26] N. F. Mott, *Reviews of Modern Physics*, **40**, 677 (1968)

[27] P. G. LeComber, D. I. Jones, W. E. Spear, *Philosophical Magazine*, **35**, 1173 (1977)

[28] R. C. Chittick, J. H. Alexander, H. F. Sterling, *Journal of the Electrochemical Society*, **116**, 77 (1969)

[29] P. Roca i Cabarrocas. *Journal of Non-Crystalline Solids*, **31**, 266 (2000)

[30] J. Robertson, *Journal of Applied Physics*, **87**, 2608 (2000)

[31] P. J. Kelly, R. D. Arnell, *Vacuum*, **56**, 156 (2000)

[32] S. G. Brush, *Historical Studies in the Physical and Biological Sciences*, **37**, 205 (2007)

[33] J. P. Gordon, H. J. Zeiger, C. H. Townes, *Physical Review*, **95**, 282 (1954)

[34] T. H. Maiman, *Nature*, **187**, 493 (1960)

[35] A. Javan, W. R. Bennett, Jr., D. R. Herriott, *Physical Review Letter*, **6**, 106 (1961)

[36] S.I. Anisimov, *Soviet Physics - JETP* **27**(1), 182 (1968)

[37] U. Paek, F.P. Gagliano, *IEEE Journal of Quantum Electronics*, **8**, 112 (1972)

[38] R. E. Wagner, *Journal of Applied Physics*, **45**, 4631 (1974)

[39] H. F. Cline, T. R. Anthony, *Journal of Applied Physics*, **48**, 5096 (1977)

[40] Y. Hayafuji, Y. Aoki, S. Usui, *Applied Physics Letters*, **42**, 720 (1983)

[41] T. Sameshima, S. Usui, H. Tomita, *Japanese Journal of Applied Physics*, **26**, L1678 (1987)

[42] T. Sameshima, M. Hara, S. Usui, *Japanese Journal of Applied Physics*, **28**, L2131 (1989)

[43] T. Sameshima, M. Hara, S. Usui, *Japanese Journal of Applied Physics*, **28**, L1789 (1989)

[44] T. Sameshima, S. Usui, *Journal of Applied Physics*, **70**, 1281 (1991)

[45] N.G. Basov, E.M. Balashov, O.V. Bogdankevitch, V.A. Danilychev, G.N. Kashnikov, N.P. Lantzov, D.D. Khodkevitch, *Journal of Luminescence*, **1-2**, 834 (1970)

[46] D. Basting, K. Pippert, U. Stamm, *2nd International Symposium on Laser Precision Microfabrication*, 14 (2002)

[47] A. Masters, T. Geuking *Beam-shaping optics expand excimer-laser applications*, Laser Focus World, Pennwell Corporation, June (2005)

[48] *Excimer Laser Product Guide*, Coherent (2011)

[49] *http://www.rp-photonics.com/excimer_lasers.html*

[50] D. Basting, G. Marowsky, *Excimer Laser Technology*, Springer (2005)

[51] James, S. Im and H.J. Kim, *Applied Physics Letters*, **63**, 14 (1993)

[52] James S. Im, H.J. Kim, *Applied Physics Letters*, **64**, 17 (1994)

[53] R. Z. Bacharach, K. Winer, J. B. Boyce, S. E. Ready, R. I. Johnson, G. B. Anderson, *Journal of Electronic Material*, **19**, 241 (1990)

[54] N. H. Nickel, H. J. Kim, M.O. Thompson, *Physical Review B*, **56**, 12065 (1997)

[55] M. O. Thompson, G. J. Galvin, *Physical Review Letters*, **52**, 2360 (1984)

[56] J. Narayan, C. W. White, *Applied Physics Letters*, **44**, 1 (1984)

[57] D. H. Lowndes, G.E. Jellison, *Applied Physics Letters*, **48**, 20 (1986)

[58] D. J. McCulloch, S. D. Brotherton, *Applied Physics Letters*, **66**, 2060 (1995)

[59] D. Toet, P. M. Smith, T. W. Sigmon, T. Takehara, C. C. Tsai, W. R. Harshbarger, M. O. Thompson, *Journal of Applied Physics*, **85**, 7914 (1999)

[60] D. K. Fork, G.B. Anderson, J. B. Boyce, R. I. Johnson, P. Mei, *Applied Physics Letters*, **68**, 2138 (1996)

[61] Y. Fan, M. J. Rose, S. K. Persheyev, M. Z. Shaikh, C. Main, *Conference Paper* (2006)

[62] *http://www.coherent.com/Applications/index.cfm?fuseaction=forms.Page&PageID=172*

[63] *http://www.purdue.edu/rem/rs/sem.htm*

[64] C. Main, *Notes on Laser pulse heating of thin films* (2006)

[65] Y. F. Tang, *PhD Thesis*, University of Surrey (2002)

[66] H. Fritzsche. *Journal of Non-Crystalline Solids*, **6**, 49 (1971)

[67] C. C. Tsai, *The American Physical Society*, **19**, 2041 (1979)

[68] N. F. Mott: *Electronic and Structural Properties of Amorphous Semiconductors*, Eds. P. G. LeComber and J. Mort Academic Press, London, 1 (1973)

[69] G. Micard, K. Peter, D. Chrastina, G. Isella, *22nd European Photovoltaic Solar Energy Conference,* EU PVSEC, Italy (2007)

[70] W. Meyer, H. Neldel, *Z. Tech. Phys.,* **12**, 588 (1937)

[71] K. Tanaka, K. Shimakawa, *Amorphous Chalcogenide Semiconductor and Related Materials*, Springer (2011)

[72] J. Stuke, *Journal of Non-Crystalline Solids*, **97-98**, 1 (1987)

[73] T. Utsumi, *Journal of the Society for Information Display*, **1**, 313 (1993)

[74] D. R. Whaley, B. M. Gannon, C. R. Smith, C. M. Armstrong, and C. A. Spindt, *IEEE Transactions on Plasma Science*, **28**, 727 (2000)

[75] R.H. Fowler and L. Nordheim, *Proceedings of the Royal Society*, **A119**, 173 (1928)

[76] B.H. Bransden and C.J. Joachain, *Introduction to Quantum Mechanics*, Longman Scientific and Technical (1989)

[77] N.S. Xu, Jun Chen, S.Z. Deng, *Applied Physics Letters*, **76**, 2463 (2000)

[78] G. A. J. Amaratunga and S.R. P. Silva, *Applied Physics Letters*, **68**, 2529 (1996)

[79] S.R. P. Silva, R. D. Forrest, D. A. Munindradasa, and G. A. J. Amaratunga, *Diamond and Related Materials*, **7**, 645 (1998)

[80] S.R. P. Silva, R. D. Forrest, J. M. Shannon, and B. J. Sealy, *Journal of Vacuum Science & Technology*, **17**, 596 (1999)

[81] D. S. Mao, J. Zhao, W. Li, C. X. Ren, X. Wang, X. H. Liu, J. Y. Zhou, Z. Fan, Y. K. Zhu, Q. Li, and J. F. Xu *Journal of Vacuum Science & Technology B*, **17**, 311 (1999)

[82] J. C. She, S. E. Huq, J. Chen, S. Z. Deng, and N. S. Xu, *Journal of Vacuum Science & Technology B*, **17**, 592 (1999)

[83] R. G. Forbes, *Ultramicroscopy*, **89**,7, (2001)

[84] Y. Lubianiker and I. Balberg, *Journal of Non-Crystalline Solids*, **227-230**, 180 (1998)

[85] M. Kondo, Y. Chida, A. Matsuda, *Journal of Non-Crystalline Solids*, **198-200**, 178 (1996)

[86] S. K. Ram, S. Kumar, R. Vanderhaghen, P. Roca i Cabarrocas, *Journal of Non-Crystalline Solids*, **299-302**, 411 (2002)

[87] H. P. Porte, D. Turchinovich, and P. Uhd Jepsen, S. Persheyev, Y. Fan, and M. J. Rose, *35th International Conference on Infrared, Millimeter, and Terahertz Waves*, CFP101MM-ART, Code 82573 (2010)

[88] H. Murakami, M. Hirakawa, C. Tanaka, *Applied Physics Letter*, **76**(13), 1776 (2000)

[89] A. H. M. Smets, *PhD Thesis*, Eindhoven University of Technology (2002)

[90] M. Stutzmann, *Philosophical Magazine B*, **60**, 531 (1989)

[91] D. L. Staebler and C.R. Wronski, *Applied Physics Letters*, **31**, 292 (1977)

[92] P. V. Santos, N. M. Johnson, and R. A. Street, *Physical Review Letter*, **67**, 2686 (1991)

[93] H. M. Branz, Sally Asher, H. Gleskova and S. Wagner, *Physical Review B*, **59**, 5498 (1999)

[94] S. John, *Physical Review Letter*, **53**, 2169 (1984)

[95] P. W. Anderson, *Philosophical Magazine B*, **52**, 505 (1985)

[96] S. John, *Physics Today*, **44**, 32 (1991)

[97] S. John, *Nature*, **390**, 661 (1997)

[98] D. S. Wiersma, P. Bartolini, A. Lagendijk, R. Righini, *Nature*, **390**, 691 (1997)

[99] D. M. Goldie, S. K. Persheyev, *Journal of Materials Science*, **41**, 5287 (2006)

[100] *http://teaching.shu.ac.uk/hwb/chemistry/tutorials/molspec/uvvisab3.htm*

[101] M. Cardona, M. *Physica Status Solidi (b)*, **118**, issue 2, pp. 463 (1983)

[102] M. Cardona, *Journal of Molecular Structure*, **141**, 93 (1986)

[103] P. Lengsfeld, N. Nickel, W. Fuhs, *Applied Physics Letters*, **76(13)**, 1680 (2000)

[104] R. Bruggemann, W. Bronner, M. Mehring, *Solid State Communications*, **119**, 23 (2001)

[105] A. H. Sari, F. Osman, M. Ghoranneviss, H. Hora, R. Hopfl, M.R. Hantehzadeh, *Applied Surface Science*, **237**, 161 (2004)

[106] R. A. Furler, *ASHRAE Transactions*, **97** (2), 1129 (1991)

[107] H. Butt, Q. Dai, and T. D. Wilkinson, *Progress in Electromagnetics Research*, **113**, 179 (2011)

[108] M. Z. Shaikh, *PhD Thesis*, University of Dundee (2008)

[109] G. A. J. Amaratunga and S.R. P. Silva, *Applied Physics Letters*, **68**, 2529 (1996)

[110] S. Persheyev, Y. Fan, A. Irving and M. J. Rose, *Journal of Biomedical Materials Research Part A*, **99A**, 135 (2011)